⑫

IMPROVEMENT OF THE SCINTILLATION - IRREGULARITY MODEL IN WBMOD

James A. Secan
Edward J. Fremouw
Physical Dynamics, Inc.

P.O. Box 3027
Bellevue, Washington 98009

28 February 1983

Final Report for Period 1 January 1981—31 December 1982

CONTRACT No. DNA 001-81-C-0092

> APPROVED FOR PUBLIC RELEASE;
> DISTRIBUTION UNLIMITED.

Prepared for
   Director
   DEFENSE NUCLEAR AGENCY
   Washington, DC 20305

DTIC
ELECTE
AUG 16 1983
B

ADA131556

DTIC FILE COPY

83 08 16 108

REPORT DOCUMENTATION PAGE	READ INSTRUCTIONS BEFORE COMPLETING FORM

1. REPORT NUMBER	2. GOVT ACCESSION NO.	3. RECIPIENT'S CATALOG NUMBER
DNA-TR-81-241	AD-A131 536	

4. TITLE (and Subtitle)	5. TYPE OF REPORT & PERIOD COVERED
IMPROVEMENT OF THE SCINTILLATION-IRREGULARITY MODEL IN WBMOD	Final Report for Period 1 Jan 81—31 Dec 82
	6. PERFORMING ORG. REPORT NUMBER
	PD-NW-83-285R

7. AUTHOR(s)	8. CONTRACT OR GRANT NUMBER(s)
James A. Secan and Edward J. Fremouw	DNA 001-81-C-0092

9. PERFORMING ORGANIZATION NAME AND ADDRESS	10. PROGRAM ELEMENT, PROJECT, TASK AREA & WORK UNIT NUMBERS
Physical Dynamics, Inc. P.O. Box 3027 Bellevue, Washington 98009	S99QAXHC-00019 62715H

11. CONTROLLING OFFICE NAME AND ADDRESS	12. REPORT DATE
Director Defense Nuclear Agency Washington, DC 20305	28 February 1983
	13. NUMBER OF PAGES
	98

14. MONITORING AGENCY NAME & ADDRESS(If different from Controlling Office)	15. SECURITY CLASS. (of this report)
	UNCLASSIFIED
	15a. DECLASSIFICATION/DOWNGRADING SCHEDULE
	N/A since UNCLASSIFIED

16. DISTRIBUTION STATEMENT (of this Report)

Approved for public release; distribution unlimited.

17. DISTRIBUTION STATEMENT (of the abstract entered in Block 20, if different from Report)

18. SUPPLEMENTARY NOTES

This work was sponsored by the Defense Nuclear Agency under RDT&E RMSS Code B310081466 S99QAXHC00019 H2590D.

19. KEY WORDS (Continue on reverse side if necessary and identify by block number)

Radiowave Scintillation
Phase Scintillation
Auroral Scintillation
Ionospheric Irregularities
Ionospheric Plasma Drift Velocity
Plasma Striation
Scintillation Model
Computer Model

20. ABSTRACT (Continue on reverse side if necessary and identify by block number)

The descriptive model of scintillation-producing irregularities in the F layer contained in Program WBMOD has been improved, along with other aspects of the code. Improvements include use of magnetic local time for modeling high-latitude boundaries, correction of a subtle error in calculating the scan velocity of the radio line of sight, simplification of the orbit calculation, and implementation of an irregularity drift routine based on a recently published model of ionospheric convection at high latitudes.

DD FORM 1473

20. ABSTRACT (Continued)

In preparation for future improvements in WBMOD, analysis and interpretation of the Wideband Satellite data base from Poker Flat, Alaska was continued. The utility of the phase-gradient ratio (i.e., the ratio of rms phase difference for interferometer baselines perpendicular and parallel to known sheetlike irregularities) was investigated for determining irregularity axial ratios and was found to be of potential use. The ratio varies strongly, however, with the phase spectral index, p. Thus, quantitative use of the phase-gradient ratio depends upon prior evaluation of the geophysical and geometrical behavior of p.

A study was initiated of the behavior of p in the data base from Poker Flat. The results show a marked variation with the angles between the line of sight and the local L shell and magnetic meridian. This behavior is interpreted tentatively as evidence for scale-size dependence of the degree of cross-field anisotropy exhibited by the irregularities, tending from sheetlike structures at the largest scales to rodlike structures at the smallest. In the course of the phase spectral study, two persistent features were found. The first is a downward break in the high-frequency spectral tail at about 10 Hz ($\approx$ 300 meters scale size in the direction of scan, which is roughly north-south geomagnetic). This feature, which was noted in about a quarter of the spectra inspected, is similar to breaks reported in equatorial data. The second feature, which occurs about three-quarters of the time, is an upward break on the low-frequency end of the spectrum (below 0.5 Hz, which corresponds to about 6 km).

Accession For

NTIS GRA&I		
DTIC TAB		☐
Unannounced		☐
Justification		

By_____
Distribution/
Availability Codes

Dist	Avail and/or Special
A	

TABLE OF CONTENTS

LIST OF ILLUSTRATIONS

3

LIST OF TABLES

SECTION 1

INTRODUCTION

In carrying out its mission to evaluate a wide variety of nuclear effects on weapons systems, the Defense Nuclear Agency (DNA) conducts a vigorous research program on high-altitude plasmas and their impact on radio propagation. In recent years, this program has concentrated on medium-scale structures (Keskinen and Ossakow, 1902) and the potentially disruptive radio-wave scintillations that they produce (Wittwer, 1979). A major element of that program's focus was DNA's Wideband Satellite Experiment (Rino et al, 1977; Fremouw et al, 1978).

High-latitude results from Wideband were put into a form directly useable for engineering evaluation of auroral-zone scintillation effects by means of a plasma-irregularity model and propagation routines encoded in a computer program called WBMOD (Fremouw and Lansinger, 1981). The Wideband data base from Poker Flat, Alaska, was used for iterative development and testing of the model. The program, written in Fortran, was constructed for highly interactive application by a systems-oriented user.

This report summarizes recent improvements in WBMOD. It also describes research into irregularity characteristics revealed by the Poker Flat data base, which could lead to further improvement in the high-latitude model and to guidance for DNA's forthcoming HILAT satellite program (Fremouw, 1982).

The code improvements are summarized in Section 2, starting with a routine to order high-latitude irregularity characteristics in geomagnetic rather than geographic time. Correction of a subtle error in treating the line-of-sight scan velocity of an orbiting satellite in the phase-screen propagation theory employed is described in Section 2-2, followed by refinement of the orbit calculation. Section 2-4 summarizes implementation of WBMOD for operational use at USAF Global Weather Central, as fully documented elsewhere (Secan, 1982). A major improvement for application of WBMOD to use of geostationary satellite links at high-latitude stations is described in Section 2-5, namely, incorporation of a realistic model (Heelis et al, 1982) for convective drift of irregularities in the high-latitude F layer.

A three-character revision numbering system has been adopted to identify major changes to the WBMOD program. The first (numeric) character identifies revisions in the overall structure of the code that is not directly part of the ionospheric irregularity model. The second (alphabetic) character identifies changes in the algebraic form of the irregularity model beyond simple revisions in the numerical constants that calibrate the model. The final (numeric) character identifies changes in these numerical constants. Lesser changes will be noted only by changes in the revision date.

This three-character revision number appears in a comment near the beginning of Program WBMOD, in the interactive dialogue with the user, and in the main output file. The model

5

contained in the code (e.g. B3) will be identified in comment statements near the beginning of subroutine MDLPRM and function FCSL. The current version of WBMOD, Revision 6B3, is summarized in Section 3.

Research topics are discussed in Section 4, starting with exploration of efficient means for deducing the three-dimensional configuration of scintillation-producing irregularities from interferometer data. One such technique was found to require independent information on the one-dimensional spatial spectrum of the irregularities, and spectral behavior is discussed in Sections 4-2 and 4-3.

IMPROVEMENTS IN WBMOD

2-1 MAGNETIC TIME.

Most high-latitude ionospheric phenomena are better ordered diurnally in magnetic time than in geographic-meridian time. Accordingly, the expression coded in WBMOD to describe the magnetic invariant latitude, λ_b, of the high-latitude scintillation boundary is as follows:

$$\lambda_b = 71.8° - 1.5K_p - 5.5 \cos \frac{\pi(t_m - 2)}{12} \tag{1}$$

where K_p is the planetary magnetic activity index, and t_m is time in hours past magnetic midnight.

For iterative testing against data from Poker Flat, a fixed offset was used between magnetic and geographic meridian time (namely, magnetic midnight lagging geographic meridian midnight by 1.5 hours). For use of the code at other locations, it is necessary to establish the magnetic-midnight offset as a function of geographic coordinates. A simple routine for calculating this offset was developed and implemented in Rev 3A2 and later modified in Rev 6B3. Both methods employed will be presented here.

2-1.1 Revision 3A2.

The basis for the magnetic-time calculation is the set of definitions established by McNish (1936). Magnetic midnight is defined as the time at which a line from the sun through the earth's center intersects the night side of the earth on the station's geomagnetic meridian. Magnetic time is then taken to advance at a constant rate of 24 hours per revolution of the earth on its spin axis. For calculating the magnetic longitude, ℓ_m, of a station, the following dipole-based expression is used:

$$\tan \ell_m = -\tan(\ell - \ell_o) \sin X \sec (X + \lambda_o) \tag{2}$$

where $\quad X = \tan^{-1}[\cos(\ell - \ell_o) \operatorname{ctn} \lambda]$

$\quad\quad \ell, \lambda$ = geographic longitude and latitude of station

and $\quad \ell_o, \lambda_o$ = geographic longitude and latitude of geomagnetic poles.

The calculation of the magnetic-time offset begins with a call by Subroutine CCGLT to Subroutine CGLT for calculation of the geomagnetic longitude of an ionospheric penetration point, using Eq. (2). A second call to CGLT finds the geomagnetic longitude of the effective anti-sun at the time that it lies in the penetration point's geographic-meridian plane. The anti-sun geomagnetic longitude is then adjusted, by means of an iterative loop, to match that

of the penetration point. The corresponding adjustment in geographic longitude, expressed in hours at the rate of 15° per hour, constitutes the lead time of magnetic midnight relative to geographic meridian midnight.

To calculate the true geomagnetic longitude of the physical sun, one would enter Subroutine CGLT using the declination of the sun for the input geographic latitude. There would then be a further correction for the equation of time. To calculate the true geomagnetic longitude of the anti-sun, one would employ the negative of solar declination for the input latitude and then make the identical equation-of-time correction.

Using the solar declination and correcting for the equation of time both introduce seasonal variations in the geomagnetic longitude of the sun for a given geographic longitude. The variation introduced by the equation of time is the same for the sun and the anti-sun. It is easy to show, however, that the seasonal variation introduced by employing the true declination is opposite for the sun and anti-sun. It is curious but true, therefore, that the seasonal variation in magnetic time as commonly defined depends upon whether one chooses noon (the sun) or midnight (the anti-sun) as the time origin.

One may avoid the difference imposed by the above arbitrary choice by employing zero declination for either the sun or the anti-sun, which corresponds to equinoctial conditions, and we have done so. To do otherwise would be to introduce an ill-based seasonal variation into our scintillation model. Since we hope to identify and code a true seasonal/longitudinal variation in scintillation, introduction of such a variation *a priori* (and, in effect, inadvertently) would introduce confusion into our efforts. For this reason, we have coded zero as the declination of the anti-sun, and we have chosen also to ignore the seasonal correction due to the equation of time. We shall keep the behaviors described thereby in mind as we investigate seasonal/longitudinal variation.

Figure 1 illustrates the difference between magnetic and geographic-meridian times computed by means of the magnetic-time offset routine. Magnetic-time advance is presented as a function of geographic longitude for four geographic latitudes.

2-1.2 Revision 6B3.

The procedure to convert local mean solar time (t_s) to local magnetic (dipole) time (t_m) was modified in Rev 6B3 to allow direct rather than iterative calculation of t_m. First, the dipole longitude is calculated from

$$\tan \lambda_m = \frac{\cos\lambda\sin(\ell-\ell_0)}{\sin\lambda_0\cos\ \cos(\ell-\ell_0)-\cos\lambda_0\sin\ \lambda} \tag{3}$$

where all variables are as defined in Equation 2. The geographic longitude (ℓ_e) at which ℓ_m crosses the geographic equator is calculated from

$$\ell_e = \ell_0 + \tan^{-1}(\sin \lambda_0 \tan \ell_m). \tag{4}$$

8
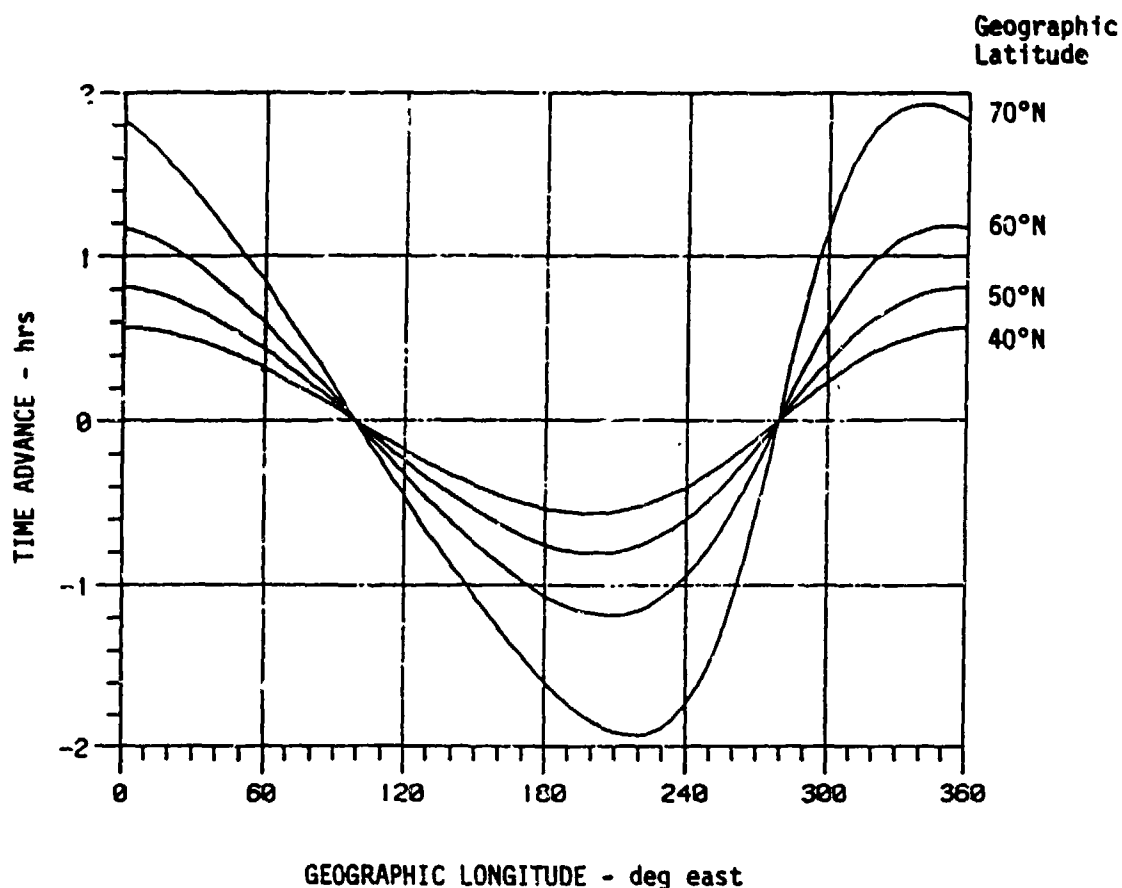
Figure 1. Difference between geomagnetic time and geographic-meridian time as function of geographic latitude and longitude. Negative values mean that geomagnetic midnight lags geographic meridian midnight.

The correction to LT then is defined as the difference between ℓ and ℓ_e, so

$$t_m = t_s + \frac{\ell - \ell_e}{15} .$$

(5)

This new algorithm, implemented in Function GMLTC, yields the same results as subroutines CCGLT and CGLT described in Section 2-1.1, but it is quicker, as no iteration is required.

An additional refinement to this calculation is use of the dipole pole location (λ_o, ℓ_o) calculated from IGRF-1980 using the expressions

$$\sin \lambda_o = \frac{g_{10}}{H_o}$$

9

$$H_o^2 = g_{10}^2 + g_{11}^2 + h_{11}^2$$

$$\tan \ell_o = \frac{h_{11}}{g_{11}}$$

where g_{nm} and h_{nm} are the (Schmidt quasi-normalized) spherical harmonic coefficients for the IGRF expansion. For epoch 1980.0 these values are λ_o = 78.8°N, ℓ_o = 70.76°W.

2-2 SCAN VELOCITY

During the course of iteratively testing WBMOD Rev 4A2 against Wideband scintillation data from Goose Bay, we encountered a problem in calculating scan velocity of the line of s⁻ht between a low-orbiting satellite and a fixed ground station. The problem seriously affected scintillation calculations for the observing geometry at Goose Bay, but had not been noticed for the Poker Flat geometry. The problem was traced not to a program bug but to a subtle error in the treatment of scan velocity in the scattering theory employed (Rino, 1979).

Prior to discovery of the problem, velocity was calculated in a subroutine called VXYZ using a coordinate system centered at the ionospheric penetration point (Rino and Fremouw, 1977). The geometry was developed from the point of view of spaced-receiver measurements on an observing plane. For application to single-receiver measurements of scintillations in the time domain, the approach was to calculate the velocity of the receiver as seen from the location of the ionospheric penetration point. The problem was that although the theory accounted for translation of the coordinate origin relative to the receiver, it did not take into account a rotation of the coordinate system relative to the local vertical.

For an observer located at the ground-based receiver, the moving coordinate system, coupled with the fact that irregularity anisotropy is handled in the scattering theory by means of an effective velocity, V_e, defined in a nonisotropic coordinate system, makes the velocity calculation somewhat obscure. The situation is quite clear, however, from the observer's point of view in a fixed reference frame centered at the receiver, especially for isotropic irregularities. The relevant velocity then obviously is that of the line of sight perpendicular to itself at the distance of the penetration point. Thus, for isotropic irregularities, V_e must reduce to

$$V_\perp = R\sqrt{\dot{\epsilon}^2 + \dot{\alpha}^2 \cos^2 \epsilon} \tag{6}$$

where R is the range from the receiver to the penetration point, ϵ is the elevation angle of the source as seen from the receiver, and α is the source azimuth from the receiver. We found that, for the Goose Bay observing geometry, it did not, as illustrated in Figure 2.

10
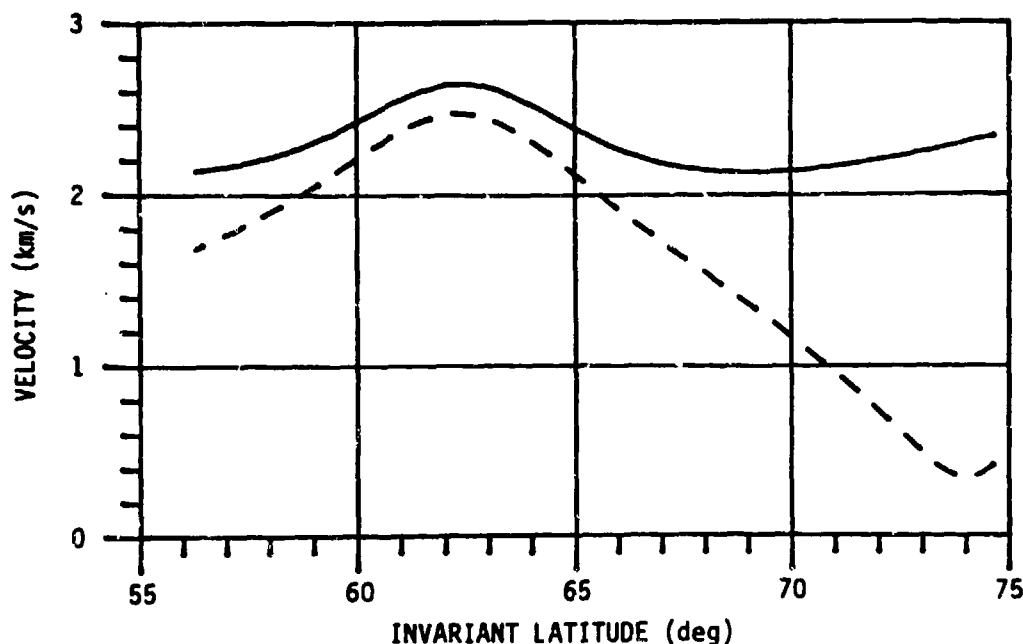
Figure 2. Comparison of V_e (dashed) calculated in WBMOD Rev 4A2 for isotropic irregularities, with $V_\perp$ (solid) calculated in receiver-centered coordinate system (Equation 1). The former should equal the latter, but does not. It is, therefore, incorrect.

The difficulty stems from rotation of the coordinate system; it may be appreciated from Figure 3, which illustrates the geometry at a calculation time, t_o, and at two time increments, $\pm\Delta t$. The scattering theory invokes a locally plane phase screen oriented horizontally at the t_o penetration point. The geometry is calculated, however, from a coordinate origin moving along a surface of constant height above a spherical earth.

The theory requires a two-dimensinal velocity referred to the instantaneous (planar) phase screen, which is given by

$$V_{sx} = V_x - V_z \tan \theta \cos \phi \tag{7a}$$

$$V_{sy} = V_y - V_z \tan \theta \sin \phi \tag{7b}$$

where θ and ϕ are the incidence angle and magnetic heading, respectively, of the propagation vector, and V_x, V_y, V_z are the three-dimensional velocity components of the receiver in the point-centered coordinate system. Equations (7) correctly shift the origin from the curved $z = 0$ surface to the intersection of the rays with the planar phase screen. They do not yield the correct two-dimensional velocity, however, unless the coordinate rotation is accounted for independently.

11
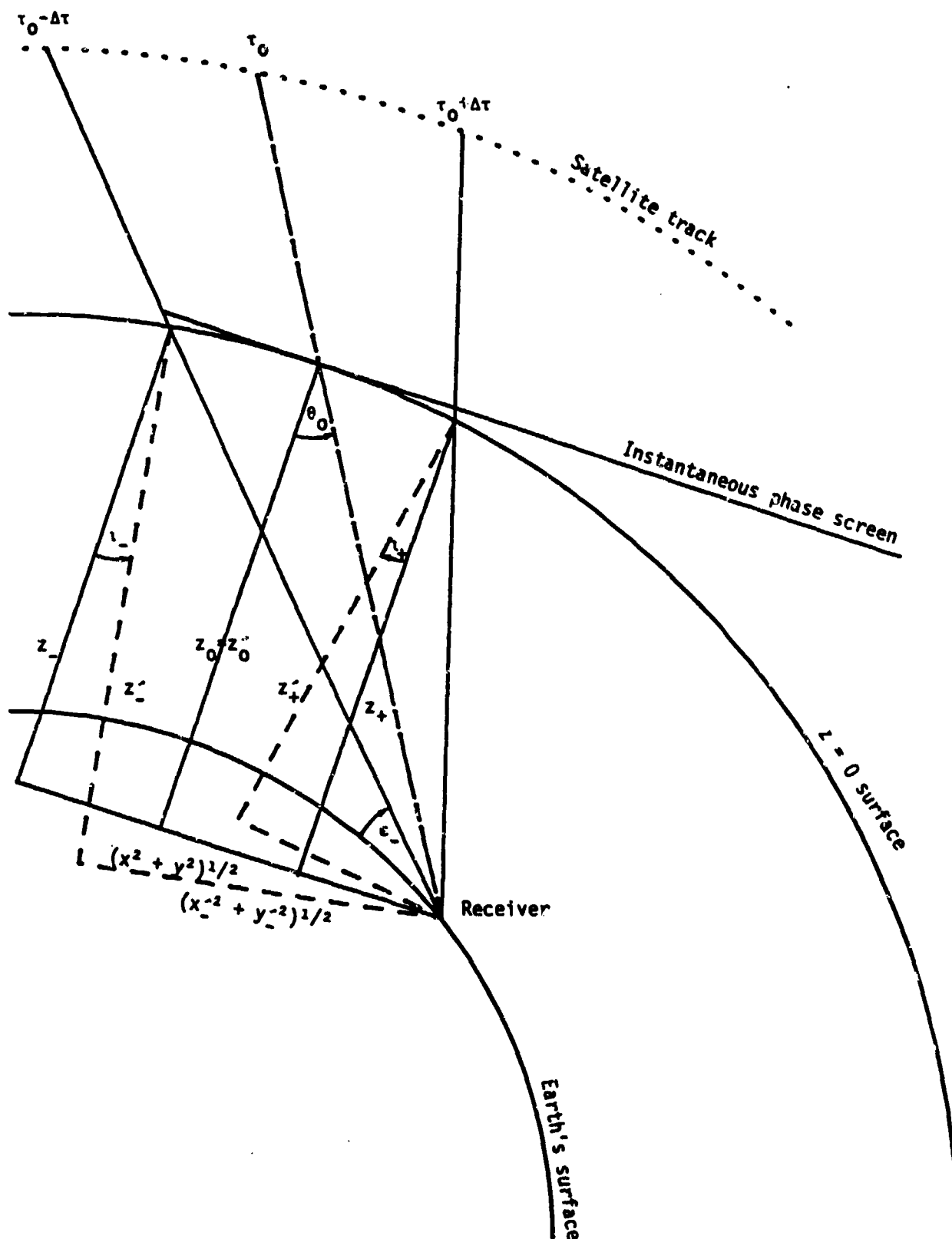
Figure 3. Illustrating the troublesome coordinate rotation.

12

The coordinate rotation is indicated in Figure 3 by the small angles, ι_- and ι_+. The velocity error arose from calculating the receiver position in a system oriented along the local vertical at the $\pm$ points, indicated by primed coordinate distances and the dashed triangles in Figure 3. The correct velocity is obtained by calculating the receiver position in a system oriented parallel to the instantaneous vertical at the calculation time, t_0, as indicated by the nonprimed coordinate distances and the solid triangles. Our finite-differences solution was to rotate through the angle, ι, from the primed to the non-primed coordinate system, by means of the following equations:

$$x_\pm = (x_\pm' \sin \lambda_\pm' + z_\pm' \cos \lambda_\pm) \cos(\ell_0 - \ell_\pm) - y_\pm' \sin(\ell_0 - \ell_\pm) \sin \lambda_0$$
$$+ (x_\pm' \cos \lambda_\pm - z_\pm' \sin \lambda_+) \cos \lambda_0 \qquad (8a)$$

$$y_\pm = (x_\pm' \sin \lambda_\pm + z_\pm' \cos \lambda_\pm) \sin(\ell_0 - \ell) + y_\pm' \cos(\ell_0 - \ell_\pm) \qquad (8b)$$

$$z_\pm = (x_\pm' \sin \lambda_\pm + z_\pm' \cos \lambda_\pm) \cos(\ell_0 - \ell_\pm) - y_\pm' \sin(\ell_0 - \ell_\pm) \cos \lambda_0$$
$$- (x_\pm' \cos \lambda_\pm - z_\pm' \sin \lambda_\pm) \sin \lambda_0 \qquad (8c)$$

where the primed and unprimed coordinates are as in Figure 3, and λ and ℓ respectively represent (geographic) latitude and longitude of the penetration points indicated by the subscripts.

In the case of spaced-receiver measurements, Equations (7) would account for the tilt angle of the observing plane (remote section of the earth's surface) in the point-centered coordinate system. In the situation at hand, it accounts only for the small angles between the $z = 0$ surface and the instantaneous planar phase screen, which in fact turns out to be negligible. The other effect of surface curvature (coordinate rotation) produced substantial velocity errors in certain circumstances, and it is now corrected for by means of Equations (8).

The in-screen velocity, V_s, is required because the scattering theory effectively collapses the thick irregularity layer as a shadow pattern onto the equivalent thin-phase screen. The relevant physical velocity, however, still is that perpendicular to the line of sight. The angular component of velocity is extracted and the range-rate component suppressed by means of the following expression for the effective velocity, V_e:

$$V_e = \frac{(C V_{sx}^2 - B V_{sx} V_{sy} + A V_{sy}^2)^{1/2}}{(AC - B^2/4)^{1/2}} . \qquad (9)$$

13

Anisotropy is accounted for (Rino and Fremouw, 1977) by means of A, 3, and C, which are functions of θ and ϕ and of the irregularity axial ratios, a and b, and orientation angles (magnetic dip and off-L-shell angle).

Figure 4 shows V_e calculated from Equation (9) in WBMOD, employing the new velocity subroutine. The solid curve includes the effects of anisotropy inherent in the irregularity model, and the dashed one was calculated with a and b set to unity. Comparison of the latter with the solid curve in Figure 2 shows that it is identical to $V_\perp$ calculated from Equation (6), as it should be. We also calculated the nonisotropic V_e, in the receiver-centered coordinate system, employing only the angular components of scan velocity, which is intuitively the clear approach. The result is identical to the solid curve in Figure 4, indicating that the range-rate velocity component has been properly suppressed in the latter in the presence of aniso-tropy.

In addition to results from the new velocity subroutine, Figure 4 shows (dotted curve) V_e calculated in WBMOD prior to implementing the velocity correction described in the foregoing. The resulting curve approximates the correct one (solid) through much of the Goose Bay satellite pass employed, but it departs substantially at the higher penetration-point invariant latitudes. The high-latitude dip in effective velocity, which caused us to suspect a problem in the first place, was indeed the result of an error.
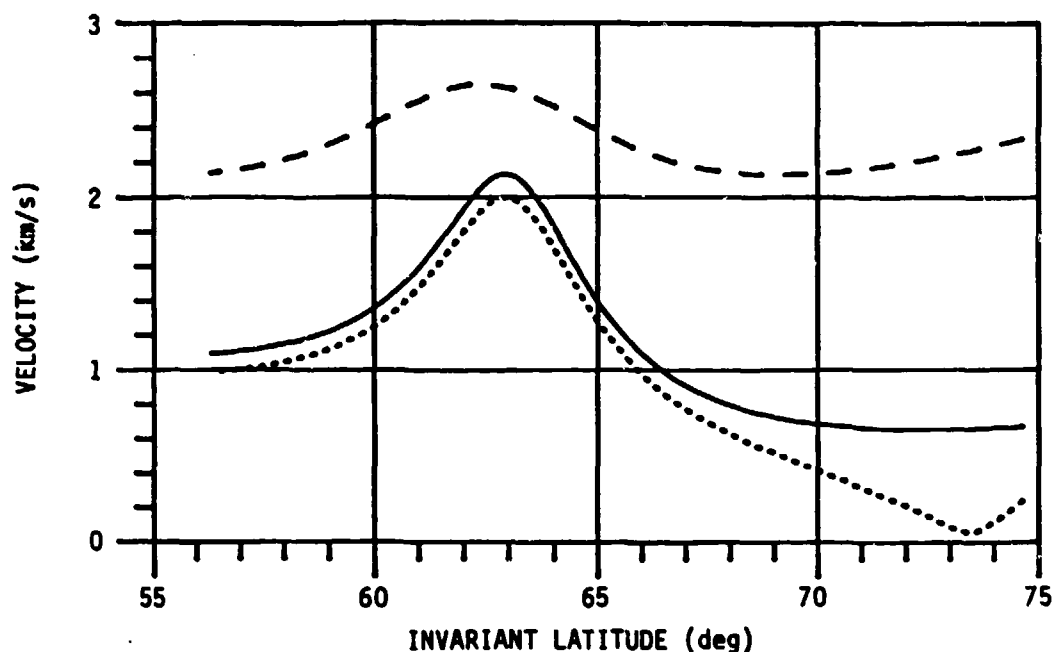
Figure 4. V_e calculated from new velocity subroutine for anisotropic (solid) and isotropic (dashed) irregularities. Note identity of latter to solid curve in Figure 2. Dotted curve represents incorrect V_e calculated for nonisotropic irregularities using old velocity subroutine.

14

The consequence of the velocity error on computation of phase scintillation was substantial in the Goose Bay pass at hand. The difference between the phase scintillation indices calculated from the same irregularity model using the new and old velocity routines is strikingly shown in Figure 5. The totally unexpected and peculiar null in rms phase fluctuation calculated with the old routine resulted solely from the velocity error.

The effect of the velocity error is quite different for different pass geometries, probably having close to its greatest impact in the geometry underlying Figures 2, 4, and 5. It is much less, for instance, in Figure 6, which contains phase scintillation indices calculated using the old (dotted) and new (solid) velocity subroutines for a nighttime Wideband pass essentially along the magnetic meridian over Goose Bay. The discontinuity in the dotted curve stemmed from insufficient numerical accuracy in the old velocity subroutine as the penetration point moved across the magnetic meridian. It too was remedied.
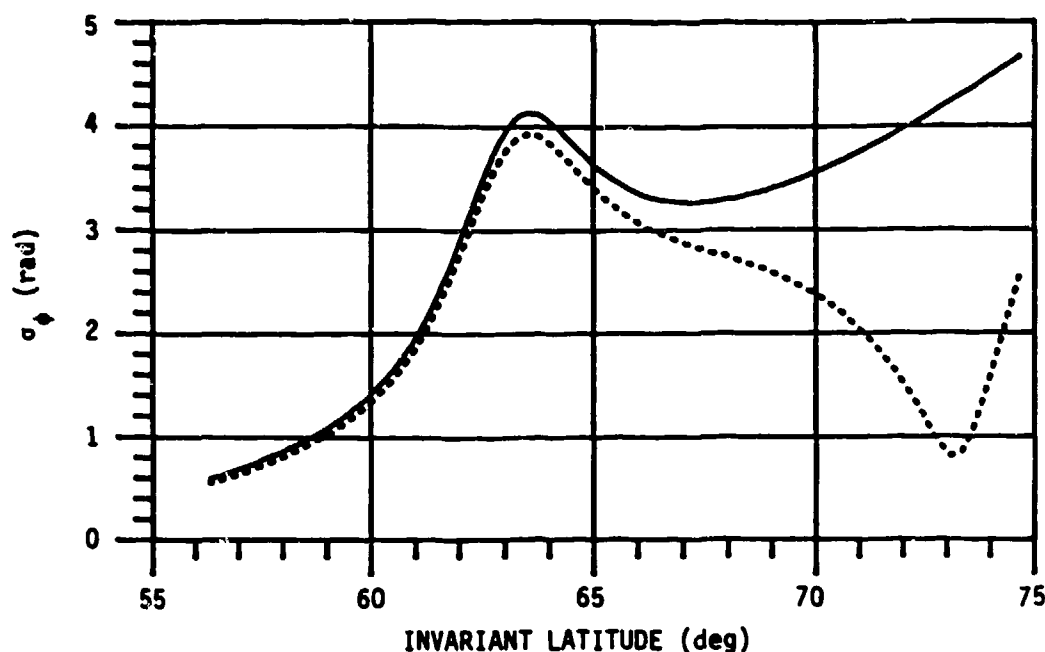
Figure 5. Phase scintillation index (rms fluctuation) calculated in WBMOD, using old (dotted) and new (solid) velocity subroutines, for nighttime pass of Wideband satellite east of Goose Bay.
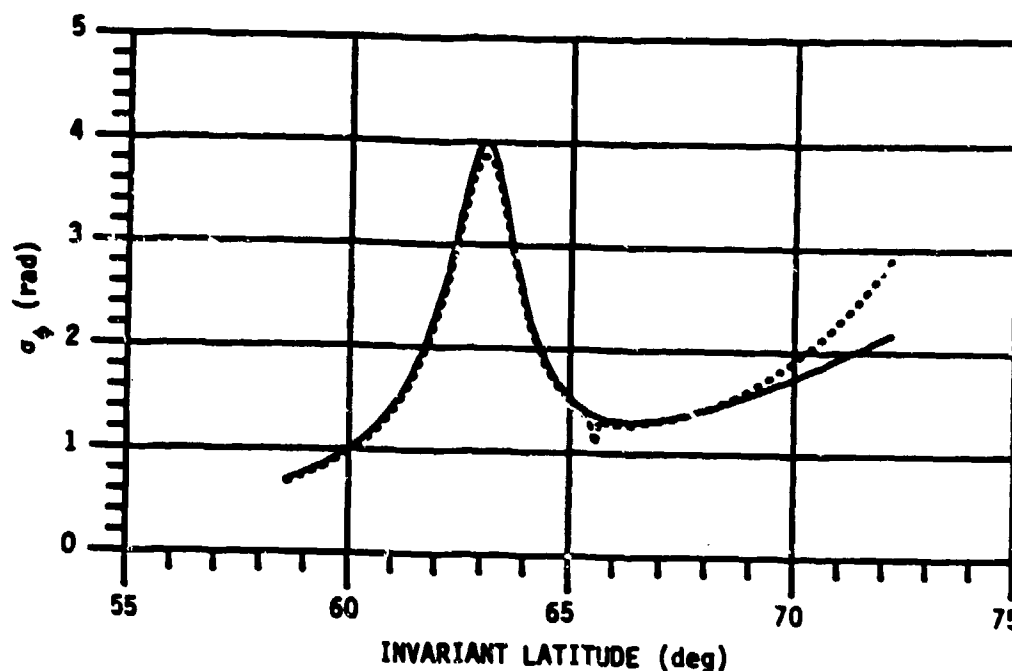
Figure 6. As in Figure 5, except for a nearly overhead pass along the magnetic meridian at Goose Bay. Again, the solid and dotted curves respectively show calculations using the new and old velocity subroutines.

2-3 ORBIT CALCULATION

During analysis of the scan velocity problem discussed in Section 2-2 and concurrent work on definition of the orbit of the HILAT satellite, algorithms were developed that would allow direct calculation of a circular orbit from two input satellite locations. These algorithms, implemented in subroutines STORB and LATLON, have replaced subroutines FNDORB, SRCHH, and SRCHT and functions SLAT and SLON (Rino et al, 1978).

Subroutine STORB calculates the necessary orbital parameters from input values of satellite altitude (h_s), two satellite locations (λ_1, ℓ_1, and λ_2, ℓ_2), and the time at the first location (t_1) as follows:

1. Calculate the orbital angular velocity of the satellite from

$$\Omega = 3600 \ \frac{\mu^{\frac{1}{2}}}{R_s^{\frac{3}{2}}} \ \text{radians/hour}$$

where

$$R_s = h_s + 6371.2 \ \text{km}$$
$$\mu = 3.986013 \times 10^5 \ \text{km}^3/\text{sec}^2.$$

2. Iteratively calculate the time at (λ_2, ℓ_2) from the orbital angular velocity, the angular distance between (λ_1, ℓ_1) and (λ_2, ℓ_2), and the earth's rotational angular velocity ($\Omega_e = \frac{2\pi}{24}$ radians/hour).

16

3. Correct the second longitude for the earth's rotation $\ell_2' = \ell_2 + \Omega_e(t_2 - t_1)$ and calculate the longitude (ℓ_0) and time (t_0) of the last ascending node and the orbital inclination angle (i) in a non-rotating frame as follows:

$$\ell_0' = \ell_1 - \tan^{-1} \frac{\tan \lambda_1 \cdot \sin(\ell_2'-\ell_1)}{\tan \lambda_2 - \tan \ell_1 \cos(\ell_2'-\ell_1)} \tag{10}$$

$$i = \frac{\pi}{2} - \tan^{-1} \frac{\sin(\ell_1 - \ell_0')}{\tan \lambda_1} \tag{11}$$

$$\tag{12}$$

$$t_0 = t_1 - \frac{\Phi}{\Omega}$$

where Φ is the angular distance along the orbit from $(0, \ell_0')$ to (λ, ℓ_1).

4. Revert to the rotating frame by correcting ℓ_0 with

$$\ell_0 = \ell_0' - \Omega_e(t_0 - t_1) \ .$$

The orbital parameters, Ω, i, ℓ_0, and t_0, are used by subroutine LATLON to calculate the sub-satellite location (λ, ℓ) for a given time, t, as follows:

1. Calculate the angular distance (Φ) along the orbit from $(0, \ell_0)$ using

$$\Phi = \Omega(t - t_0) \ .$$

2. Calculate the location from

$$\lambda = \sin^{-1}(\sin i \sin \Phi) \tag{13}$$

$$\ell = \ell_0 + \tan^{-1} \frac{\cos i \sin \Phi}{\cos \Phi} - \Omega_e(t - t_0). \tag{14}$$

These algorithms allow the user to generate a locally circular orbit that will approximate the trajectory of any actual satellite over a small section of its orbit.

2-4 IMPLEMENTATION AT AFGWC

One of the tasks carried out was to modify the most recent version of WBMOD (Rev 6A3) for operational use by the USAF Air Weather Service (AWS) at the Air Force Global Weather Central (AFGWC). Completion of this task required the following work:

1. Meet with AWS representatives at AFGWC to determine the requirements to be met by an operational version of WBMOD. These requirements were formalized in a Functional Description (Secan, 1982) and a project development plan.

2. Convert the existing WBMOD code to meet the ANSI X3.9-1978 FORTRAN standard and insert standardized in-line documentation.

3. Develop AFGWC-specific interface routines to interact with the AFGWC Space Environment Support Branch (AFGWC/WSE) Operations Center CRT and Data Communications Terminal (DCT) and the AFGWC Astrogeophysical Data Base (AGDB). Figure 7 shows an example of the input interaction between the AFGWC version of WBMOD and the user. Figure 8 is a sample of the output, which can be routed by the user to a local off-line printer (DCT).

4. Establish procedures for Physical Dynamics to provide AFGWC with model updates as they occur.

5. Write and publish system documentation in accordance with DoD Standard 7935.1-S (1977) (Secan, 1982).

6. Implement and test the reconfigured WBMOD at AFGWC. This included on-site training of AFGWC operations and programming staff members.

This task was begun on November 17, 1981, with a meeting at AFGWC and was completed on August 17, 1932, when the following items were provided to AFGWC:

1. Documentation required by DoD Standard 7935.1-S (Secan, 1982)

    Vol. I. Functional Description

    Vol. II. Users Manual

    Vol. III Program Maintenance Manual

    Vol. IV Test Plan

    Vol. V Test Analysis Report

2. A magnetic tape containing the latest version of WBMOD (6A3) as configured for use at AFGWC.

3. A list of the tape contents.

4. Baseline output samples for the non-equatorial cases listed in Appendix A of the Program Maintenance Manual.

All sections of WBMOD-6A3 were implemented at AFGWC, with the exception of equatorial-zone scintillation. This section of the model required further calibration. Rather than to provide scintillation estimates that were unreliable, it was decided to "switch off" the model internally within 25° of the dip equator. All involved personnel at AFGWC are aware of this temporary constraint.

2-5 IRREGULARITY DRIFT VELOCITY

2-5.1 Introduction

The WBMOD program has developed to where it provides reliable estimates of average scintillation strength for transionospheric radiowave systems with one terminus in low earth orbit. It contained a serious deficiency, however, for application to systems having a very high

```
IONOSPHERIC SCINTILLATION MODEL
(VERSION 6A3 - 18 FEB 1982 )
ENTER INITIAL UT DATE (MM DD YY)
11 25 80
ENTER F10 VALID FOR 25 NOV 80
150
ENTER INITIAL UT TIME (HHMM)
0000
**AP IS NOT AVAILABLE IN THE AGDB**
ENTER AP VALID FOR 25/0300UT NOV 80
40
ENTER SYSTEM OPERATING FREQUENCY (MHZ)
137.68
ENTER PHASE STABILITY DURATION TIME (SEC)
10
ENTER RECEIVER LOCATION
LAT(+NORTH)  LON(+EAST)   ALTITUDE(KM)
65.1 -147.5 0.2
ENTER INITIAL SATELLITE POSITION
LAT(+NORTH)  LON(+EAST)   ALTITUDE(KM)
0.0 -80.0 42240.0
ENTER RUN MODE DESIRED
 1:ORBIT  2:STEP PARAMETER   3:STEP RECEIVER
2
ENTER PARAMETER TO VARY
 1:TIME  2:AP  3:F10  4:FREG  5:SATELLITE LONGITUDE
5
ENTER FINAL SATELLITE LONGITUDE (+EAST)
-180.0
ENTER NUMBER OF INCREMENTS (50 MAX)
11
DO YOU WANT A SUMMARY OF INPUTS? (1:YES, 2:NO)
1
OPTION: STEP PARAMETER
DATE: 11/25/80      TIME: 0000 UT
F10: 150      AP:   40
SYSTEM PARAMETERS
  FREQUENCY:    137.7 MHZ
  RECEIVER LOCATION:  65.1/-147.5/ 0.20 KM
  SATELLITE LOCATION:   0.0/ -80.0/42240.0 KM
  ONE-WAY PROPAGATION
  PHASE STABILITY PERIOD:  10 SEC
VARIED PARAMETER (SLON)
  FINAL VALUE: -180.00
  NUMBER OF STEPS: 11
DO YOU WANT TO CHANGE ANY INPUTS? (1:YES, 2:NO)
2

    [Output List - See Figure 8]

DO YOU WANT A DCT COPY? (1:YES, 2:NO)
2
DO YOU WANT ANOTHER RUN? (1:YES, 2:NO)
2
WBMOD:FIN
```

Figure 7. Sample Input Interaction (Orbit Mode)

19

```
IONOSPHERIC SCINTILLATION MODEL (VERSION 6A3 - 18 FEB 1982 )
DATE: 06/13/82  TIME: 2230  F10: 120  AP:  40    FREQUENCY:    137.7 MHZ
RECEIVER: 65.1N,  147.5W,   0.20KM   SATELLITE: 80.0N,  85.1W,  1026.0KM
STABILITY PERIOD:   10SEC  ONE-WAY PROPAGATION  RUN MODE: ORBIT
```

STEP	TIME (UT)	AP	SATELLITE LATITUDE	LONGITUDE	SPECTRAL INDEX	STRENGTH	SCINTILLATION PHASE(RAD)	AMPL(S4)
1.	2230	40	80.00N	85.10W	2.5	0.0268	1.063	0.701
2.	2231	40	79.48N	98.00W	2.5	0.0240	1.005	0.660
3.	2231	40	78.87N	109.61W	2.5	0.0215	0.951	0.613
4.	2232	40	77.71N	119.40W	2.5	0.0199	0.916	0.561
5.	2233	40	76.28N	127.38W	2.5	0.0182	0.876	0.507
6.	2233	40	74.64N	133.82W	2.5	0.0169	0.845	0.456
7.	2234	40	72.87N	139.04W	2.5	0.0171	0.849	0.413
8.	2235	40	70.99N	143.30W	2.5	0.0192	0.900	0.385
9.	2235	40	69.04N	146.85W	2.5	0.0256	1.039	0.387
10.	2236	40	67.03N	149.83W	2.5	0.0662	1.671	0.467
11.	2237	40	64.98N	152.38W	2.5	0.3018	3.567	0.743
12.	2237	40	62.90N	154.59W	2.5	0.2107	2.981	0.709
13.	2238	40	60.79N	156.53W	2.5	0.0398	1.296	0.474
14.	2239	40	58.66N	158.25W	2.5	0.0141	0.771	0.391
15.	2239	40	56.51N	159.78W	2.5	0.0068	0.536	0.354
16.	2240	40	54.36N	161.17W	2.5	0.0039	0.403	0.327
17.	2241	40	52.19N	162.44W	2.5	0.0023	0.312	0.299
18.	2241	40	50.01N	163.61W	2.5	0.0014	0.242	0.262
19.	2242	40	47.82N	164.69W	2.5	0.0008	0.181	0.217
20.	2243	40	45.63N	165.69W	2.5	0.0004	0.130	0.168

Figure 8. Sample Output (Orbit Mode)

terminus (approaching geostationary altitude, for instance) due to the rudimentary treatment of the *in-situ* drift velocity, $\vec{V}_d$, of the ionospheric irregularities that produce radiowave scintillation. This deficiency, which was most severe at high latitudes, affected the calculated phase scintillation strength, T, through the dependence of T on the effective scan velocity, V_e, as shown in Equation (1) of Fremouw and Lansinger (1981). The effective scan velocity, in turn, is a function of the scan velocity, $\vec{V}_s$, of the propagation line of sight with respect to the scintillation-producing irregularities at the ionospheric penetration point (Rino, 1979), where $\vec{V}_s$ is a function of the satellite orbital velocity, $\vec{V}_0$, and the *in-situ* drift velocity. For a low-orbiting satellite ($h_s \sim 1000$ km), the velocity due to the orbital motion of the satellite is normally the dominant term in calculating $\vec{V}_s$. However, for slowly changing (i.e. high-orbit) receiver-transmitter geometries (and, as we will show later, for some rapidly changing geometries), the contribution from $\vec{V}_d$ is comparable to, or even dominant over, $\vec{V}_0$.

The drift velocity model used by WBMOD was a very rudimentary one. In meters/sec, it was as follows:

$$V_{dx} = 0 \tag{15a}$$

$$V_{dy} = 50 - 15 \left[1 + \mathrm{erf}\left(\frac{\lambda_I - 20}{3}\right)\right] + 40(1 + K_p)\left[1 + \mathrm{erf}\left(\frac{\lambda_I - \lambda_b}{3^\circ}\right)\right] \tag{15b}$$

$$V_{dz} = 0 \tag{15c}$$

where erf = error function,

   λ_I = invariant latitude,

   λ_b = invariant latitude of high-latitude scintillation boundary,

   K_p = 3-hourly planetary magnetic index,

and x, y, and z denote components in the geomagnetic north, east, and geocentric-nadir directions, respectively. Equations (15) describe an eastward drift of 50 m/sec at the geomagnetic equator, dropping to 20 m/sec, and increasing with geomagnetic activity at latitudes poleward of λ_b, with a maximum velocity of $20+80(1+K_p)$ m/sec. While this model is fairly representative of $\vec{V}_d$ at low geomagnetic latitudes, it is largely inadequate at latitudes poleward of the high-latitude plasma trough.

This simple model produces a (magnetic) eastward drift at all local times and latitudes, whereas the existence of a (nominally) two-celled plasma convection pattern with predominately anti-sunward flow across the polar cap with predominately sunward flow between the polar plasma-trough wall and equatorward of roughly 75° invariant has been accepted for at least the past decade (Cauffman and Gurnett, 1972; Heelis, 1982). It was decided, therefore, to survey the various two-cell convection models that have appeared in the literature and select one for

21

implementation in Program WBMOD.

The earliest models were the empirical high-latitude convection potential models developed by Heppner (1972) from OGO-6 observations, which have been the conceptual ancestor of most models that followed (Wolf, 1974; Volland, 1978; Kawasaki, 1975; Heppner, 1977; and Heelis et al, 1982). Of these recent models, that developed by Heelis et al (1982) proved to be the most flexible, both phenomenologically and computationally, and most applicable to the problem at hand.

2-5.2 Convection Potential Model

The convection potential model developed by Heelis et al (1982), henceforth denoted the HLS model, is an empirical model developed for use in an investigation of the effects of the convection flow on F-region plasma distributions. It is described in an offset invariant co-latitude, (θ), rotated magnetic local time (ϕ) coordinate system in which all local time boundaries are assumed to be along lines of constant θ. The electrostatic convection potential, ψ, is assumed to be of the form

$$\psi(\phi,\theta) = G(\theta)F(\phi,\theta) \tag{16}$$

where $G(\theta)$ and $F(\phi,\theta)$ represent the latitudinal and magnetic local time (MLT) variations of ψ respectively.

The function, $G(\theta)$, which contains the main latitudinal variations of ψ, is basically a $\sin^r\theta$ form with $r=2$ in the polar cap and $r=-4$ equatorward of the potential reversal boundary. Two transition regions, one on either side of the reversal boundary, are included to remove velocity discontinuities at the boundary. The exact form of $G(\theta)$ is shown in Appendix I. In these equations, θ_0 is the co-latitude of the reversal boundary; θ_1, and θ_2 $(\theta_1 > \theta_0 > \theta_2)$ are the equatorward and poleward boundaries of the two transition regions; and A_1, B_1, and A_2, B_2 are scale parameters, which are determined by equating the functions and their first derivatives at $\theta=\theta_1$ and $\theta=\theta_2$, respectively. The parameter θ_c is an additional scale parameter, denoted as a polar potential phase angle by HLS, which allows for a non-zero convection velocity at $\theta=0°$. (The determination of all model parameters is discussed in the next section.) Figure 9 shows an example of $G(\theta)$ for $\theta_1=22°$, $\theta_0=17°$, $\theta_2=15°$, $\theta_c=10°$.

The function, $F(\phi,\theta)$, which models the MLT variation of the potential, is more complex functionally than $G(\theta)$, but basically provides for constant potential along $\theta=$constant except in two regions, the dayside cusp and the nightside exit region. Appendix I gives the exact form of $F(\phi,\theta)$ implemented in WBMOD. These are slightly different from Equations (5) in HLS due to a slightly different implementation of (MLT). In these equations, ψ_m and ψ_e denote the potential extrema values along $\phi=6^h$ and $\phi=18^h$, respectively, ϕ_d is the MLT location of the center of the dayside cusp, $\phi_d^{\pm}$ are the width of the cusp along $\theta=\theta_0$, ϕ_n is the MLT location of the night exit region, and $\phi_n^{\pm}$ are the width of the exit region along $\theta=\theta_0$. Figure 10 shows $F(\phi,\theta_0)$ for
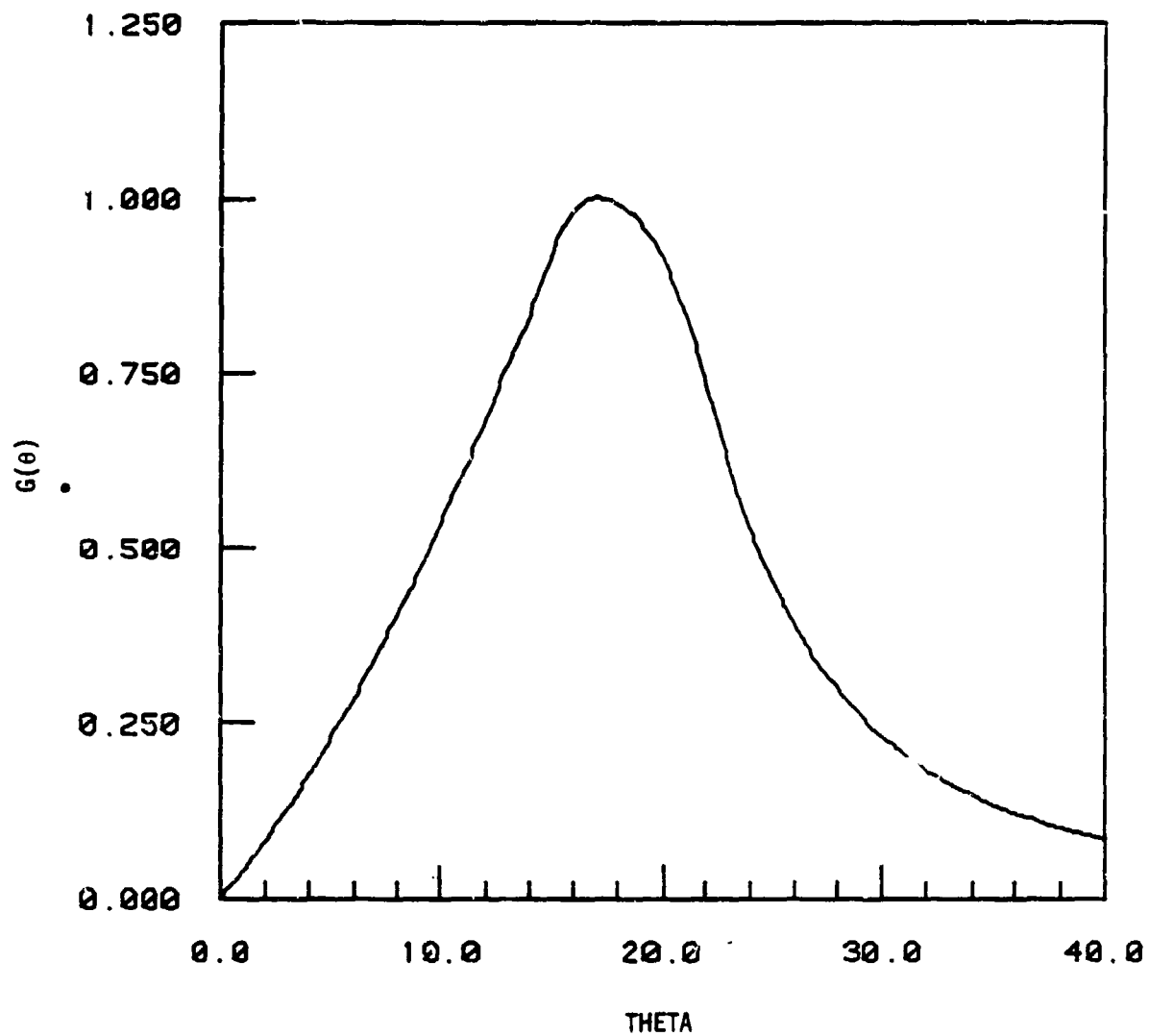
22

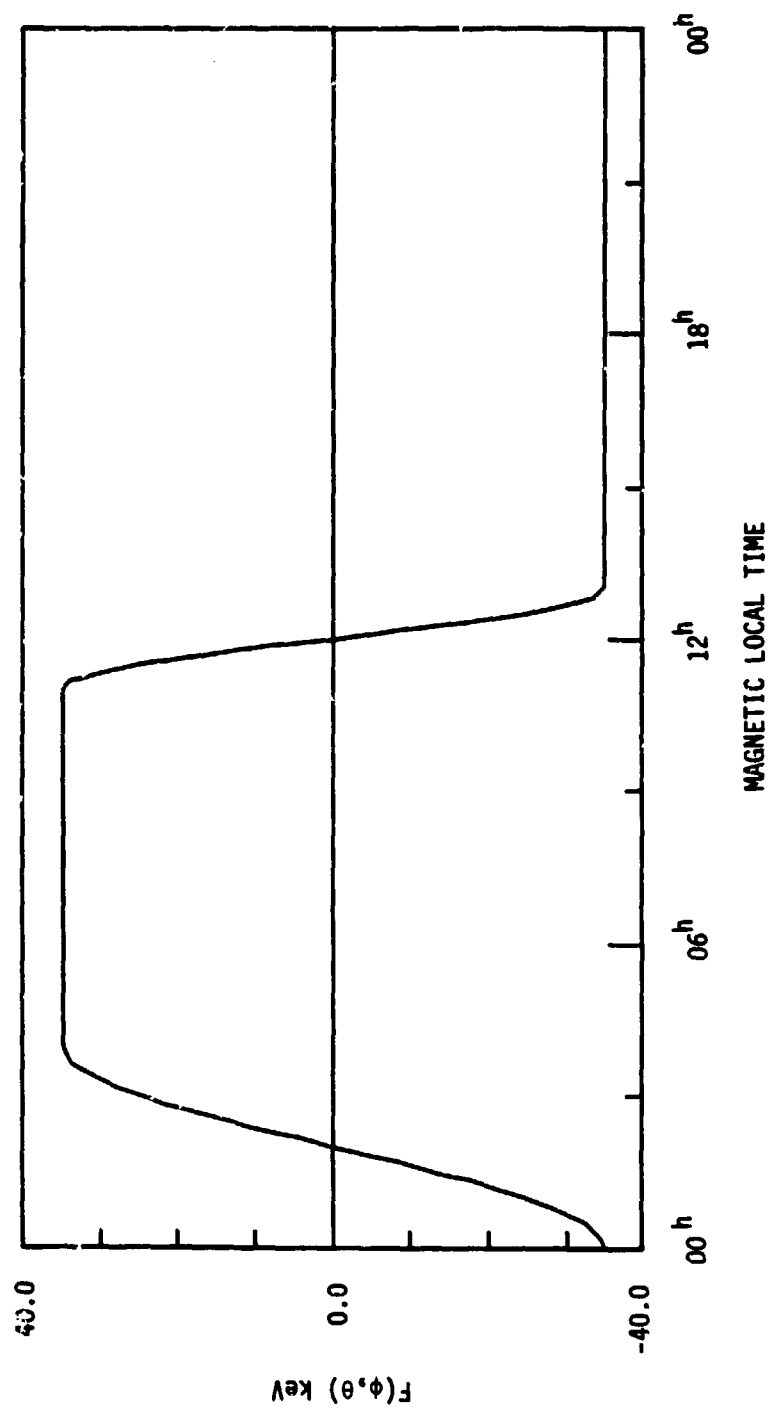Figure 9. The latitudinal function $G(\epsilon)$ ($\theta_1 = 22°$, $\theta_0 = 17°$, $\theta_2 = 15°$, $\theta_c = 10°$)

23

Figure 10. The local time function $F(\phi,\theta)$ $(\theta=\theta_0,\ \phi_d=12^h,\ \phi_d^{\pm}=1^h,\ \phi_n=02^h,\ \phi_n^{\pm}=2^h$

$\psi_m = 35$ kev, $\psi_e = -35$ kev, $\phi_d = 1200$ MLT, $\phi_d^{\pm} = 1^h$, $\phi_n = 0200$ MLT, and $\phi_n^{\pm} = 2^h$.

Figure 11 is an example of the polar-cap potential pattern as described by Equation (16) using the model parameters employed in Figures 9 and 10. Note that the center of the convection pattern is offset from the invariant pole. This is discussed in the following section on the selection of model parameter values.

2-5.3 Model Parameter Definition

One of the most attractive features of the HLS model is the large number (16) of essentially free parameters that allow the user to configure the model to fit observed conditions within the two-cell pattern framework. Table 1 is a list of these parameters with the values, or equations, to which they are set in the WBMOD drift model. Also included in Table 1 are the equations used to calculate three environmental parameters (ϵ, Q_e, and $\overline{K}_p$) from K_p if they are not input to the model.

The philosophy used in developing the values or functional forms shown in Table 1 was to (1) preserve as much as possible of the essential physics of the convection phenomenon in the choice of observables and model parameter functions, (2) develop expressions that would drive the model based on routinely available observable quantities, and (3) allow the entire model to be driven by a single geophysical observable, K_p, if no other data are available. This last criterion, established primarily with operationally oriented users such as AFGWC in mind, led to development of the expressions shown in Table 1 for ϵ, Q_e, and $\overline{K}_p$.

Since high-latitude convection is to a large extent "powered" by the magnetosphere and "braked" by the ionosphere, it seemed reasonable to search for a magnetospheric parameter to specify the "strength" of the convection (i.e., the cross-polar cap potential drop, $\Delta\psi$) and for auroral ionospheric boundaries to specify the orientation and boundary parameters (i.e., H_0, ϕ_0, θ_1, θ_0, θ_2, ϕ_d, $\phi_d^{\pm}$, ϕ_n, and $\phi_n^{\pm}$).

The most widely used quantity employed to specify the magnitude of magnetospheric (and, in turn, high-latitude) convection is the ϵ parameter developed by Perrault and Akasofu (1978) to study the transfer of energy from the solar wind to the earth's magnetosphere. Equation (17) in Table 1 for the cross-polar-cap potential drop is taken from Reiff et al (1981), who studied several parameters to employ in modeling $\Delta\psi$ and found a slightly modified version of ϵ to be the best. In this equation, ϵ is defined as

$$\epsilon = V_{sw} B^2 \sin^4 \frac{\theta_{sw}}{2} \quad nT^2\text{-km/sec} \tag{23}$$

where
V_{sw} = streaming velocity of the solar wind

θ_{sw} = solar wind $\vec{B}$ angle

B = minimum of $\left(B_{sw}, \frac{60nT}{f}\right)$

B_{sw} = solar wind magnetic field strength

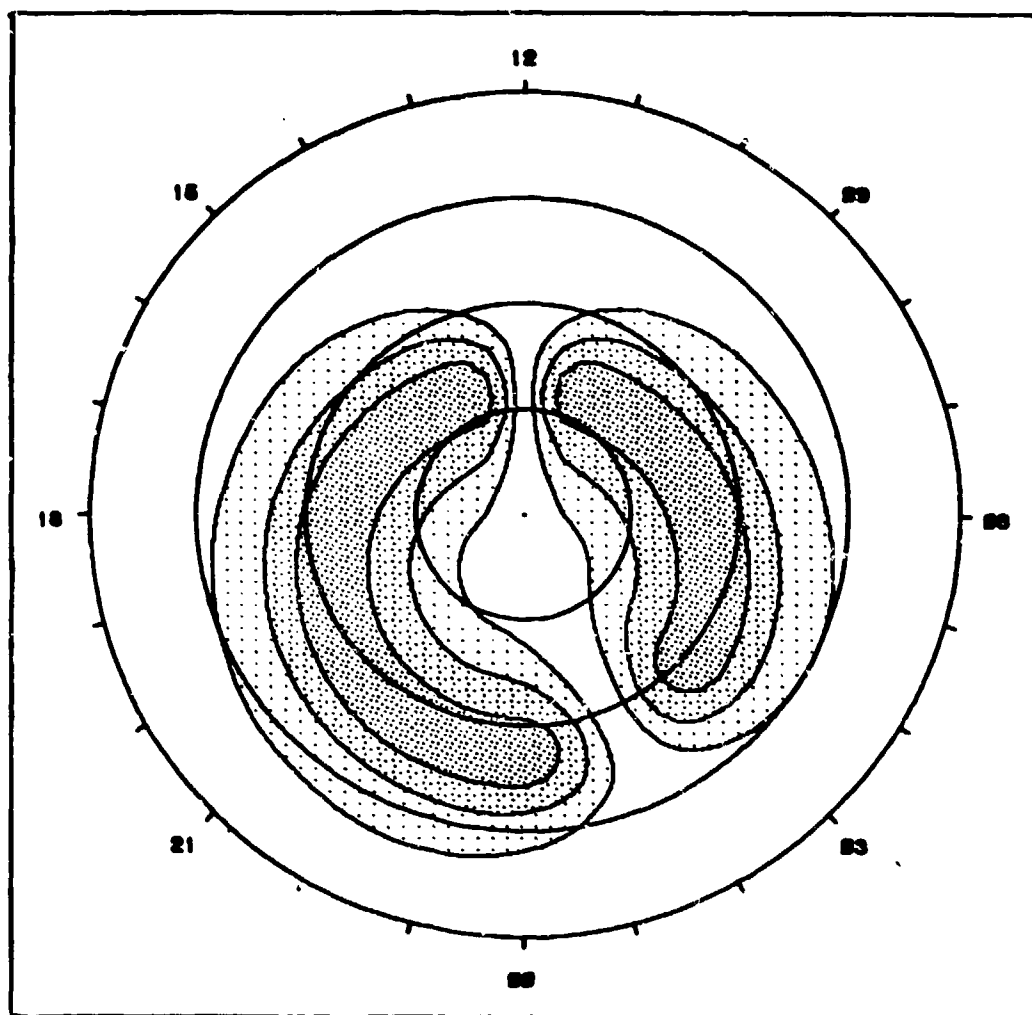f = amplication factor (= 7 for use in Equation (17)).

Figure 11. Potential pattern displayed in invariant latitude-magnetic local time coordinates. (Latitude circles are every 10° invariant; potential contours are every 10 keV with a maximum of +35 keV at 0600 MLT and a minimum of -35 keV at 1800 MLT.)

26

TABLE 1

POTENTIAL MODEL PARAMETERS

Parameters	Description	Value	Reference
θ_o	Invariant co-latitude of the convection-pattern center	$5°$	Meng et al (1977) Heelis et al (1980)
ϕ_o	Magnetic local time of the convection pattern center	00^h	(same)
ψ_m, ψ_e	Morning (0600 MLT) and evening (1800 MLT) extrema of the potential field (along $\theta = \theta_0$)	$\Delta\psi = (0.93\varepsilon - 319.)^k$ $\psi_m = +\Delta\psi/2$ $\psi_e = -\Delta\psi/2$	(17) Reiff et al (1981)
θ_2	Poleward edge of transition region	$\theta_2 = 17.0° - 1.7°\exp(-0.255q_e - 0.0113)$	(18) Holzworth and Meng (1975)
θ_0	Reversal boundary	$\theta_0 = \theta_2 + 2°$	Heelis et al (1980)
θ_1	Equatorward edge of transition region	(see text)	Dandekar (1979)
θ_c	Polar cap "phase angle"	$10°$	
r_1	Power-law parameter of -variation equatorward of 1	-4	Heelis et al (1982)
r_2	Power-law parameter of -variation poleward of 2	2	(same)
ϕ_d	Location of dayside cusp	11^h30^m	Meng (1981)
$\phi_d^{\pm}$	Width of cusp	$\pm 2^h$	Heelis et al (1976)
ϕ_n	Location of night exit region	$\phi_n = \phi_{no} - 0.6^h K_p$	(19) Zi and Nelson (1982), Zi et al (1982)
$\phi_n^{\pm}$	Width of night exit region	$\pm 2^h$	(same)

27

Environment Parameters

Symbol	Description	Equation		Reference
ε	Akasofu solar wind parameter	$\varepsilon = 181.7(K_p^2 + 3.08 K_p + 4.25)$	(20)	Rieff et al (1981), Heppner (1973)
Q_e	Effective auroral Q index	$Q_e = 1.35 K_p - 1.92$	(21)	Dandekar (1979)
$\bar{K}_p$	Average K_p index over past 24 hours	$\bar{K}_p = 1.1 + 0.67 K_p - 0.018 K_p^2$ where K_p is current three-hour value.	(22)	

The selection of ϵ as the parameter on which to model $\Delta\psi$ was based strongly on the desire to use geophysically meaningful parameters to drive the model. It violates to some extent, however, the desire to use readily (and operationally) available parameters. This is alleviated in the model through equation (20) in Table 1, in which ϵ is calculated as a function of K_p. This relationship, valid only in this application, was constructed from two algorithms for $\Delta\psi$:

$$\Delta\psi^2 = 0.93\epsilon - 319 \qquad \text{(Rieff et al, 1981)}$$
$$\Delta\psi = 20 + 13\ K_p \qquad \text{(Heppner, 1973)}. \tag{24}$$

This can be solved for $\epsilon(K_p)$ to produce equation (20). Note that Equation (20) is strictly a mathematical artifact which allows the model to use Equations (17) or (24) depending on the availability of ϵ.

Several studies have been made of the partitioning of $\Delta\psi$ between ψ_m and ψ_e (Heppner, 1972; Heppner, 1973; Rieff et al, 1981), and there is evidence of systematic asymmetries between $|\psi_e|$ and $|\psi_m|$, which can possibly be tied to the y-component of the solar wind, B_y. It was decided not to add this level of sophistication to the model, however, since no quantitative model of the variation of the asymmetry with B_y was found. Moreover, $\overset{\bullet}{B_y}$ is neither readily available for operational use nor can it be simply modeled in terms of some available parameter such as K_p, as ϵ is in equation (20). After reviewing the literature on this point, it was decided that $\psi_e = -\psi_m = \frac{1}{2}\Delta\psi$ is a reasonable default partitioning to use for now.

The first of the configuration parameters that require definition is the location (H_0, Φ_0) of the center of the convection pattern in invariant latitude-MLT. Although Heelis et al (1980) found the center of a circle fit to the location of the reversal boundary from atmospheric explorer data to be at ($4°$, 22^h40^m), it was decided for the time being to locate the center at ($5°\ 00^h$). This choice was made for the following reasons:

1) The latitudinal boundaries ($\theta_2, \theta_0, \theta_1$) are calculated as functions of various auroral boundaries based on auroral oval definitions from Holzworth and Meng (1975) and Meng et al (1977), who locate the center of the auroral boundaries at roughly ($5°, 00^h$).

2) As with the decision to ignore the seasonal variations inherent in the definitions of MLT (Section 2-1), it is better to stay simple rather than to add unnecessary (or even fictitious) variations to the model.

Several different ways of modeling θ_2, θ_0, and θ_1 were explored before settling on the method mentioned earlier. It was decided, based on Figure 7 of Heelis et al (1980), to model the poleward edge of the aurora and to locate the reversal boundary, θ_0, $2°$ equatorward of that. The expression used for the poleward edge of the aurora, Equation (18) in Table 1, was derived from the data presented in Table 2 of Holzworth and Meng(1975) showing the poleward edge of the statistical auroral oval (Feldstein, 1963) as a function of Q. The poleward transition boundary, θ_2, has been located at the poleward edge of the oval, as both Heelis et al (1982) and Volland (1978) placed θ_2 roughly $2°$ poleward of θ_0. In modeling θ_1, it was decided to use this

29

parameter to control the drop in $G(\theta)$ below θ_0 as a function of the equatorward edge of the auroral oval (θ_{ae}). Two empirical equations for θ_{ae} were extracted from figures in Dandekar (1979)

$$\theta_{ae} = 20.6 + 1.40 \, K_p \tag{25}$$

$$\theta_{ae} = 22.6 + 1.04 \, Q_e \tag{26}$$

from which Equation (21) in Table 1 was constructed in the same manner (and with the same caveats) as $\varepsilon(K_p)$ was derived. Once θ_{ae} is calculated from either Equation (25) or (26), θ_1 is determined by defining it as the value needed to drop $G(\theta)$ to 0.1 at $\theta_{ea + 1}^\circ$ if there were no transition zone. This leads to an equation

$$\sin \theta_1' = \left| 0.1(1 + 4 \cot \theta_1)^{\frac{1}{2}} \right|^{\frac{1}{4}} \sin(\theta_{ea} + 1^\circ) \tag{27}$$

which is solved iteratively for θ_1. (It should be noted that neither transition boundary has any physical significance. They are included only to avoid discontinuous behavior of $\vec{V}_D$ near the reversal boundary, and they affect the model potential configuration primarily through slight changes in the equatorward shape of $G(\theta)$).

The values listed in Table 1 for the location and local-time width of the dayside cusp were taken from Heelis et al (1976), who found the cusp reversal region to be roughly $3\frac{1}{2}$ to 4 hours wide, and from Meng (1981), who located the cusp centered at roughly $11^h 30^m$ MLT. No evidence was presented for moving the cusp center MLT (ϕ_d) with magnetic activity.

The location of the night exit region, however does apparently move toward the evening sector with increasing activity (Zi and Nelson, 1982). The constants in Equation (19) in Table were developed in two steps. The movement of ϕ_n with $\overline{K}_p$, the mean K_p over the preceding 24 rs, was taken from Figure 4c of Zi and Nelson (1982). The value of ϕ_n for $K_p = 0o$, ϕ_{no}, was determined by iteratively changing ϕ_{no} until the model produced the observed location of ϕ_n as in this same figure. The widths of the exit region, $\phi_n^\pm$, are currently set to $\pm 2^h$ as a compromise to the two examples given by Heelis et al (1982) in their Figure 6.

For completeness, and in line with the philosophy stated earlier, a relationship was developed between $\overline{K}_p$ and K_p (Equation (22)). This was developed by constructing a quadratic least-squares fit to three years of K_p data (1976-1978). (Interestingly, this equation is nearly identical to one developed early in the model development in which the value of K_p was assumed to tend toward 3 as one went back 24 hours from the current K_p value. The equation from this simple model was $\overline{K}_p = 1.1 + 0.60 \, K_p - 0.016 \, K_p^2$.)

The power-law parameters, r_1 and r_2, were set to values suggested by Heelis et al (1982). The value for θ_c suggested (14°) was decreased to 10° to avoid undesirable behavior should θ_c be greater than θ_2.

Table 2 lists the values for $\overline{K}_p$, Q, ϵ, θ_1, θ_0, θ_2, θ_{ap}, ψ_m, and ϕ_n, as calculated from the equations presented in Table 1 for K_p values 0 through 9. Figures 12-14 are examples of the convection potential pattern produced by this implementation of the HLS model for $K_p=2o$, 3+, and 6o.

The functions and values of all model prameters can, and most likely will, be changed as the model is used in this new application. As will be discussed below, the most likely candidates for change are the parameters that describe the location and width of the night exit region.

2-5.4 Drift Velocity Calculation

The plasma drift velocity is calculated from

$$\vec{V}_d = \frac{\vec{E}_c \times \vec{B}}{B^2} \tag{28}$$

where $\vec{E}_c = - \nabla\psi(\phi,\theta)$ and $\psi(\phi,\theta)$ is calculated from Equation (16). This leads to

$$\vec{E}_c = \vec{E}_\theta\hat{\theta} + E_\phi\hat{\phi} = - \frac{1}{r_p}\frac{\partial\psi}{\partial\theta}\hat{\theta} - \frac{1}{r_p\sin}\frac{\partial\psi}{\partial\phi}\hat{\phi} \tag{29}$$

where $r_p = R_e + h_p = 6721$ km. From Equation (16)

$$\frac{\partial\psi}{\partial\theta} = F(\phi,\theta)\frac{\partial G(\theta)}{\partial\theta} + G(\theta)\frac{\partial F(\phi,\theta)}{\partial\theta} \tag{30a}$$

$$\frac{\partial\psi}{\partial\phi} = G(\theta)\frac{\partial F(\phi,\theta)}{\partial\phi} \tag{30b}$$

the form of the deriviatives of $G(\theta)$ and $F(\phi,\theta)$ implemented in Program WBMOD are given in Appendix I. The coordinate system in which the potential is defined has its r-axis aligned along $\vec{B}$, so Equation (28) becomes

$$\vec{V}_d = \frac{E_\phi}{B}\hat{\theta} - \frac{E_\theta}{B}\hat{\phi} \tag{31}$$

where

$$E_\theta = - \frac{1}{r_p}\left[F(\phi,\theta)\frac{\partial G(\theta)}{\partial\theta} + G(\theta)\frac{\partial F(\phi,\theta)}{\partial\theta}\right]$$

$$E_\phi = - \frac{G(\theta)}{r_p\sin}\frac{F(\phi,\theta)}{\partial\phi}.$$

Figure 15 shows $\vec{V}_d$ calculated from Equation (31) plotted in the (θ,ϕ) potential-model coordinate system, for $K_p=4o$.

31

TABLE 2

K_p	$\bar{K}_p$	Q	ε	θ_2	θ_0	θ_1	θ_{ae}	$\Delta\psi$	ϕ_n
0o	1.16	-1.92	7.73E 02	14.3	16.3	16.2	20.6	2?.3	1.34
0+	1.36	-1.47	9.73E 02	14.6	16.6	17.1	21.1	24.3	1.21
1-	1.54	-1.02	1.22E 03	14.8	16.8	17.4	21.5	28.7	1.08
1o	1.73	-0.57	1.51E 03	15.1	17.1	17.7	22.0	33.0	0.95
1+	1.96	-0.12	1.86E 03	15.3	17.3	18.0	22.3	37.3	0.82
2-	2.17	0.33	2.21E 03	15.5	17.5	18.3	22.9	41.7	0.70
2o	2.37	0.78	2.65E 03	15.6	17.5	18.6	23.4	46.0	0.58
2+	2.57	1.23	3.07E 03	15.8	17.8	19.0	23.9	50.3	0.46
3-	2.76	1.68	3.56E 03	15.9	17.7	19.3	24.3	54.7	0.34
3o	2.95	2.13	4.09E 03	16.0	18.0	19.6	24.8	59.0	0.23
3+	3.13	2.58	4.66E 03	16.1	18.1	19.9	25.3	63.3	0.12
4-	3.31	3.03	5.27E 03	16.2	18.2	20.2	25.8	67.7	0.01
4o	3.49	3.48	5.92E 03	16.3	18.3	20.5	26.2	72.0	23.90
4+	3.87	3.93	6.61E 03	16.4	18.4	20.8	26.7	76.3	23.80
5-	3.83	4.38	7.34E 03	16.4	18.4	21.1	27.2	80.7	23.70
5o	4.00	4.83	8.11E 03	16.5	18.5	21.4	27.6	85.0	23.60
5+	4.16	5.28	8.93E 03	16.6	18.6	21.7	28.1	89.3	23.50
6-	4.32	5.73	9.78E 03	16.6	18.6	22.0	28.6	93.7	23.41
6o	4.47	6.18	1.07E 04	16.7	18.7	22.3	29.0	98.0	23.32
6+	4.62	6.63	1.16E 04	16.7	18.7	22.5	29.5	102.3	23.23
7-	4.77	7.08	1.26E 04	16.7	18.7	22.8	30.0	106.7	23.14
7o	4.91	7.53	1.36E 04	16.8	18.8	23.1	30.4	111.0	23.06
7+	5.05	7.98	1.46E 04	16.8	18.8	23.4	30.9	115.3	22.97
8-	5.18	8.43	1.57E 04	16.8	18.8	23.7	31.4	119.7	22.89
8o	5.31	8.88	1.67E 04	16.8	18.8	24.0	31.8	124.0	22.82
8+	5.43	9.33	1.81E 04	16.8	18.8	24.3	32.3	128.3	22.74
9-	5.55	9.78	1.93E 04	16.9	18.9	24.6	32.8	132.7	22.67
9o	5.67	10.23	2.05E 04	16.9	18.9	24.8	33.2	137.0	22.60

Potential Model Parameters as a Function of K_p

32
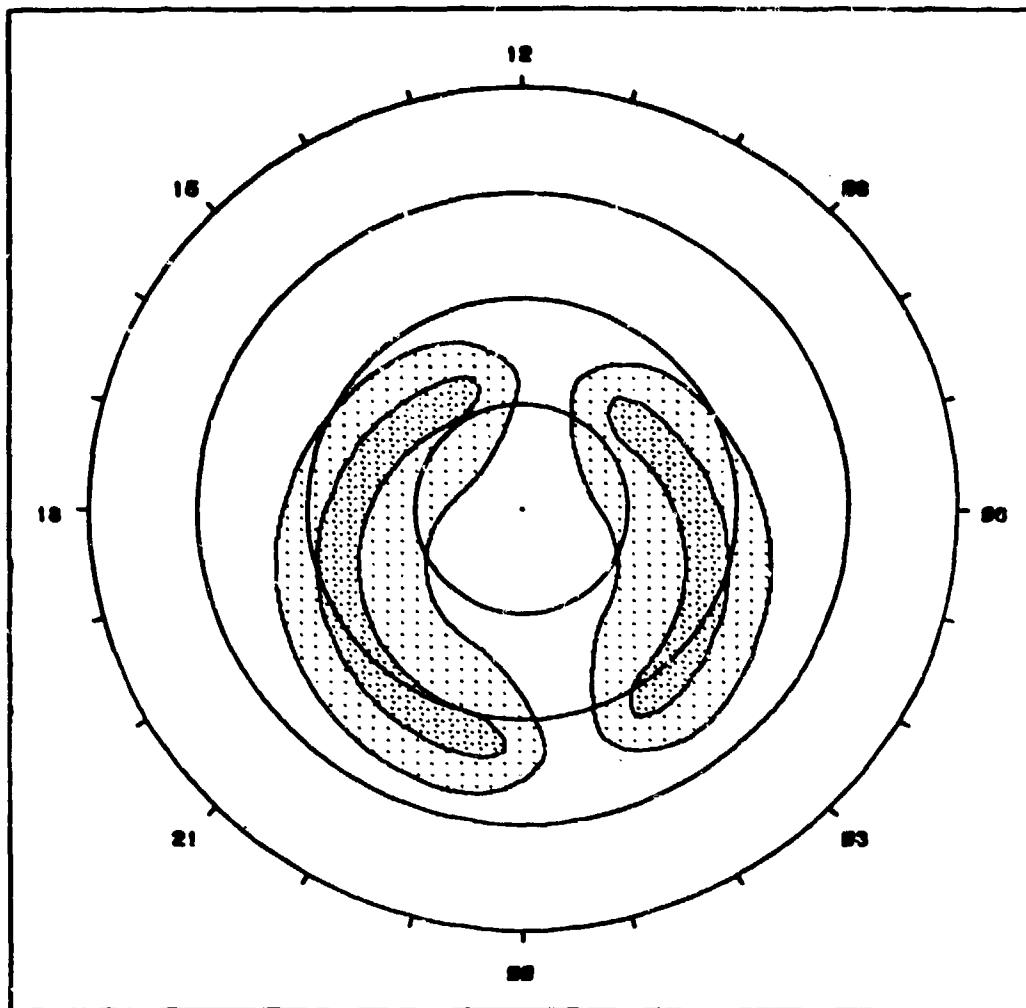
Figure 12. Potential pattern as plotted in Figure 11 using model parameters defined in Table 1 for $K_p = 2°$.
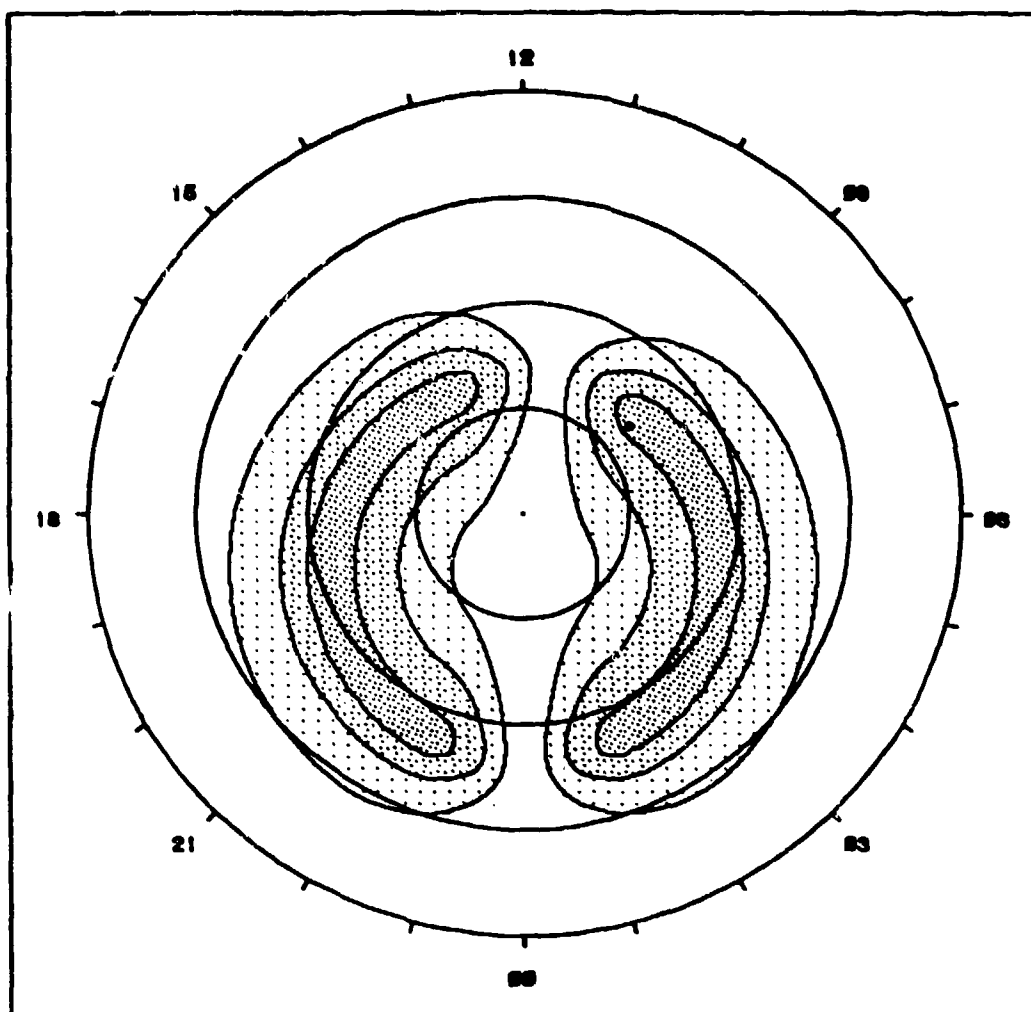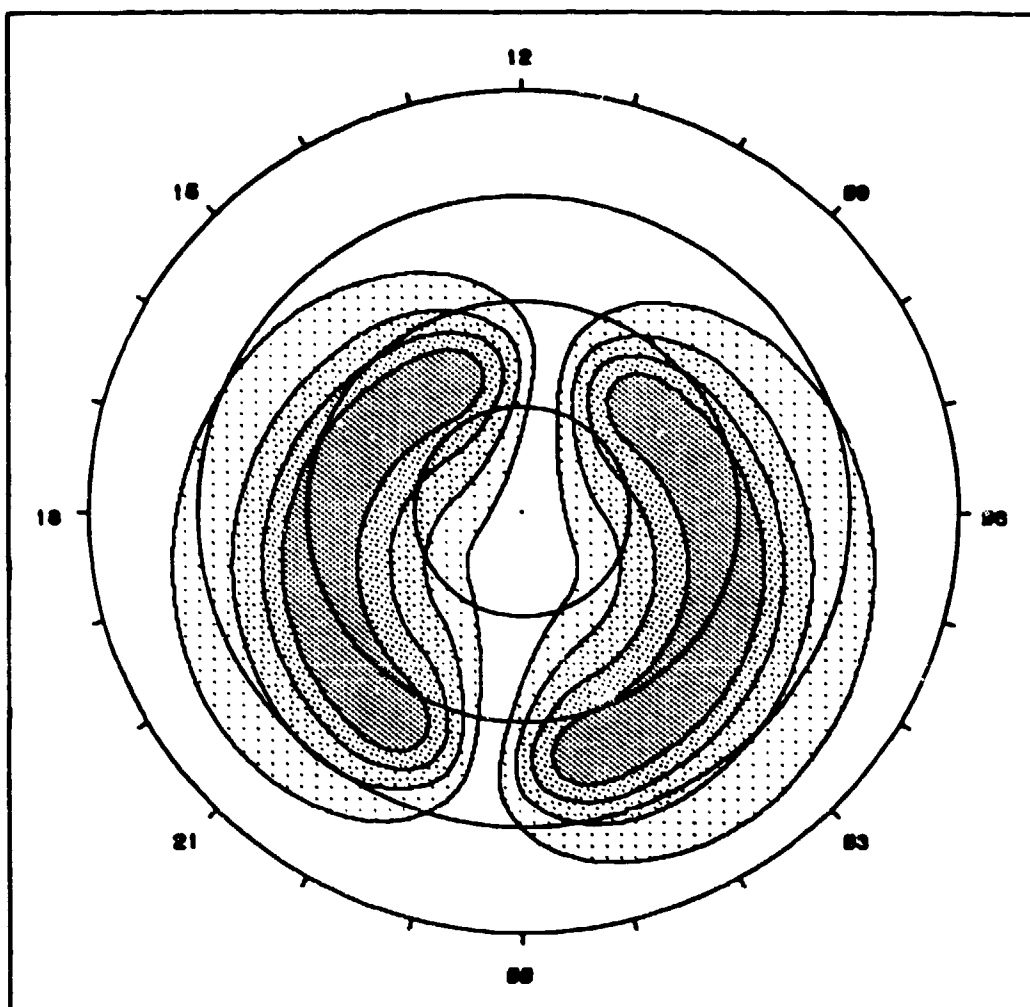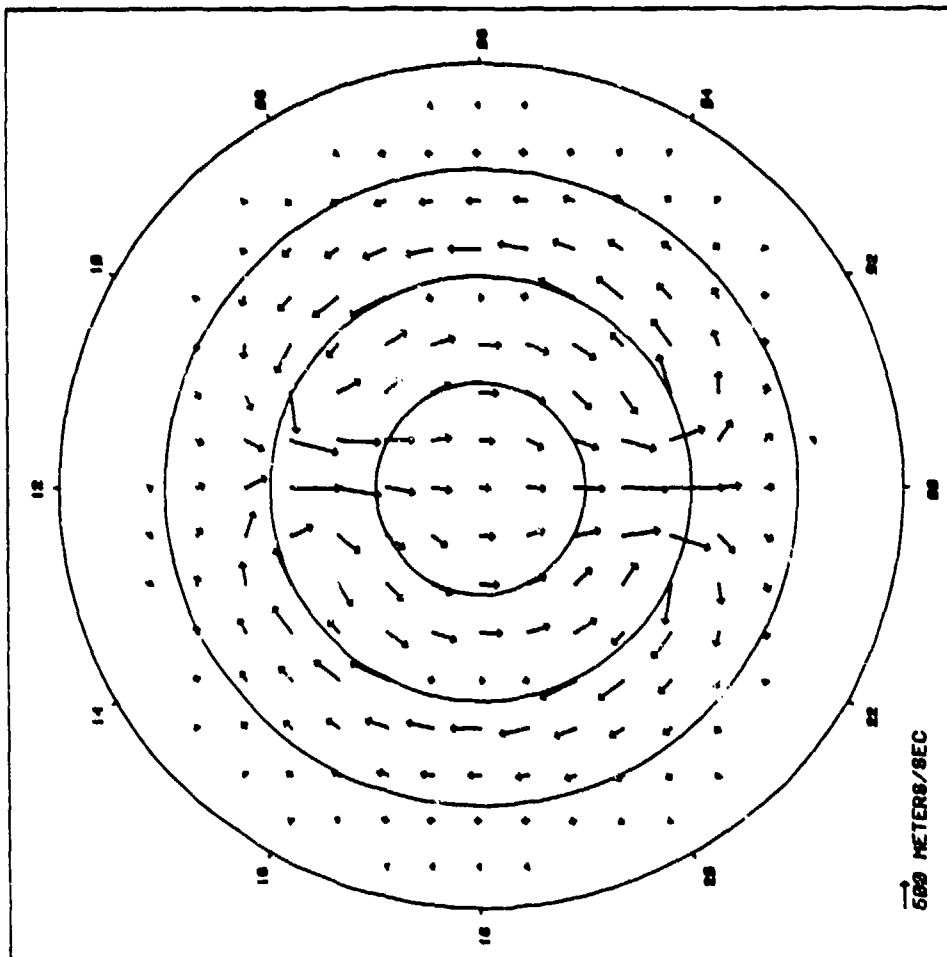
Figure 13.   Same as Figure 12 for K_p=3+.

Figure 14. Same as Figure 12 for K_p=6°.

35

IRREGULARITY DRIFT VELOCITY
(HLS POTENTIAL MODEL)

ENVIRONMENT DATA

KP: 4.65
MKP: 3.40
QE: 3.5
EPS: 8.66E+84 (nT**2-KV/SEC)

MAX POTENTIAL: 36.0 kV

COORDINATE SYSTEM

THETA: POTENTIAL MODEL
PHI: POTENTIAL MODEL

500 METERS/SEC

Figure 15. Drift velocity in the (θ,φ) potential-model coordinate system. The concentric circles represent each 10° in θ.

The final step in the calculation is to transform the drift velocity calculated in Equation (31) to the coordinate system used in WBMOD. The coordinate system of Equation (31) has $+\hat{r}$ aligned along $-\vec{B}$, $+\hat{\theta}$ magnetic south, $+\hat{\phi}$ magnetic east, while WBMOD uses $+\hat{x}$ magnetic north, $+\hat{y}$ magnetic east, and $+\hat{z}$ along the (geocentric) nadir. The transformation equations are

$$V_{dx} = -V_{d\theta} \sin d \cos \beta - V_{d\phi} \sin \beta \tag{33a}$$

$$V_{dy} = -V_{d\theta} \sin d \sin \beta + V_{d\phi} \cos \beta \tag{33b}$$

$$V_{dz} = V_{d\theta} \cos d \tag{33c}$$

where V_d and V_d are the drift velocity components in the potential coordinate system, V_{dx}, V_{dy}, V_{dz} are the components in the WBMOD coordinate system, d is the magnetic dip (inclination) angle and β is the angle between $\hat{x}$ and $\hat{\theta}$ given by

$$\cos \beta = \left[\frac{\cos H_0 - \cos \theta_p \cos \theta_I}{\sin \theta_p \sin \theta_I} \right] \tag{33}$$

where $H_0 = 5°$ (from Table 3), θ_p is the potential-model θ coordinate, and θ_I is the invariant co-latitude. Figure 16 shows the $\vec{V}_d$ plotted in Figure 15 after the transformation shown in Equations (33). This figure (and others that follow) is ploted such that the $0°$ magnetic meridian is always at the bottom of the picture, so the $\vec{V}_d$ pattern shown is rotated according to the input Greenwich Mean Time (UT) shown on the figure.

The final form of the *in-situ* drift velocity implemented in WBMOD transitions from the drift velocity given by Equations (33) to the old form given by Equations (15) at the location of the sub-auroral scintillation boundary, λ_b (see Section 3.2). The final equations are then

$$V_{dx} = V'_{dx} + \rho V_{dxo} \tag{35a}$$

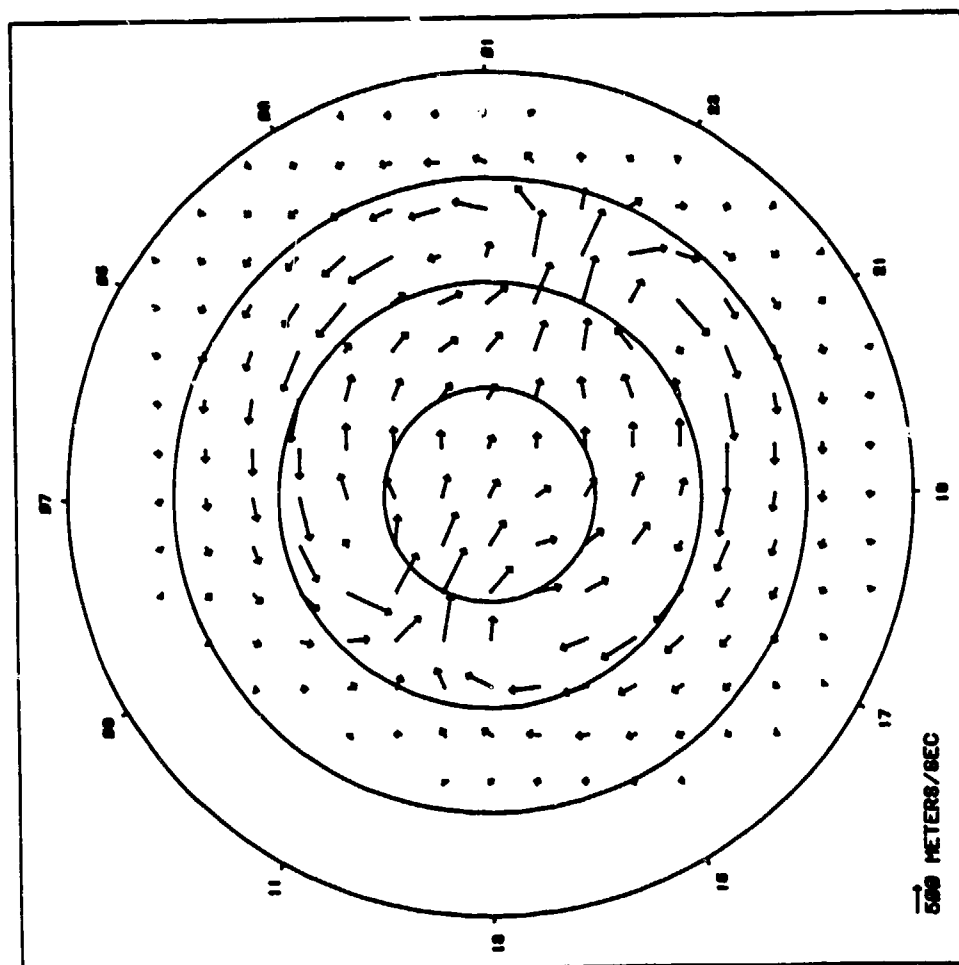$$V_{dy} = V'_{dy} + \rho V_{dyo} \tag{35b}$$

$$V_{dz} = V'_{dz} + \rho V_{dzo} \tag{35c}$$

where the primed velocities are from Equations (33); V_{dxo}, V_{dyo}, and V_{dzo} are the mid-latitude velocities from Equations (15), and ρ is given by

$$\rho = \text{erf} \left(\frac{\lambda_I - \lambda_b}{W_h} \right)$$

where λ_I is invariant latitude, λ_b is the scintillation boundary invariant latitude, and W_h is

37

Figure 16. Drift velocity from Figure 15 transformed into WBMOD coordinate system (invariant latitude and MLT).

the transition width. Figures 17 and 18 show the drift velocities calculated from Equations (35) for K_p = 3o at 1200UT and K_p = 6o at 1200UT respectively.

2-5.5 Effects on RMS Phase Calculations

The drift-velocity model described above recently has been implemented in WBMOD (Rev 6B3), and we have begun to assess its effects on the rms phase fluctuation, σ_ϕ, calculated in WBMOD. Results to date are tentative, but a number of interesting manifestations of this new $\vec{V}_d$ model have turned up.

Figure 19, a plot of σ_ϕ for K_p=3o for both the old (6A3) and new (6B3) models, illustrates the minimal effect expected from the new $\vec{V}_d$ for a low-orbiting satellite case (simulated Poker Flat night-overhead Wideband pass). Figure 20, however, for the same geometry but a K_p of 8o, shows an unexpected decrease in the calculated σ_ϕ by roughly a factor of two. The cause of this decrease is the addition by the new model for $\vec{V}_d$ of a V_{dx} comparable to V_x due to the satellite motion, which drops, by roughly 45%, the effective velocity, V_e, calculated for K_p=8o. (Recall, from Equation 15a, that V_{dx}=0 for the old $\vec{V}_d$ model). The source of this V_{dx}, and the reason that little change occurred for K_p=3o , can be seen in Figures 21 and 22. These figures show the track of the penetration point plotted over the drift velocity patterns for K_p=3o and 8o respectively. In the K_p=3o case, the track lies westward of the exit region; the majority of the drift velocity is cross-track, as calculated (roughly) by the old model. For K_p=8o the track lies within the exit region, however, and the drift velocity is almost entirely along-track, effectively reducing the irregularity scan velocity.

This effect is different at different receiver longitudes. Figures 23 through 26 are the same as 19 through 23, but for a simulated Goose Bay night-overhead pass. In this case, the differences in σ_ϕ for K_p=3o are more noticeable than for Poker Flat, and the decrease in σ_ϕ at K_p=8o is less. As can be seen in the corresponding $\vec{V}_d$ pattern plots, the cause of the different behavior is due to a different geometry vis-a-vis the drift velocity pattern. The track for the K_p=3o case at Goose Bay is within the exit region and has an appreciable V_{dx}, while at K_p=8o the track has moved closer to the edge of the exit region, so that the along-track drift velocity is less than it was at Poker Flat for K_p=8o.

In another test of the model, an attempt was made to reproduce the results of a study (Basu et al, 1982) of the phase scintillation statistics on a 244-MHz link between Goose Bay and FLEETSAT, a geostationary satellite at (nominally) 100°W longitude. Figure 27 shows a plot of median diurnal curves of observed σ_ϕ for $K_p > 3.5$ and average model σ_ϕ for K_p=6o. The dashed curves are for Jan-Apr 1979 (upper curve) and Aug-Nov 1979 (lower curve) from Figures 3b and 5b, respectively, of Basu et al (1982), and the solid curve is from WBMOD (Rev 6B3). There is

IRREGULARITY DRIFT VELOCITY
(HL8 POTENTIAL MODEL)
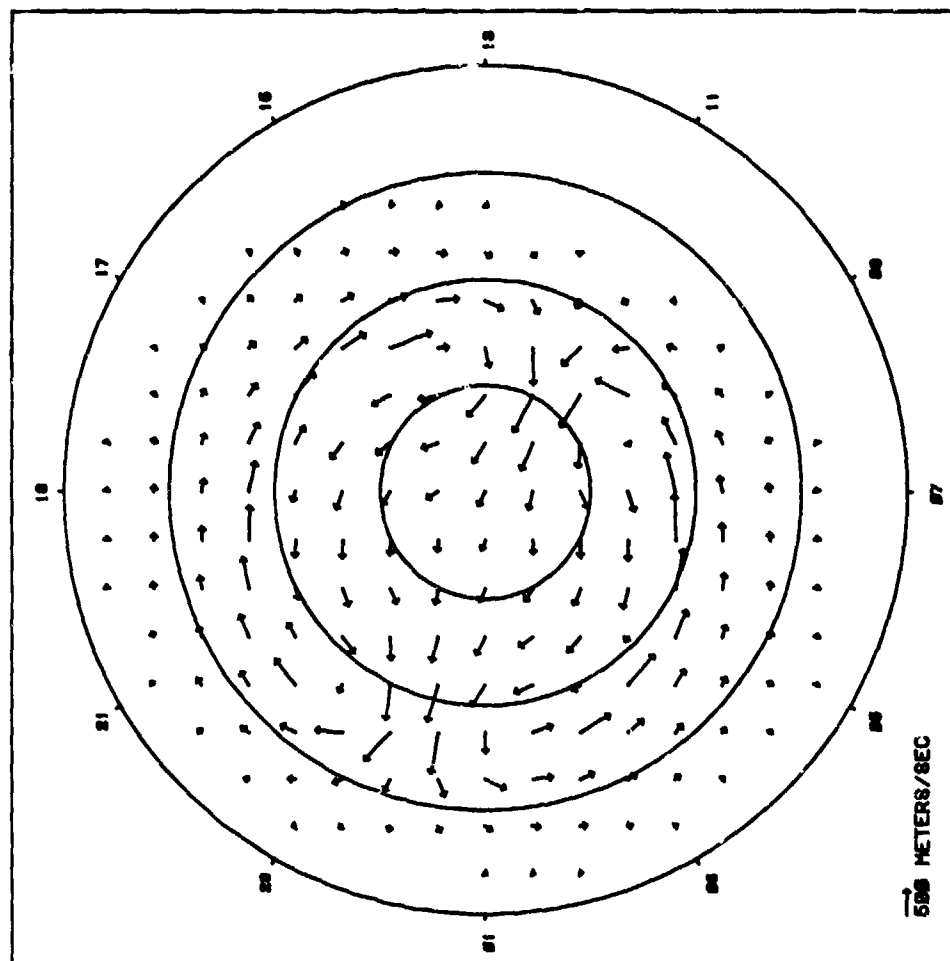
ENVIRONMENT DATA
  KP: 3.99
  MKP: 2.86
  OE: 2.1
  EPS: 8.41E+84 (nT**2-KM/SEC)

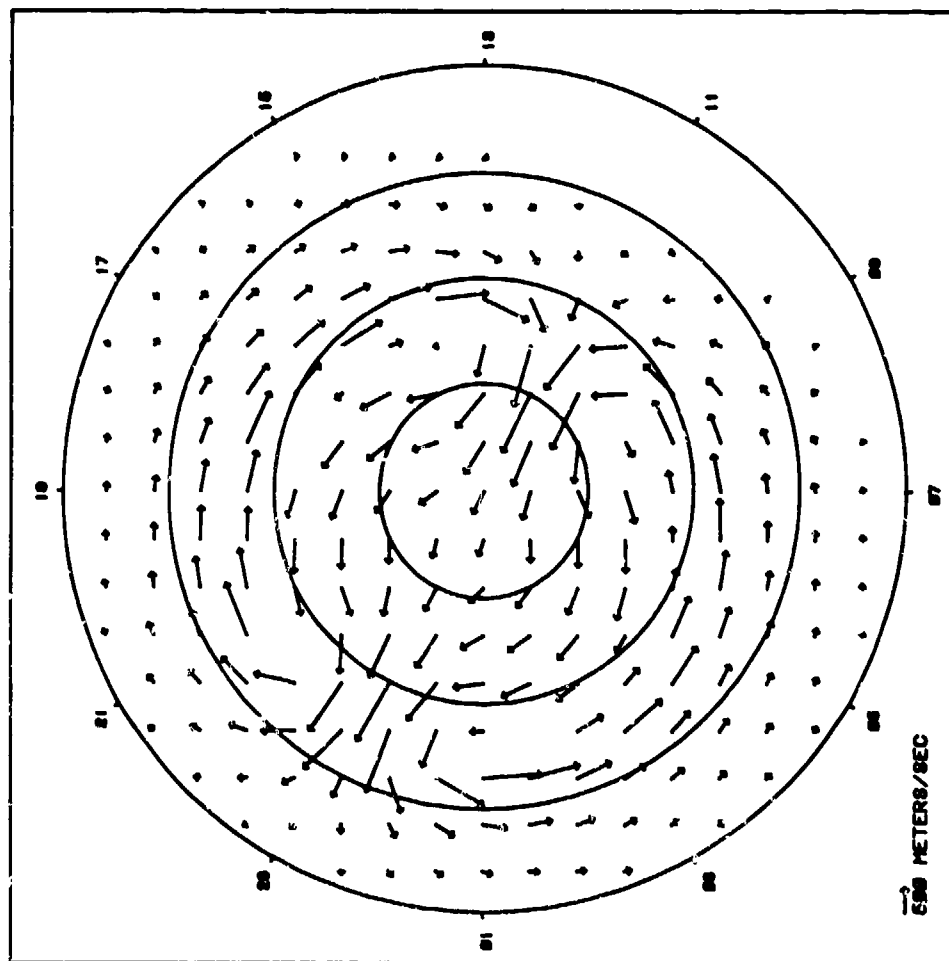MAX POTENTIAL: 28.6 kV

COORDINATE SYSTEM
  THETA: INVARIANT LATITUDE
  PHI: MAGNETIC LOCAL TIME
  UT: 1288

Figure 17. Drift velocity for K_p=3o at 1200 UT.
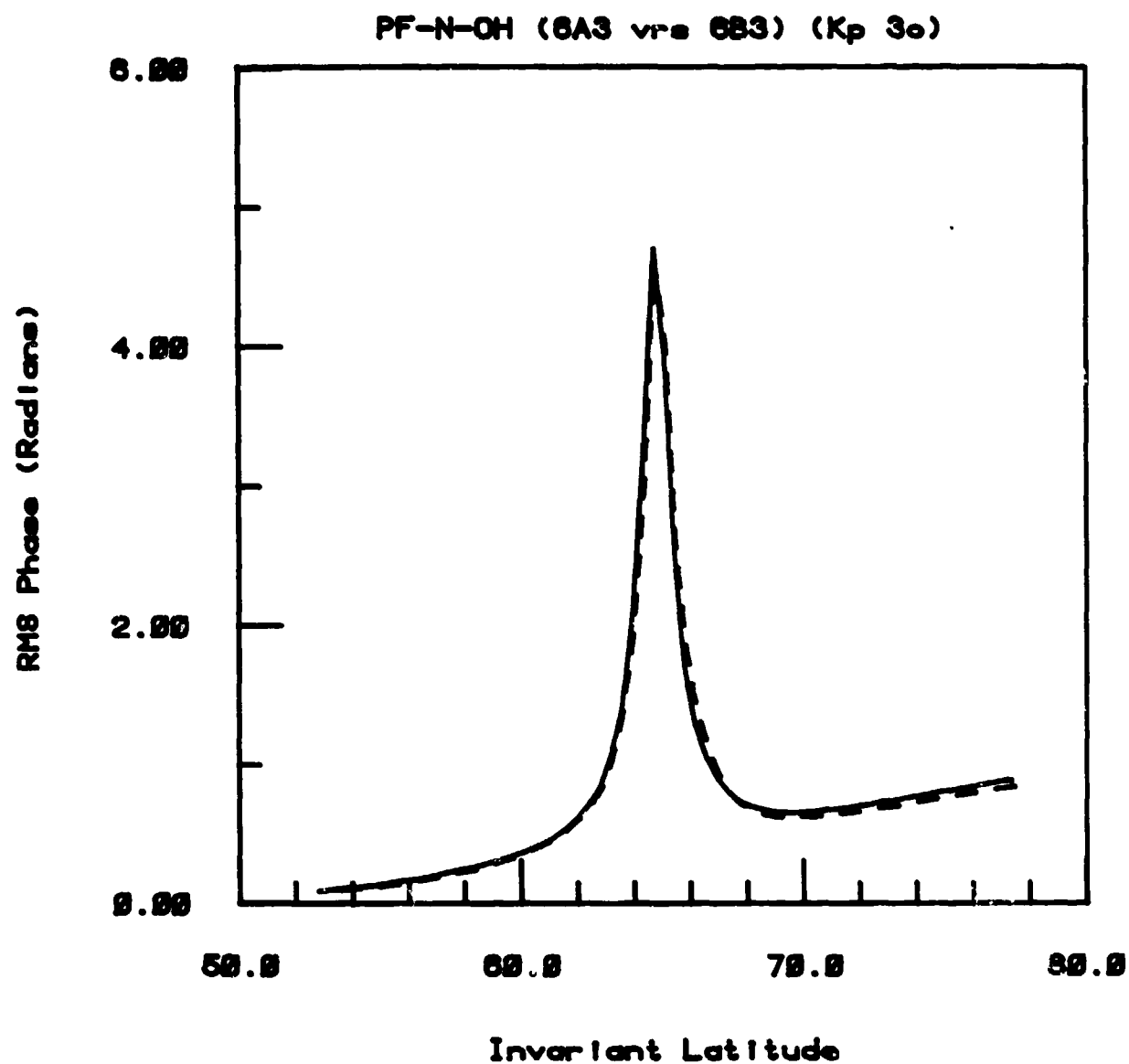
Figure 18. Drift velocity for K_p=6° at 1200 UT.

Figure 19. RMS phase for a simulated Poker Flat night-overhead Wideband pass. The solid curve is calculated using the old V_d model, the dashed curve using the new model.
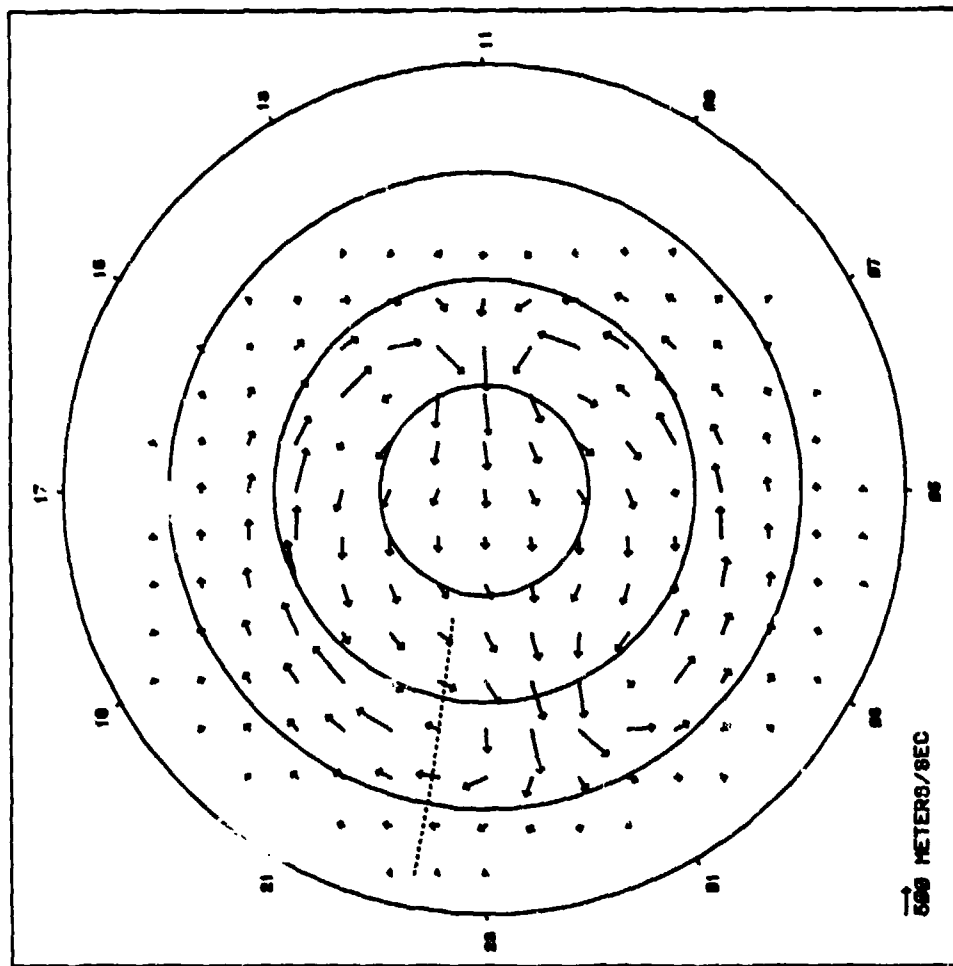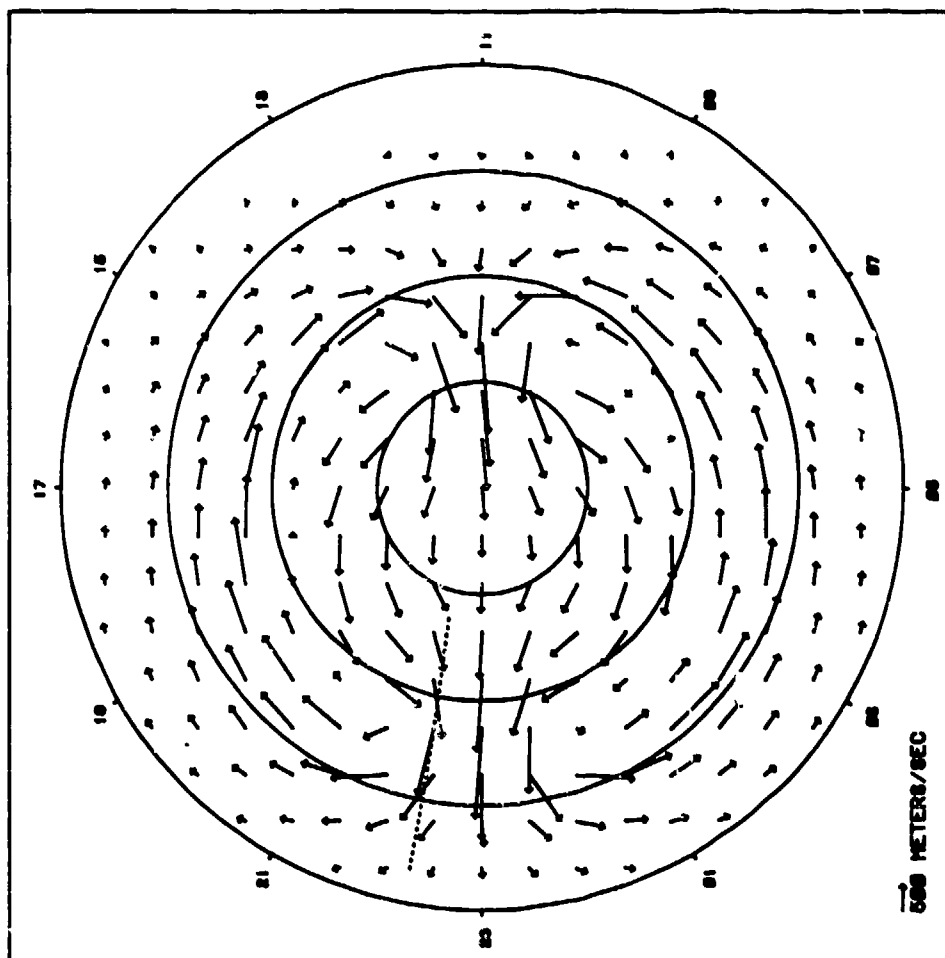
PF–N–OH (6A3 vrs 6B3) (Kp 8o)
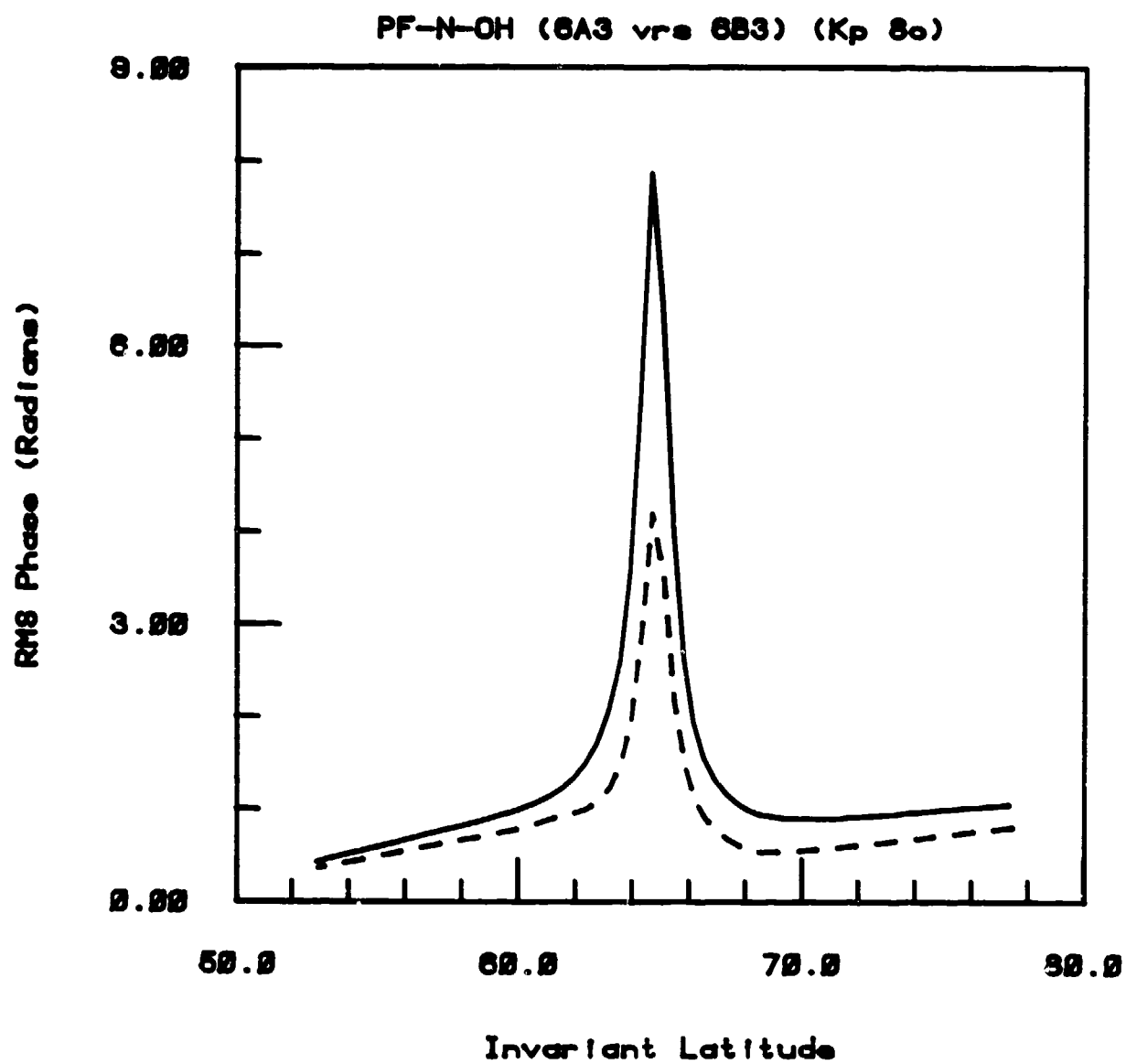
Figure 20.   Same as Figure 19 for $K_p = 8°$

Figure 21. Drift velocity pattern and ionospheric penetration point track for σ_ϕ calculation in Figure 19.

IRREGULARITY DRIFT VELOCITY
(HLS POTENTIAL MODEL)

ENVIRONMENT DATA

KP: 8.80
MKP: 5.31
OE: 8.8
EPS: 8.17E+85 (nT**2-KM/SEC)

MAX POTENTIAL: 82.8 kV

COORDINATE SYSTEM
THETA: INVARIANT LATITUDE
PHI: MAGNETIC LOCAL TIME
UT: F*55

Orbit track is Poker Flat N-OH

500 METERS/SEC

Figure 22.   Drift velocity pattern and ionospheric penetration point track for σ_ϕ calculation in Figure 20.
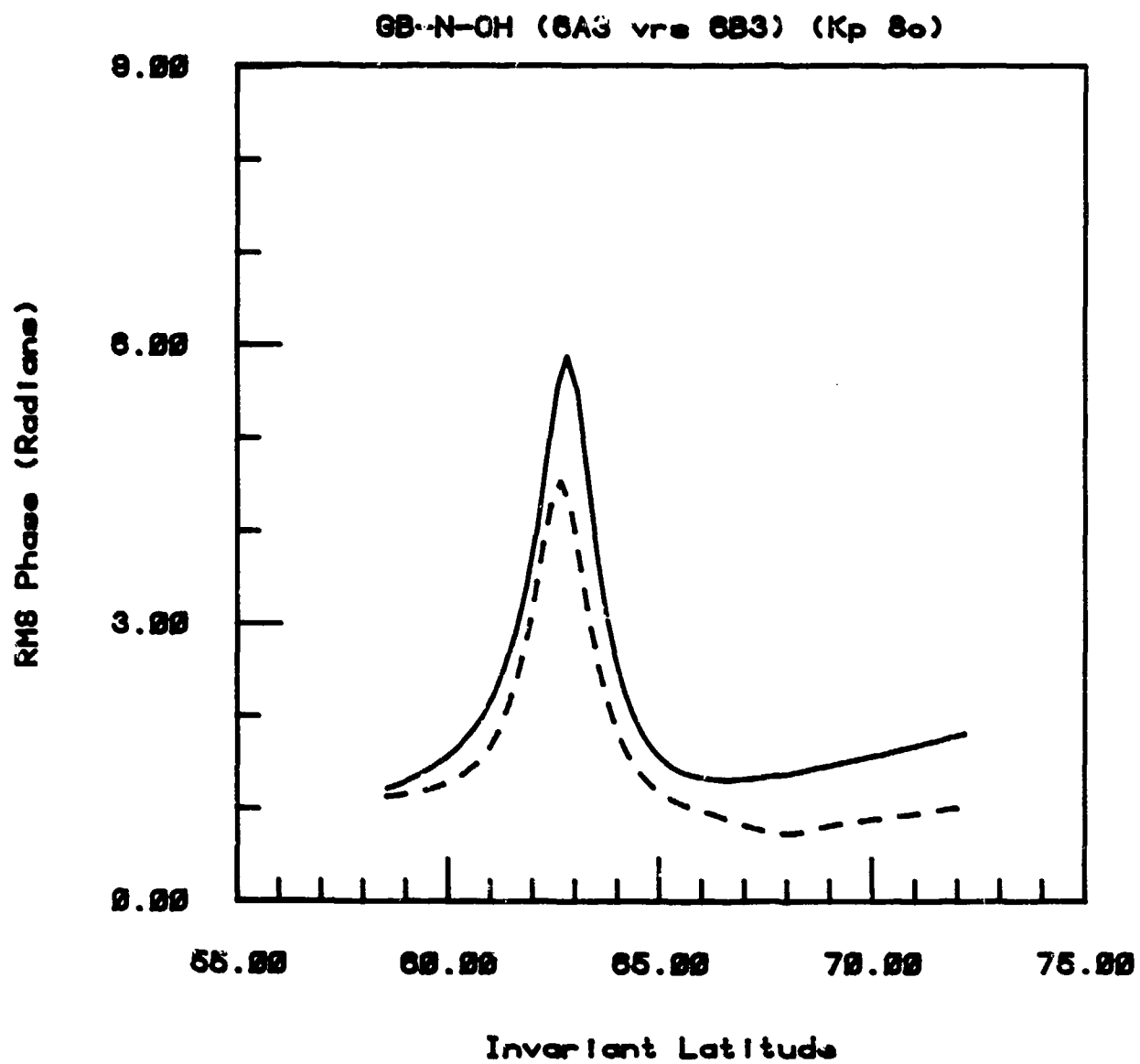
45

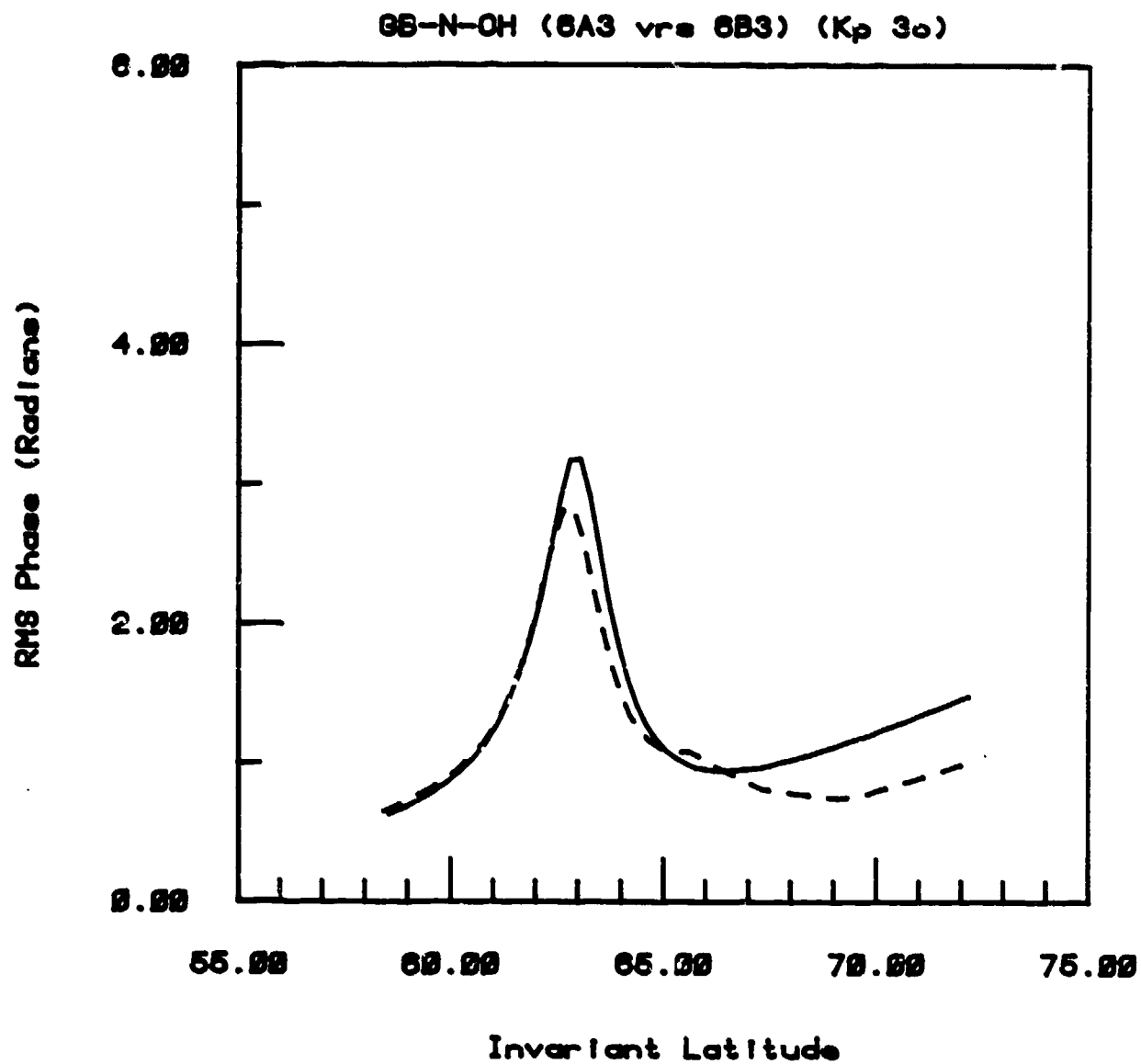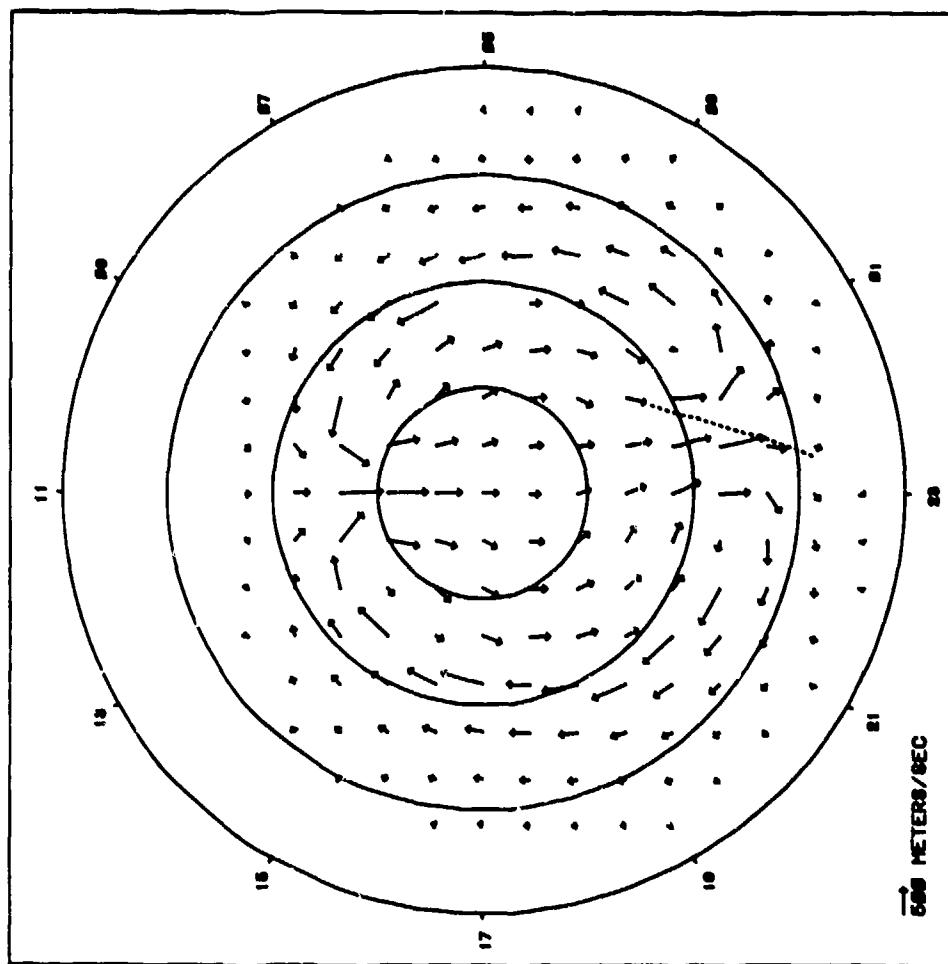Figure 23.   Same as Figure 19 for a simulated Goose Bay night-overhead pass.

46

Figure 24.   Same as Figure 23 for $K_p = 8o$.

47

Figure 25. Drift velocity pattern and ionospheric penetration point track for σ_ϕ calculation in Figure 23.

IRREGULARITY DRIFT VELOCITY
(HLS POTENTIAL MODEL)

ENVIRONMENT DATA
KP: 6.66
MKP: 5.31
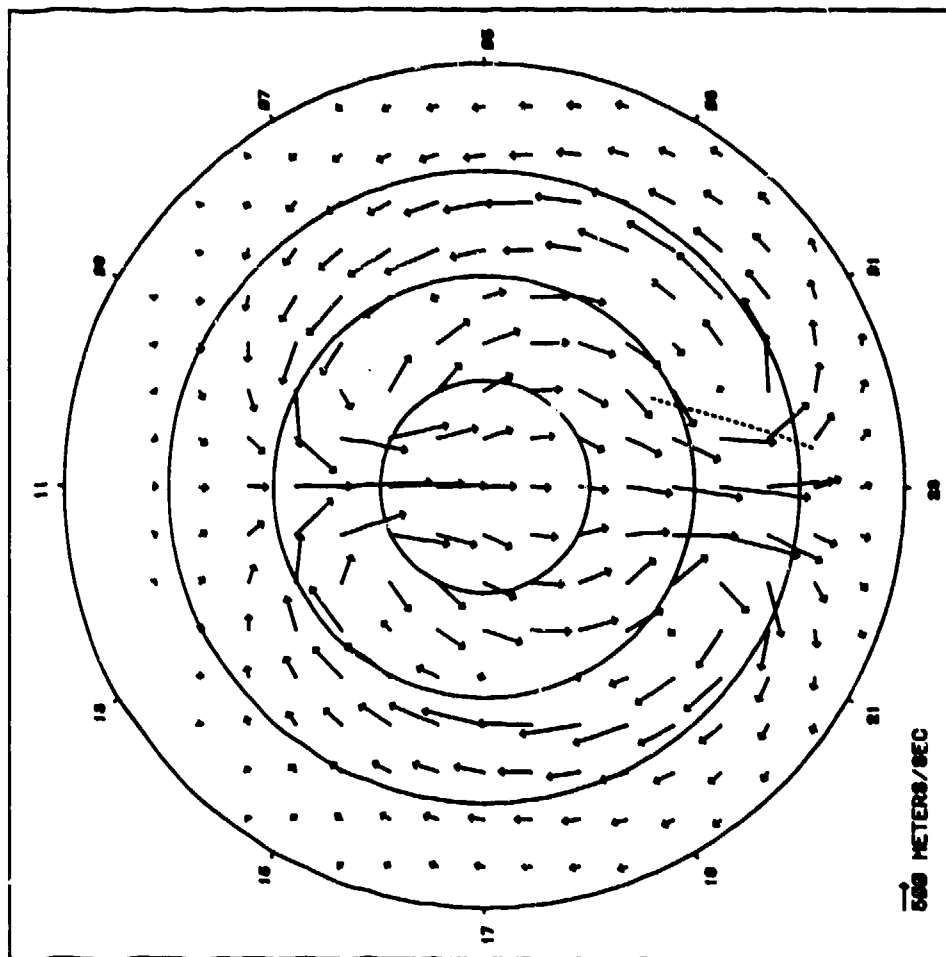QE: 8.8
EPS: 9.17E+06 (nT**2-KM/SEC)

MAX POTENTIAL: 62.9 kV

COORDINATE SYSTEM
THETA: INVARIANT LATITUDE
PHI: MAGNETIC LOCAL TIME
UT: 9492

Orbit track is for Goose Bay N-OH

500 METERS/SEC

Figure 26. Drift velocity pattern and ionospheric penetration point track for σ_ϕ calculation in Figure 24.
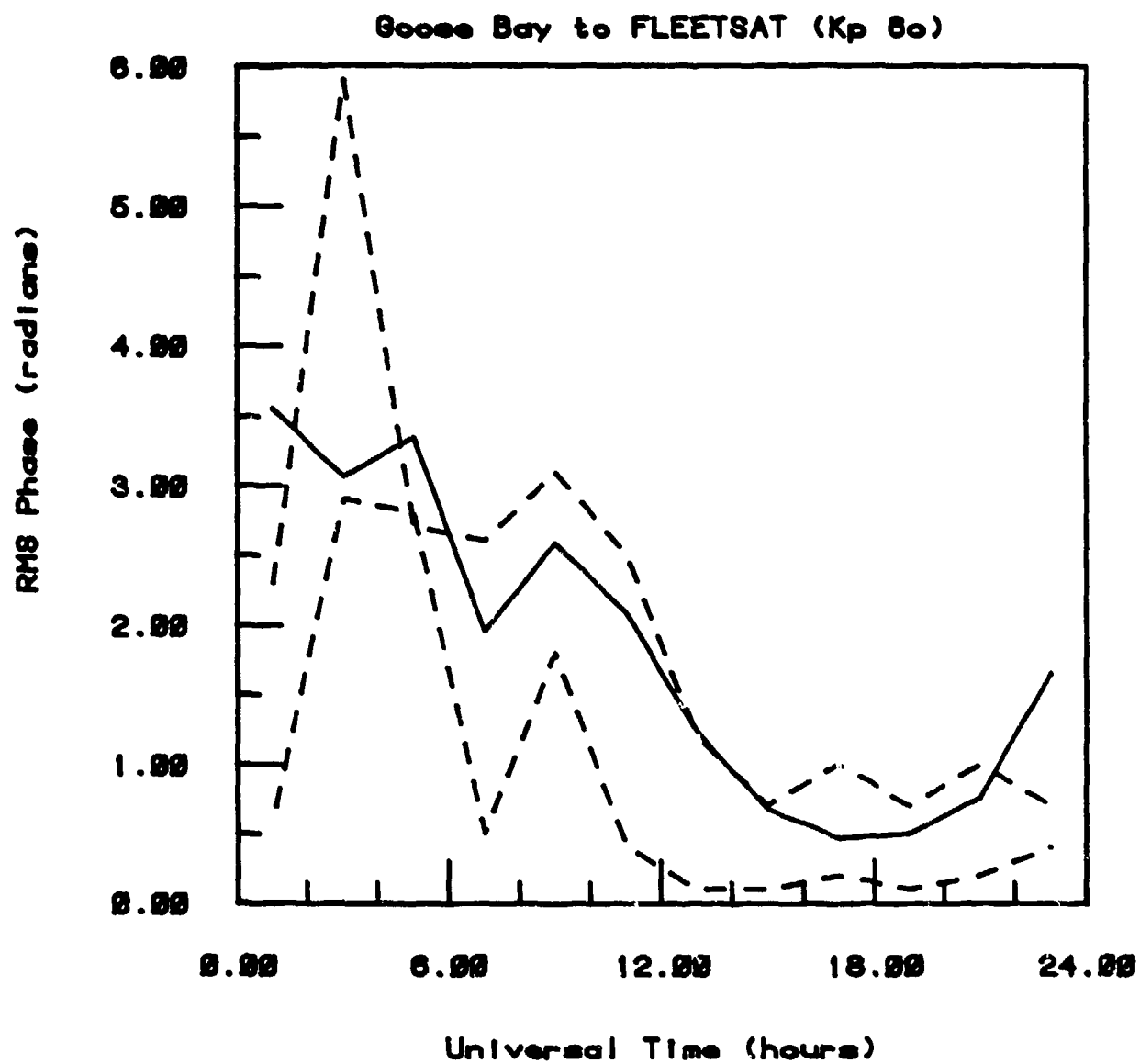
49

Figure 27. RMS phase index σ_ϕ for a Goose Bay - FLEETSAT geometry. Solid curve is calculated from WBMOD-6B3 using K_p=60, SSN=135. Upper dashed curve is from Basu *et al* (1982) Figure 3b, lower dashed curve is from their Figure 5b.

general agreement between the modeled and observed σ_ϕ, but some disagreement in detail. In particular, the peak that occurs at 0900 UT in all three curves is caused in the model by a peak in V_{eff}, while Basu *et al* speculate that it is due to a change in the irregularity strength, C_s, based on the occurrence of a similar peak in S_4 observations.

In summary, preliminary investigations of the effects of the new $\vec{V}_d$ model have produced several unexpected results. If correct, they should be observable in past, such as Wideband, and planned, such as HILAT, scintillation experiments. It must be emphasized that the most pronounced of these effects are strongly influenced by the potential-model parameters that control the location and width of the nightside exit region, the parameters that are possibly the most inadequately modeled of the entire set in the present model. The next step in this process should be a careful comparison of the effects predicted by the new model with the Wideband-Poker Flat data base to adjust the model parameters, followed by comparisons with other data sets, such as the Goose Bay - FLEETSAT observations, for verification.

SECTION 3
WBMOD REVISION 6B3

3-1 OVERVIEW

The current version of Program WBMOD, Revision number 6B3 dated 31 January 1983, includes several substantial changes to the initial version described by Fremouw and Lansinger (1981a). The major changes are as follows:

1. Code Structure (6).

   a. Geomagnetic field. The basic geomagnetic field model (Subroutine IGRF80) has been updated with the International Geomagnetic Reference Field (IGRF) 1980 coefficients as adopted by IAGA in 1981. Additional routines have been added to calculate invariant latitude (Kluge, 1970) and local magnetic (dipole) time (Section 2-1).

   b. Scan velocity. Two modifications were made in the calculation of the line-of-sight scan velocity (Subroutine VXYZ). The method used in the calculation was changed tc avoid an artificial contribution due to rapidly changing magnetic declination at high latitudes, and the error in calculating the scan velocity discussed in Section 2-2 was corrected.

   c. Orbit calculation. The circular-orbit calculation algorithms discussed in Section 2-3 were implemented.

   d. User interface. The WBMOD main routine and subroutine READIN were substantially modified to improve interaction with the user and to make changes of a software-engineering nature to improve program flow and code transportability to other computer systems.

2. Model form (B). The only change in model form from the original WBMOD is the calculation of irregularity drift velocity described in Section 2.5.

3. Model constants (3). Three model constants have been changed. The scintillation boundary parameter, λ_1, (Section 3-3) changed from 71.0° to 71.8° invariant latitude, and the height-integrated strength parameters for equatorial (C_e) and middle (C_m) latitudes were changed from 2.3×10^9 to 5.0×10^{12} and 3.0×10^9 to 1.9×10^{11}, respectively.

3-2 Structure of the Code.

Figure 28 is a flow diagram of Program WBMOD, Revision 6B3. Upon initiation of the program, the user is asked interactively for information regarding his computational scenario. The requested information includes parameters of the user's system, such as operating frequency and the longest time over which the system's mission requires phase stability. It also includes other aspects of the intended operation, such as transmitter and receiver location and time of day, plus characterization of the general state of solar/terrestrial disturbance by means of sunspot number and planetary magnetic activity index, K_p. Finally, the user specifies one of his input quantities as the independent variable (e.g., transmitter location or time of
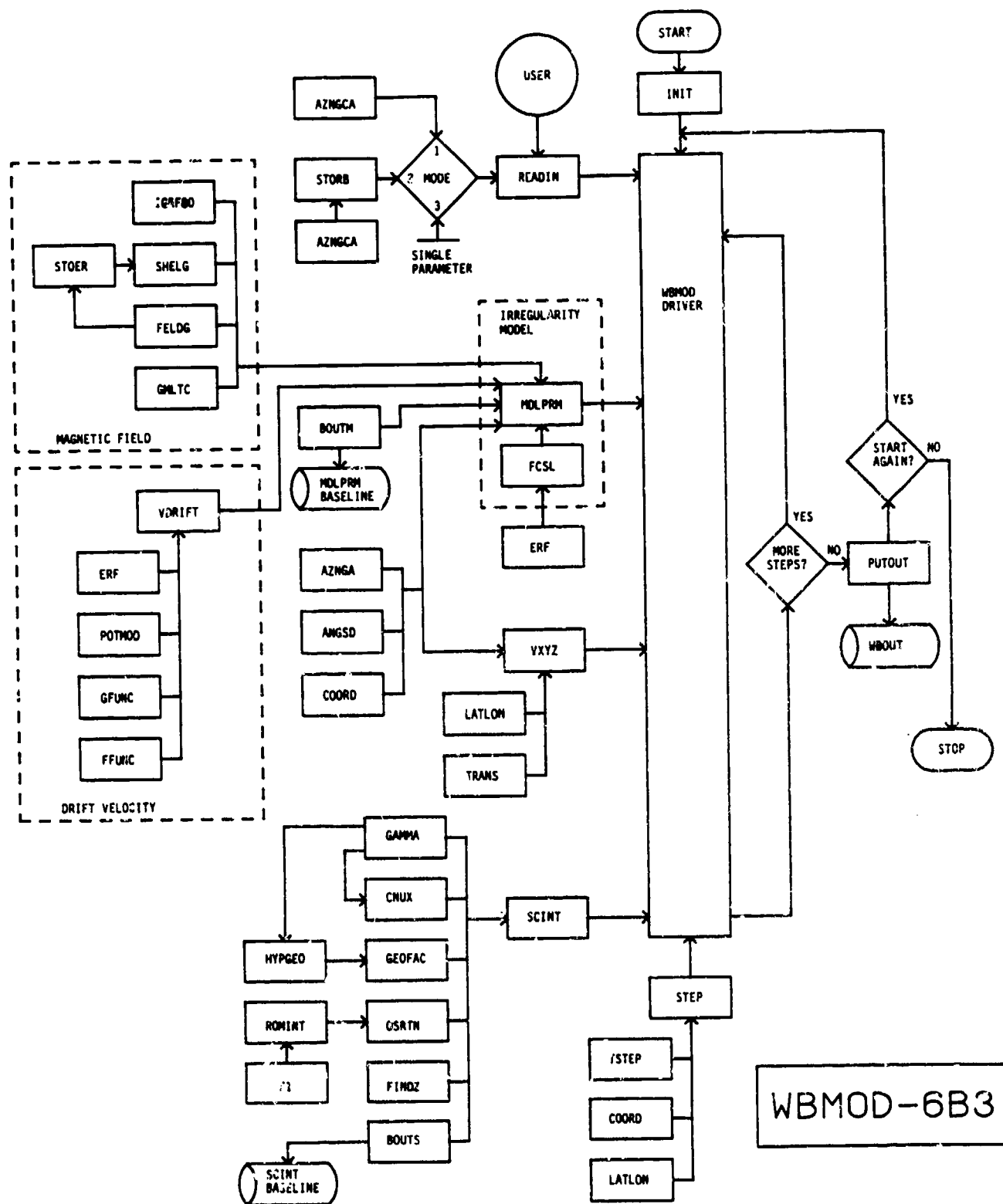
Figure 28. Flow chart for WBMOD Rev 6B3.

53

day). The output parameters (e.g., scintillation indices) then are calculated as functions of the selected independent variable.

The WBMOD Driver obtains information from the user through Subroutine READIN, by which a mode selection also is made and through which the geometry is initialized. The driver then increments the selected independent variable(s) (Subroutine STEP) and updates the geometry, calling upon the irregularity model and a propagation theory for scintillation calculations at each computational point. Among the parameters that the user may choose to vary are the receiver or transmitter latitude/longitude coordinates. This may be done either in an incremental but static manner (mode 1) or in an orbital mode (mode 2) in which the scanning motion of the line of sight is taken into account. The third mode consists of varying any single independent variable. (See Section 3-4 for a more detailed discussion of user inputs.)

The output parameters - value of the incremented variable(s), p (phase spectral index), T (phase spectral strength), σ_ϕ (RMS phase), and S_4 (intensity scintillation index) - are written to a temporary file after each calculation loop, and are written to a final summary file (WBOUT) by Subroutine PUTOUT after all increment steps are completed for printing or plotting by means of user-supplied software. When the chosen parameter range is satisfied, the user may start a new run in which any or all input parameters may be changed without a total reinitialization.

Two additional output files can be generated by subroutines BOUTM and BOUTS, if the user desires, by configuring subroutine INIT such that variables LUB1 and LUB2 are initialized with FORTRAN file numbers for each output file. Both files contain the penetration point latitude, longitude, dip latitude, and invariant latitude for each increment step. In addition, the file created by BOUTM contains the calculated model parameters a and b (along- and cross-field irregularity axial ratios), δ_s (sheet orientation angle), q (in-situ spectral index), $C_s L$ (height-integrated strength), and h_p (height of the phase screen), and the three components of in-situ drift velocity. The file created by BOUTS contains auxilliary and scintillation parameters p (phase spectral index), T (phase spectral strength), G (geometric factor), V_e (effective scan velocity), σ_ϕ, and S_4.

Table 3 contains a list of the subroutines and functions that make up WBMOD-6B3, with a brief synopsis of the function of each.

3-3 MODEL B3

Subroutine MDLPRM calculates, or calls routines to calculate, eight model parameters used to describe ionospheric irregularity structure for the calculation of the scintillation parameters, p, T, σ_ϕ, and S_4. These model parameters are the height, h_p, and the in-situ drift velocity, $\vec{V}_d$, of the irregularities; the outer scale, α; the height-integrated spectral strength, $C_s L$; the in-situ spectral index, q; and three "shape" parameters describing the three-dimensional configuration of the irregularities, a, b, and δ_s. The philosophy behind the definition and form of these model parameters, other than for $\vec{V}_d$, has not changed from the

Table 3
Subroutines and Functions in Program WBMOD

Name	Synopsis
WBMOD	Driver Routine
INIT	Initialization Routine (user specific)
READIN	Calls for inputs from user and certain subroutines
AZNGCA	Finds azimuth and great-circle angle between points 1 and 2 (Double Precision)
STGRB	Finds circular orbit between two points at a given altitude
MDLPRM	Establishes all parameters of the ionospheric-irregularity model except height-integrated strength and in-situ drift velocity
FCSL	Computes height-integrated strength of irregularities from empirical model
ERF	Computes error function (Double Precision)
IGRF80	Sets up arrays for calculation of the International Geomagnetic Reference Field (IGRF-1980).
SHELG	Calculates geomagnetic L parameter
STOER	Used in conjunction with SHELG
FELDG	Calculates magnetic-field components
GMLTC	Calculates difference between local mean solar time and local magnetic (dipole) time
VDRIFT	Calculates the in-situ drift velocity of the scintillation-producing irregularities
POTMOD	Calculates model parameters for the high-latitude convection potential model used by VDRIFT
GFUNC	Calculates the latitudinal variations of the high-latitude convection potential
FFUNC	Calculates the local magnetic time variations of the high-latitude convection potential
BOUTM	Builds a baseline output file of model parameters calculated in MDLPRM
ANGSD	Plane-geometry routine
COORD	Finds point 2 given point 1 and azimuth and great-circle angle between them (Double Precision)
VXYZ	Calculates line-of-sight scan velocity (Double Precision)

LATLON	Calculates latitude and longitude of an orbiting satellite (Double Precision)
TRANS	Calculates coordinate transformations for center-difference velocity calculation in VXYZ (Double Precision)
SCINT	Calculates scintillation parameters using phase-screen scattering theory
GAMMA	Gamma-function routine
HYPGEO	Calculates Gaussian hypergeometric function
CNUX	Calculates normalization factor used in computation of intensity scintillation index
GEOFAC	Calculates static and dynamic geometrical factors that influence scintillation strength
OSRTN	Sets up integral to calculate phase variance, for finite outer scale
ROMINT	Modified Romberg quadrature integration routine
F1	Computes change of variable for efficient integration by ROMINT
FINDZ	Calculates "reduced height" for one-way and two-way propagation
BOUTS	Builds a baseline output file of scintillation parameters calculated in SCINT
STEP	Controls the incrementing of whatever parameter is being varied during the model run
TSTEP	Increments time (includes date checks)
PUTOUT	Formats and controls output

original WBMOD. (See Section III of Fremouw and Lansinger 1981a.) The new $\vec{V}_d$ calculation is discussed in Section 2-5. Here we will present only the model forms for h_p, α, C_sL, q, a, b, and δ_s and the current values of all model constants.

1. Irregularity height.

$$h_p = h_e - h_t \left[1 + \text{erf} \left(\frac{\lambda_d - \lambda_h}{W_h} \right) \right] \text{km}$$

where

h_p = irregularity height at λ_d

h_e = irregularity height at dip equator

$h_t = (h_e - h_a)/2$

h_a = irregularity height at non-equatorial latitudes

λ_d = dip latitude

λ_h = dip latitude of h_e-to-h_a transition

W_h = half-width of transition.

2. Outer scale.

α = 1000.0 km (effectively ∞).

3. Height-integrated strength.

$\sqrt{C_sL}$ = E + M + H.

a. Equatorial term, (E).

$$E = C_e(1 + C_{er}R) \left\{ \exp \left[-\left(\frac{\lambda_d - \lambda_e}{W_e} \right)^2 \right] + \exp \left[-\left(\frac{\lambda_d + \lambda_e}{W_e} \right)^2 \right] \right\}$$

$$x \left\{ 1 - C_{es} \left[\cos \frac{2\pi}{182.5} (D + \Delta_d) + \frac{\lambda_q}{C_{eg}} \cos \frac{2\pi}{365} (D + \Delta_d) \right] \right\}$$

$$x \left\{ \exp \ - \left(\frac{t + (24 - t_e)}{T_-} \right)^2 + \exp \left[-\left(\frac{t - t_e}{T_+} \right)^2 \right] \right\}$$

where

C_e = equatorial C_sL scale parameter

C_{er} = Proportionality constant for sunspot number

R = smoothed sunspot number

λ_d = dip latitude

λ_e = dip latitude boundary of equatorial "anomaly" in ionospheric total electron content and C_sL.

57

W_e = Half-width of equatorial-to-mid-latitude transition

C_{es} = proportionally constant for season

D = day of year (1-365)

Δ_d = phase delay (days) of seasonal variations

λ_g = geographic latitude

C_{eg} = proportionally constant for geographic latitude

t = local geographic-meridian time (hours)

t_e = time of maximum equatorial scintillation

T_+ = post-maximum temporal half-width

T_- = T_+ if t < t_e

= pre-maximum temporal half-width if t > t_e.

b.   Mid-latitude term, (M).

$$M = C_0 \left(1 + C_{ot}\cos \frac{2\pi}{24} t \right) \exp\left[-\left(\frac{\lambda_I - \lambda_0}{W_0}\right)^2 \right]$$

where

C_j = mid-latitude C_sL scale parameter

C_{ot} = variation with local time

t = local time

λ_I = invariant latitude

λ_0: statistical center of the mid-latitude region

W_m: half-width of the mid-latitude region

c.   High-latitude term, (H).

$$H = C_h(1 + C_{hr}R)\left[1 + erf\left(\frac{\lambda_I - \lambda_b}{W_h}\right) \right]$$

where $\lambda_b = \lambda_1 - C_k K_p - C_{bt} \cos \frac{2\pi}{24} (t_0 - t_{bo})$

$W_h = C_{hb} b$

C_h = high-latitude C_sL scale parameter

C_{hr} = proportionally constant for sunspot number

R = smoothed sunspot number

λ_I = invariant latitude

λ_b = sub-auroral scintillation boundary

W_h = width of transition at scintillation boundary

λ_1 = nominal invariant latitude of quiet-time boundary

C_k = rate of migration of $_b$ with K_p (deg per K_p unit)

58

K_p = three-hour magnetic index (0.0 to 9.0)

C_{bt} = variation of λ_b with local magnetic time

t_m = local magnetic time (LMT)

t_{mt} = phase delay (hours) of LMT variation

C_{Hb} = boundary-width scale parameter.

4. *In-situ* spectral index.

   $q = 1.5$.

5. Field-aligned axial ratio.

$$a = a_0 - a_0 \left[1 + erf\left(\frac{\lambda_d - \lambda_h}{W_h}\right)\right]$$

where a_e = equatorial value of a

$a_t = (a_e - a_a)/2$

a_a = non-equatorial value of a

λ_d = dip latitude

λ_h = statistical dip latitude of a_E-to-a_A transition

W_h: Half-width of transition.

6. Cross-field axial ratio.

$$b = 1 + b_h \left[1 + \cos \frac{2\pi}{24} (t_m - t_{mt})\right]\left[1 + erf\left(\frac{\lambda_I - \lambda_b}{W_h}\right)\right]$$

where b_h = auroral b scale factor.

(See high-latitude C_sL term for other variables.)

7. Orientation angle of sheetlike irregularities relative to L shell.

$\delta_s = 0.0$.

The values for all model constants in Rev 6B3 of Program WBMOD are listed in Table 4. Included in this table are the constants used in the drift-velocity calculation.

3-4 USE OF THE CODE

Program WBMOD is structured for interactive application from a user terminal. A sample interaction for Rev 6B3 is provided in Table 5, in which system queries are indicated in lower case and user responses in caps. As indicated in the table, a computation session begins with a request by the code for a label by which the run output is to be identified. The label may consist of any alphanumeric string of up to 40 characters. The code then permits the user to make several choices.

First, the user selects either one-way (communication system) or two-way (radar) propagation and then the reciprocal of the low-frequency cutoff of the band of phase-fluctuation

TABLE 4

WBMOD Model B3 Constants

Irregularity Height

h_0 = 500 km λ_h = 20.0° dip

h_0 = 350 km W_h = 3.0° dip

Height-Integrated Strength

Equatorial:

C_e = 5.0x10^{12} C_{er} = 0.04 C_{es} = 0.40

λ_e = 10.0° dip W_e = 10.0° dip C_{eg} = 15.0°

Δ_D = 10.0 days t_e = 22.5 hrs T_+ = 6.0 hrs for t t_e

   T_- = T_+ for t > t_e

   = 3.0 hrs for t t_e

Mid latitude:

C_m = 1.9x10^{11} C_{mt} = 0.33 λ_m = 32.5° invariant

W_m = 15.0° invariant

High latitude:

C_h = 4.3x10^{11} C_{hr} = 0.0496 C_K = 1.5

C_{bt} = 5.5 C_{hb} = 0.15 λ_1 = 71.8° invariant

t_{mt} = 2.0 hrs

Axial Ratios

a_e = 30.0 a_a = 8.0 b_h = 0.75

Drift Velocity

Θ_0 = 5.0° invariant ϕ_0 = 0.0 hrs θ_c = 10.0°

ϕ_d = 180.0° ϕ_d^+ = 30.0° ϕ_d^- = 30.0°

ϕ_{no} = 390.0° ϕ_n^+ = 30.0° ϕ_n^+ = 30.0°

r_1 = - 4.0 r_2 = 2.0

60

WBMOD REV 6B3 REQUESTS A LABEL FOR THIS RUN.
POKER FLAT (N-OH)

DO YOU WANT ONE-WAY (1) OR TWO-WAY (2) PROPAGATION?
1

ENTER DURATION (SECONDS) OVER WHICH SYSTEM REQUIRES PHASE STABILITY
(0.0 FOR SYSTEMS NOT SENSITIVE TO PHASE SCINTILLATION).
10.0

ENTER IONOSPHERIC OUTER SCALE (KM) OR TYPE "MODEL" FOR EFFECTIVELY INFINITE
DEFAULT VALUE.
MODEL

ENTER IRREGULARITY DRIFT VELOCITY (M/S) FOR GEOMAGNETIC NORTH, EAST, DOWN
OR TYPE "MODEL" FOR KP-DEPENDENT DEFAULT VALUE.
MODEL

PROVIDE INITIAL VALUES FOR FOLLOWING
(IN MHZ, DECIMAL NUMBER, DECIMAL HOURS, DECIMAL DEGREES, OR KM, AS APPROPRIATE).

    OPERATING FREQUENCY (FREQ):
137.68

    PLANETARY GEOMAGNETIC ACTIVITY INDEX (KP):
3.0

    SMOOTHED ZURICH SUNSPOT NUMBER (SSN):
75.0

    DAY OF THE YEAR (DAY):
150.0

    MERIDIAN TIME AT RECEIVER OR RADAR TARGET (TIME):
0.65

    LATITUDE OF RECEIVER OR TARGET (RLAT):
65.1

    LONGITUDE OF RECEIVER OR TARGET (RLON):
-147.5

    ALTITUDE OF RECEIVER OR TARGET (RALT):
0.2

    LATITUDE OF TRANSMITTER OR RADAR (TLAT):
80.2

    LONGITUDE OF TRANSMITTER OR RADAR (TLON):
-85.7

    ALTITUDE OF TRANSMITTER OR RADAR (TALT):
1026.0

SELECT CHANGING PARAMETER
(ONE OF THE NAMES IN PARENS ABOVE OR TYPE "RCRD" OR "TCRD"
TO STEP RECEIVER OR TRANSMITTER ALONG A GREAT-CIRCLE
OR "ORBT" TO CAUSE HIGHER TERMINAL TO PERFORM ORBITAL SCAN
AT CONSTANT ALTITUDE).
ORBT

PROVIDE FINAL VALUE FOR THE FOLLOWING:
    LATITUDE OF TRANSMITTER OR RADAR (TLAT):
42.8

    LONGITUDE OF TRANSMITTER OR RADAR (TLON):
-161.2

SPECIFY NUMBER OF CALCULATION POINTS   (150 MAX):
50

    SUMMARY OF VALUES
    RUN CONDITIONS
LABEL .   POKER FLAT (N-OH)
1-2WAY   PH DUR   OUTER SCALE   VDX   VDY   VDZ
    1   10.0   MODEL   MODEL DRIFT VELOCITY

    INITIAL VALUES
FREQ: SSN: DAY: TIME: KP:
 137.68   75.0   150.   0.650   3.0
RLAT: RLON: RALT: TLAT: TLON: TALT:
 65.100   -147.500   0.200   80.200   -85.700   1026.000

    CHANGING PARAMETER :   ORBT
INITIAL   LAT :   80.200   LONG :   -85.700
FINAL   LAT :   42.800   LONG : -161.200
OF POINTS :   50.
ARE VALUES CORRECT?   YES = 1   NO = 2
1

DO YOU WISH TO START AGAIN?
    1: COMPLETE STARTOVER
    2: NO
    3: ONLY ALTERING SOME VALUES
2

Table 5.   Sample WBMOD-6B3 User Interaction

frequencies to which his system is susceptible. Thereafter, he either provides values for the geomagnetic east-west outer scale of the *in-situ* electron-density spectrum and for the drift velocity of ionospheric irregularities or elects to let the code employ default values for them. For high latitudes, the default values for drift velocity are obtained from the convection model described in Sections 2-5.2 through 2-5.4.

Next, the code requests initial values for the potentially variable parameters that describe the operating scenario. Once the initial values have been set by the user, the code inquires as to which computational mode is desired. The user may select any of the 11 parameters just initialized to be the independent variable against which output parameters are to be tabulated. Alternatively, either the receiver (radar target) or transmitter (radar) may be stepped in latitude (north positive) and longitude (east positive) along a great circle by typing in RCRD or TCRD, respectively, instead of a single variable name.

In eleven of the foregoing modes, scintillation parameters are calculated for each incremented value of the independent variable(s) without introducing a line-of-sight scan. (That is, scintillation is taken to arise only from irregularity drift.) Finally, the ORBT mode may be selected, in which the receiver or transmitter (whichever is higher) moves along a constant-altitude circular orbit, and scintillation results from a combination of line-of-sight scan and irregularity drift. (In most low-orbiting applications, the former velocity dominates.) Whatever mode is chosen, the code now asks for the final value(s) of the changing parameter(s) and for the number of increments desired between the initial and final values.

A sample output, (WBOUT), corresponding to the interaction contained in Table 5, is illustrated in Table 6. Following a general heading, the title specified by the user is printed. Thereafter, his input parameters are identified, followed by the calculation outputs. The first output is a single printing of the power-law spectral index, p, of phase scintillation. Finally, columns containing the following information are provided: calculation point number; changing parameter(s); the spectral strength parameter, T, for phase scintillation; the phase scintillation index, σ_ϕ; and the intensity scintillation index, S_4.

Tables 7 and 8 illustrate samples of the model and scintillation calculation baseline output files. Both outputs include the penetration point geographic latitude (PLAT) and longitude (PLON), dip latitude (DIPLAT), and invariant latitude (INVLAT). The baseline model output also includes the calculated values for a, b, δ_s, q, C_sL, V_D, and h_p. The baseline auxiliary and scintillation output includes the calculated values for p, T, G, V_e, σ_ϕ, and S_4.

62

F-LAYER-PRODUCED RADIOWAVE SCINTILLATION

CALCULATED FROM A MODEL DEVELOPED BY PHYSICAL DYNAMICS, INC.
BELLEVUE, WA 98009

WBMOD - REV   6B3

THIS RUN IS POWER FLAT (N-OH)
ONE-WAY PROPAGATION
REQUIRED PHASE-STABILITY DURATION =   10.0 SEC
IONOSPHERIC OUTER SCALE: EFFECTIVELY INFINITE
IRREGULARITY DRIFT VELOCITY   DEFAULT MODEL

FREQ = 137.48 MHZ   AP INDEX = 3.0   SSN = 75.

DAY OF YEAR = 150.   TIME =   0.69 HOURS LMT AT RECEIVER

FOR FIRST DATA POINT
RECEIVER COORDINATES   TRANSMITTER COORDINATES
   LAT =   65.10 DEG   LAT =   80.20 DEG
   LON = -147.50 DEG   LON = -85.70 DEG
   ALT =   0.200 KM   ALT = 1036.000 KM

FOR THIS RUN, THE CHANGING PARAMETERS WERE
 TRANSMITTER LATITUDE AND LONGITUDE SCANNING ALONG ORBIT.

POWER-LAW SPECTRAL INDEX OF PHASE SCINTILLATION: P = 2.50

	TLAT	TLONG	T	RMS PHASE(RAD)	S4
1	80.200	-85.700	0.1614E-01	0.825	0.662
2	80.022	-91.010	0.1520E-01	0.801	0.645
3	79.746	-96.078	0.1432E-01	0.777	0.628
4	79.436	-100.911	0.1349E-01	0.754	0.609
5	79.040	-105.412	0.1273E-01	0.733	0.590
6	78.585	-109.586	0.1204E-01	0.713	0.570
7	78.077	-113.433	0.1142E-01	0.694	0.550
8	77.523	-116.961	0.1087E-01	0.677	0.529
9	76.929	-120.190	0.1039E-01	0.662	0.508
10	76.299	-123.141	0.9987E-02	0.649	0.487
11	75.639	-125.837	0.9634E-02	0.638	0.466
12	74.953	-128.303	0.9403E-02	0.630	0.444
13	74.243	-130.561	0.9236E-02	0.624	0.426
14	73.514	-132.633	0.9173E-02	0.622	0.408
15	72.767	-134.537	0.9235E-02	0.624	0.391
16	72.005	-136.291	0.9392E-02	0.629	0.376
17	71.229	-137.912	0.9818E-02	0.643	0.364
18	70.442	-139.413	0.1070E-01	0.672	0.355
19	69.644	-140.806	0.1216E-01	0.716	0.350
20	68.836	-142.103	0.1432E-01	0.782	0.351
21	68.021	-143.313	0.1873E-01	0.889	0.360
22	67.198	-144.445	0.2671E-01	1.061	0.381
23	66.368	-145.506	0.4204E-01	1.331	0.422
24	65.533	-146.504	0.7544E-01	1.784	0.497
25	64.692	-147.443	0.1601E 00	2.598	0.634
26	63.846	-148.330	0.3816E 00	4.011	0.826
27	62.997	-149.169	0.5030E 00	4.614	0.890
28	62.143	-149.964	0.2209E 00	3.058	0.747
29	61.285	-150.720	0.8897E-01	1.937	0.584
30	60.424	-151.438	0.4413E-01	1.364	0.483
31	59.560	-152.123	0.2509E-01	1.045	0.425
32	58.694	-152.777	0.1699E-01	0.846	0.389
33	57.825	-153.403	0.1202E-01	0.712	0.366
34	56.953	-154.002	0.8951E-02	0.614	0.350
35	56.080	-154.577	0.6889E-02	0.539	0.338
36	55.204	-155.129	0.5428E-02	0.478	0.329
37	54.327	-155.660	0.4335E-02	0.428	0.321
38	53.447	-156.172	0.3494E-02	0.384	0.313
39	52.567	-156.666	0.2824E-02	0.345	0.305
40	51.685	-157.143	0.2286E-02	0.310	0.296
41	50.801	-157.605	0.1847E-02	0.279	0.286
42	49.916	-158.052	0.1486E-02	0.250	0.274
43	49.030	-158.485	0.1180E-02	0.224	0.261
44	48.143	-158.905	0.9427E-03	0.199	0.246
45	47.255	-159.314	0.7426E-03	0.177	0.230
46	46.366	-159.711	0.5796E-03	0.156	0.213
47	45.475	-160.097	0.4487E-03	0.138	0.195
48	44.585	-160.474	0.3436E-03	0.120	0.176
49	43.693	-160.841	0.2614E-03	0.105	0.157
50	42.800	-161.200	0.1984E-03	0.091	0.139

Table 6.   Sample WBMOD-6B3 Output

63

BASELINE OUTPUT (MODEL)

PLAT	PLON	DIPLAT	INLAT	A	B	DELTA	Q	CBL	CSL	VDX	VDY	VDZ	HP

Table 7.   Sample Model Baseline Output

PLAT	PLON	DIPLAT	INVLAT	Q	VEFF	P	T	PRMS	S4

Table 8. Sample Auxilliary and Scintillation Baseline Output

SECTION 4
RESEARCH TOPICS

4-1 INTRODUCTION

The scattering theory (Rino, 1979) employed in WBMOD is formulated for a simply aniso-
tropic three-dimensional power-law spectral characterization of the scattering irregularities.
By "simply anisotropic" is meant that the anisotropy is restricted to the spectral strength
(and, by inference and normalization, to the inner and outer scales), with the power-law
spectral index taken as isotropic. The theoretical formulation also is in the infinite outer-
scale limit.

For modeling on the basis of such a characterization, one needs six spectral parameters
and two auxilliary quantities. The spectral parameters are the height-integrated power spec-
tral density, C_sL, at a reference wavenumber; the *in-situ* (one-dimensional) spectral index, q;
two anisotropy-defining axial ratios, a and b; and two orientation angles. The first angle is
taken to be the local magnetic dip, d, on the assumption that the irregularities are elongated
along the field by ambipolar diffusion. The second, δ_s, is measured from the magnetic east and
is invoked to describe the orientation of (sheetlike) irregularities elongated along a second
axis.

The parameters, a and b, are respectively the ratios of irregularity scale-size along the
magnetic field and along a second elongation axis to that in the remaining orthogonal direc-
tion. The two auxilliary parameters needed are an equivalent phase-screen height (closely
corresponding to the centroid height of the irregular layer) and the irregularity drift veloci-
ty. The latter is needed for accurately modeling scintillation on geostationary and slowly
moving satellite links. It was addressed in Section 2-5.

There are several signal parameters observable in scintillation measurements, but they are
by no means related one-to-one to the foregoing eight irregularity parameters. Nonetheless,
relationships do exist, and a relative efficiency can be achieved by applying various observ-
ables in a particular order to evaluation of the physical parameters. For instance, the axial
ratios, a and b, and the orientation angle, δ_s, are most directly deduced from interferometer
measurements. Approaches that do not use interferometer measurements (Fremouw and Lansinger,
1981a and 1981b) suffer from a need to combine multiple observing geometries for a single
result and from uncertainty over variations in irregularity strength.

4-2 THE PHASE-GRADIENT RATIO

General analysis of interferometer measurements (Rino and Livingston, 1982) is quite time-
consuming. For application to modeling, which involves large volumes of data, one would like a
more time-efficient, even if less general, technique. In our research related to WBMOD, we
explored one such possibility, the theoretical basis for which is as follows.

66

The phase structure function, $D(\vec{\beta})$, for an interferometer baseline $\vec{\beta}$ is defined as

$$D(\vec{\beta}) = \left\langle \left[\phi(\vec{\rho} + \vec{\beta}) - \phi(\vec{\beta}) \right]^2 \right\rangle \tag{36}$$

and is related to the normalized phase autocorrelation function, $R(\vec{\beta})$, as follows (Tatarski, 1971):

$$D(\vec{\beta}) = 2 \sigma_\phi^2 [1 - R(\vec{\beta})] \tag{37}$$

where σ_ϕ^2 is the phase variance. For a power-law phase spectrum with spectral index, p, and outer scale, α, observed in a processing window with a low-frequency cutoff, f_c, we have (Rino and Fremouw, 1977; Rino, 1979)

$$R(\beta) = \int_{\kappa_c}^{\infty} \frac{J_0(\kappa \beta_e) d\kappa}{(\kappa_0^2 + \kappa^2)^{(p+1)/2}} \bigg/\!\!\int_{\kappa_c}^{\infty} \frac{d}{(\kappa_0^2 + \kappa^2)^{(p+1)/2}} \tag{38}$$

where $\kappa_0 = \alpha^{-1}$

and $\kappa_c = \dfrac{2\pi f_c}{V_e}$

and where V_e is the effective velocity of the phase pattern across the observing plane, given by Equation (9) in Section 2-2.

The anisotropy information we seek is carried in the argument of the Bessel function, J_0, in Equation (38), specifically in the "effective baseline" given by

$$\beta_e = S(C\beta_{sx}^2 - B\beta_{sx}\beta_{sy} + A\beta_{sy}^2)^{\frac{1}{2}} \bigg/ (AC - \frac{B^2}{4})^{\frac{1}{2}} \tag{39}$$

where $\beta_{sx} = \beta_x - \beta_z \tan\theta \cos\phi$ \hfill (40)

and $\beta_{sy} = \beta_y - \beta_z \tan\theta \sin\phi$ \hfill (41)

where S is a geometrical factor accounting for wavefront sphericity; A, B, and C are given in Rino and Fremouw (1977); θ and ϕ respectively are in the incidence angle and magnetic heading of the propagation vector; and β_x, β_y, and β_z, are the components of the interferometer's physical baseline, $\vec{\beta}$. Suppose now that we have two interferometers oriented perpendicular and parallel to the intersection of known sheetlike irregularities with a plane parallel to the observing plane. Calling their effective baselines $\beta_\perp$ and $\beta_\parallel$, respectively, we can define the "phase-gradient ratio," r, such that

67

$$r^2 = \frac{D(\beta_\perp)}{D(\beta_{\parallel})} \quad . \tag{42}$$

Our desires are, first, to compute $\beta_\perp$ and $\beta_{\parallel}$ for different irregularity axial ratios, a and b, and observing geometries, which dictate A, B, and C; second, to evaluate Equation (39); and, third, to identify best fits of the ratio, r, to pass-long time series of the observed phase-gradient ratio (or to multipass averages thereof). We would like the p-dependence of r to be sufficiently weak or well-behaved that a and b could be determined from the behavior of r. This would give us a means for evaluating the axial ratios that is independent of the highly variable irregularity strength, but much faster than the general correlation analysis of Livingston et al (1982). We must first investigate the p-dependence of r and find an efficient means for evaluating Equation (38).

Evaluating the integrals, whether analytically or numerically, is facilitated by making the infinite-outer-scale approximation. To assess the effect of this assumption and to serve as a simple illustrative example of the behavior of Equation (39), we first evaluated Equations (37) through (42) for the following Gaussian autocorrelation function:

$$R(\vec{\beta}) = \exp(-\beta_e^2/L_0^2) \tag{43}$$

where β_e is given by Equations (39), (40), and (41). In the infinite-outer-scale approximation, we have obviously

$$r \approx \beta_\perp/\beta_{\parallel} \quad . \tag{44}$$

For representative model parameters and actual observing geometries and baselines employed for Wideband at Poker Flat, we found the general Gaussian case to yield results identical to those obtained from Equation (44).

We expect the infinite-outer-scale approximation to hold, regardless of the autocorrelation-function form, so long as L_0 is much larger than the physical length of the interferometer baseline, and we have employed it in the power-law case. Accordingly,

$$R(\vec{\beta}) = \int_{\kappa_c}^\infty \kappa^{-p} J_0(\kappa\beta_e)d\kappa \bigg/ \int^\infty \kappa^{-p} d\kappa \tag{45}$$

so we have, approximately,

$$r^2 = \left(\frac{\beta_\perp}{\beta_{\parallel}}\right)^{(p-1)} \frac{I(\beta_\perp, p; \kappa_c)}{I(\beta_{\parallel}, p; \kappa_c)} \tag{46}$$

where $\quad I = \int_{x_c}^\infty x^{-p} \left[1 - J_0(x)\right] dx \tag{47}$

and $x_c = \beta_e \varsigma_c$. (48)

For computational efficiency, we split Integral (47) into two ranges, employing respectively small- and large-argument approximations to the Bessel function. Specifically, we used

$$I = I_1 + I_2$$ (49)

where

$$I_1 = \int_{x_c}^{x_b} x^{-p} \left[1 - J_0(x) \right] dx$$ (50)

$$\approx \sum_{n=1}^{N} (-1)^{(n+1)} \frac{x_b^{(2n+1-p)} - x_c^{(2n+1-p)}}{4^n (n!)^2 (2n+1-p)}$$ (51)

and

$$I_2 \approx \sqrt{\frac{2}{\pi}} \int x^{-(p+\frac{1}{2})} \cos(x - \frac{\pi}{4}) dx$$ (52)

$$\approx \pi^{-\frac{1}{2}} \left\{ x_b^{-(p+\frac{1}{2})} \cos x_b + \Gamma_{1x} \cos \frac{\pi(p-\frac{1}{2})}{2} - \Gamma_{1y} \sin \frac{\pi(p-\frac{1}{2})}{2} \right.$$

$$\left. -(p+\frac{1}{2}) \left[\Gamma_{2x} \cos \frac{\pi(p+\frac{1}{2})}{2} - \Gamma_{2y} \sin \frac{\pi(p+\frac{1}{2})}{2} \right] \right\}$$ (53)

where Γ_{1x} and Γ_{1y} are the real and imaginary parts of $\Gamma[-(p-\frac{1}{2}), ix_b]$, and Γ_{2x} and Γ_{2y} are the real and imaginary parts of $\Gamma[-(p+\frac{1}{2}), ix_b]$. We found $x_b = 3.8$ and $N = 5$ to give quite satisfactory accuracy through the whole range of integration.

We coded the results of the foregoing analysis in the model-development version of WBMOD. Figures 29 and 30 contain calculated results therefrom to illustrate pertinent behaviors of the phase-gradient ratio, r. The left-hand side of Figure 29 shows that, for highly anisotropic irregularities (bottom), the ratio is sensitive to the form of the spatial spectrum (Gaussian vs. power-law). One expects, then, that the ratio also may be sensitive to the index, p, of a power-law spectrum. Indeed, the right-hand side of Figure 29 shows that the phase-gradient ratio goes essentially as the effective-baseline ratio to the (p-1)/2 power.

Figure 30 shows graphically the sensitivity of the phase-gradient ratio to the spectral index and to irregularity anisotropy. It contains nine plots of r vs. penetration-point position during the pass employed in Figure 29. The three different line types correspond to three different values of the cross-field axial ratio, b, for fixed field-aligned axial ratio, a, as indicated in the legend. As desired, there is quite good separation of the curves for

69
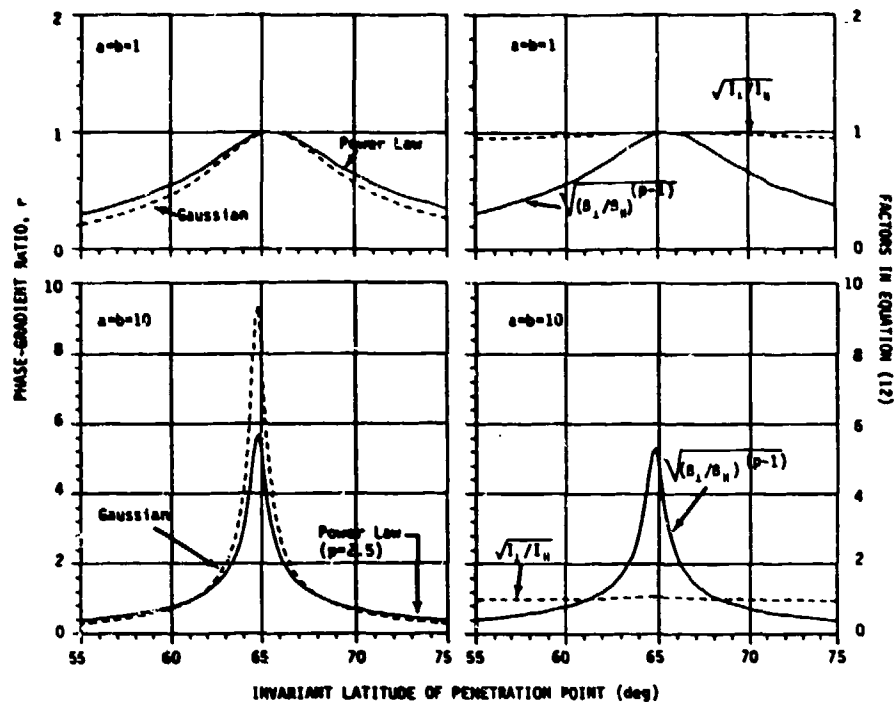
Figure 29. Illustrating (left) the sensitivity of the phase-gradient ratio, r, to the form of the spatial spectrum (Gaussian vs. power-law) and (right) the relative importance of the two factors in Equation (46). The top two sets of curves are for isotropic irregularities and the bottom two are for L-shell aligned (sheetlike) irregularities with axial ratios of 10:10:1.
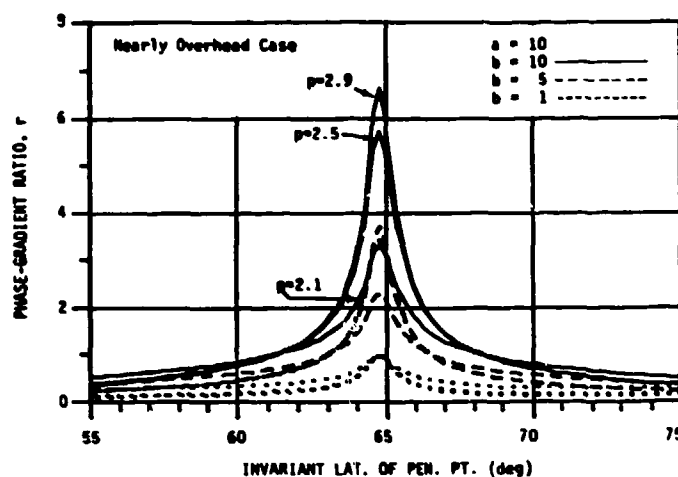
Figure 30. Illustrating the sensitivity of the phase-gradient ratio, r, to the cross-field axial ratio, b, for a fixed field-aligned axial ratio, a, of 10:1 and to the power-law spectral index, p, of phase.

different likely values of b, especially for the mid-pass geometry in which the line of sight is nearly along the magnetic field. (The peak in r for isotropic irregularities occurs at the geographic zenith, which happens to be close to the geomagnetic zenith at Poker Flat.)

Unfortunately, dependence of r on p is sufficiently strong as to render b ambiguous as a function of r. Three curves are shown for each value of b, employing values of p in the range observed at Poker Flat. For $r > 1$, the upper curve in each set is for $p = 2.9$, the middle curve is for $p = 2.5$, and the bottom one is for $p = 2.1$. (For $r < 1$, the order of the curves reverses.) Clearly, unless p and b are independent of latitude (which they probably are not), one cannot distinguish a situation, say, in which $b = 10$ and $p = 2.1$ from one in which $b = 5$ and $p = 2.5$.

The foregoing shows both the potential utility and a fundamental limitation to employing the phase-gradient ratio for determination of axial ratios. It appears that quantitative refinement of axial ratios from a large data population may be feasible using the phase-gradient ratio, but that underlying variations in them (e.g., latitudinal dependence) should be modeled with guidance from more general interferometer analysis (Livingston et al, 1982). Moreover, before application of the phase-gradient ratio for this purpose, it is necessary to obtain a value (or a functional description) of the phase spectral index independently. Phase spectral behavior is addressed in the next two subsections.

4-3 SPECTRAL-INDEX BEHAVIOR NEAR THE SUBAURORAL ENHANCEMENT

For several years, we have known that the values, p, of the phase spectral index observed in Wideband at Poker Flat vary with geomagnetic latitude of the penetration point, at least at night. Figure 31, which is adapted from Fremouw and Lansinger (1979), illustrates the observed dependence. The indicated behavior is potentially of interest for modeling because of the one-to-one relationship between p and the powerlaw index, q, of the in-$situ$ spatial spectrum of the irregularities ($q = p - 1$ in the absence of diffractive effects on the phase spectrum, given a thick scattering region). We did not pursue it initially, however, because of a concern that the observed increase in p for a restricted range of magnetic latitude might be an artifact of nonstationary phase statistics due to rapidly changing observing geometry as the line of sight swept through the region of geometrically imposed phase-scintillation enhancement (Fremouw et al, 1977; Rino et al, 1978).

Regardless of the geophysical reality, or lack thereof, of the latitudinal dependence of p illustrated in Figure 31, that dependence is pertinent to interpretation of phase-gradient measurements in terms of irregularity axial ratios. Moreover, recent incoherent-scatter observations of large-scale structures in the F layer, apparently restricted to the latitude regime near Poker Flat (e.g., Vickrey, 1982, Figure 1), are consistent with the possibility that Figure 31 reveals a true geophysical variation in q.

71
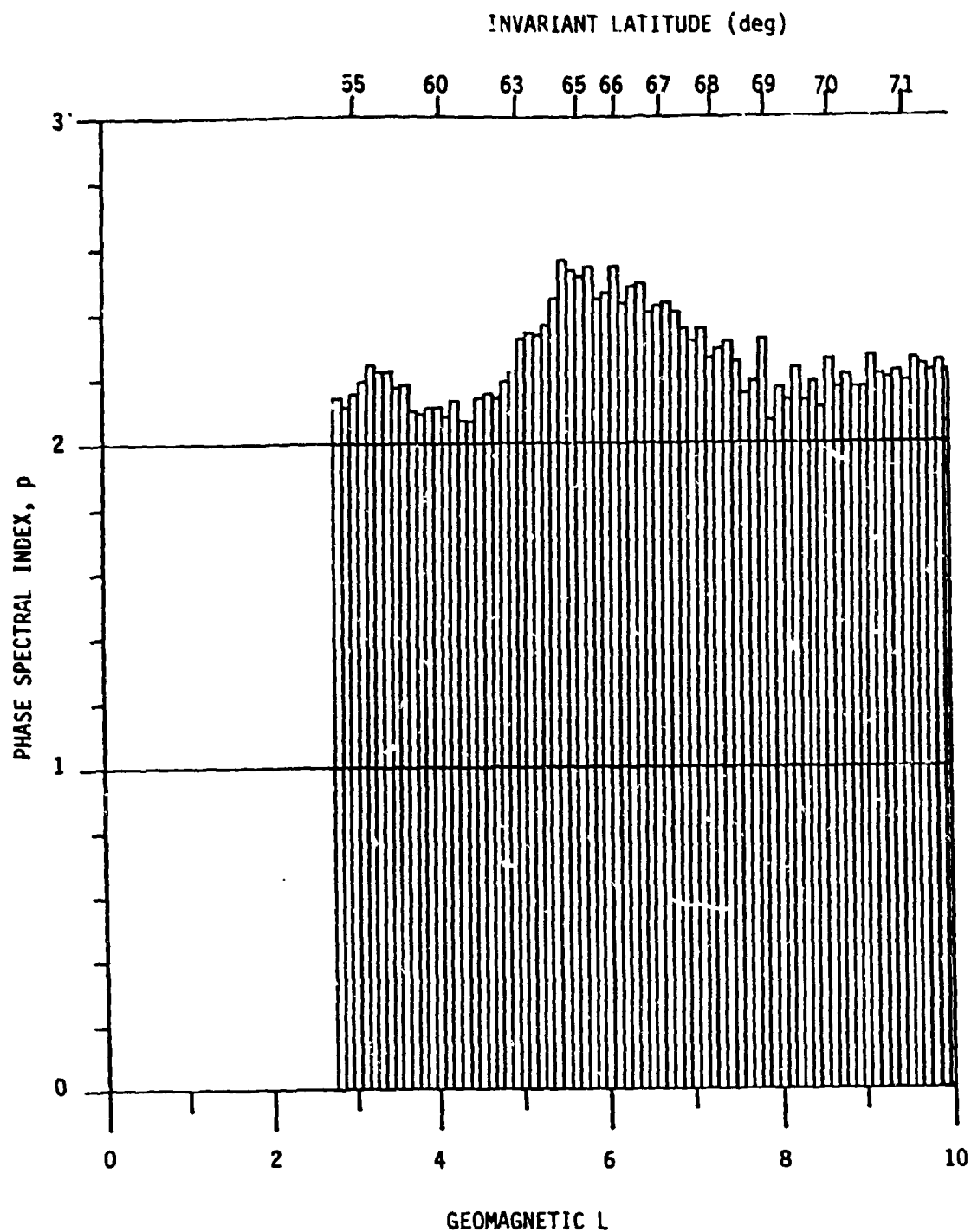
Figure 31. Relationship between VHF phase spectral index, p, and geomagnetic latitude (and L value) at the line-of-sight penetration point in the F layer.

In view of the foregoing, we conducted a preliminary investigation of the behavior of p in the nighttime Wideband data base from Poker Flat. The aggregate behavior and an internally consistent (but not uniquely proven) interpretation of it are described in this subsection.

Figure 31 shows an increase in p, at night, for penetration-point latitudes corresponding to magnetic L values between about 5 and 7.5. Our reason for doubting the geophysical significance of the observation stemmed from the existence of sheetlike irregularities in the nighttime subauroral ionosphere. The line of sight scans through grazing incidence on the L shells, along which such sheets are aligned, at L = 5.5. Our fear was that the scintillation enhancement occurring there might invalidate the stationary-statistics-based analysis from which the measured p values came.

We know that, as a dominant configuration, the sheetlike irregularities are confined to the night side of the earth (Fremouw and Lansinger, 1981b). One might suppose, therefore, that a test of the geophysical reality of the observed increase in p would be its presence or absence in daytime data; absence of the effect in the daytime would indicate that the nighttime increase is a geometrical artifact of the sheets. This reasoning is oversimplified, however, since the effect may well be associated with sheetlike structures but still have geophysical significance.

Nonetheless, there is a reliable test of the possible effect of geometrically imposed signal-statistical nonstationarity on our observed behavior of p: to look for a singular feature at the magnetic zenith in our daytime data base. The dominant configuration of daytime irregularities in the vicinity of Poker Flat is that of axially symmetric "rods" aligned along the magnetic field (Fremouw and Lansinger, 1981b). For such irregularities, the station's magnetic zenith represents a geometric "singularity," which is known to produce an enhancement in phase-scintillation strength as the line of sight sweeps through it. If the same rapid change in observing geometry does not produce an enhancement in p, we can be reasonably confident that our nighttime p enhancement is not imposed by a geometrically produced signal-statistical nonstationarity.

The original data set showing a broad p enhancement (Figure 31) contained best-fit spectral indices to 15,953 phase spectra obtained from all nighttime VHF Wideband data collected at Poker Flat during 1976 through 1978, except for exclusion of passes during which the local (College) K index was zero. Including all nighttime data (17,937 spectra from 1976 through 1979, with no K-index threshhold) produced little change in the behavior of p. The latter result is presented in Figure 32 (solid curve) in terms of average p as a function of the invariant latitude of the line-of-sight penetration point (at 350-km altitude). Shown for comparison (dotted curve) is a plot of average p from the 1,719 spectra available from daytime passes traversing within 10° of the magnetic zenith, which occurs at a penetration-point invariant latitude of 64.9°.
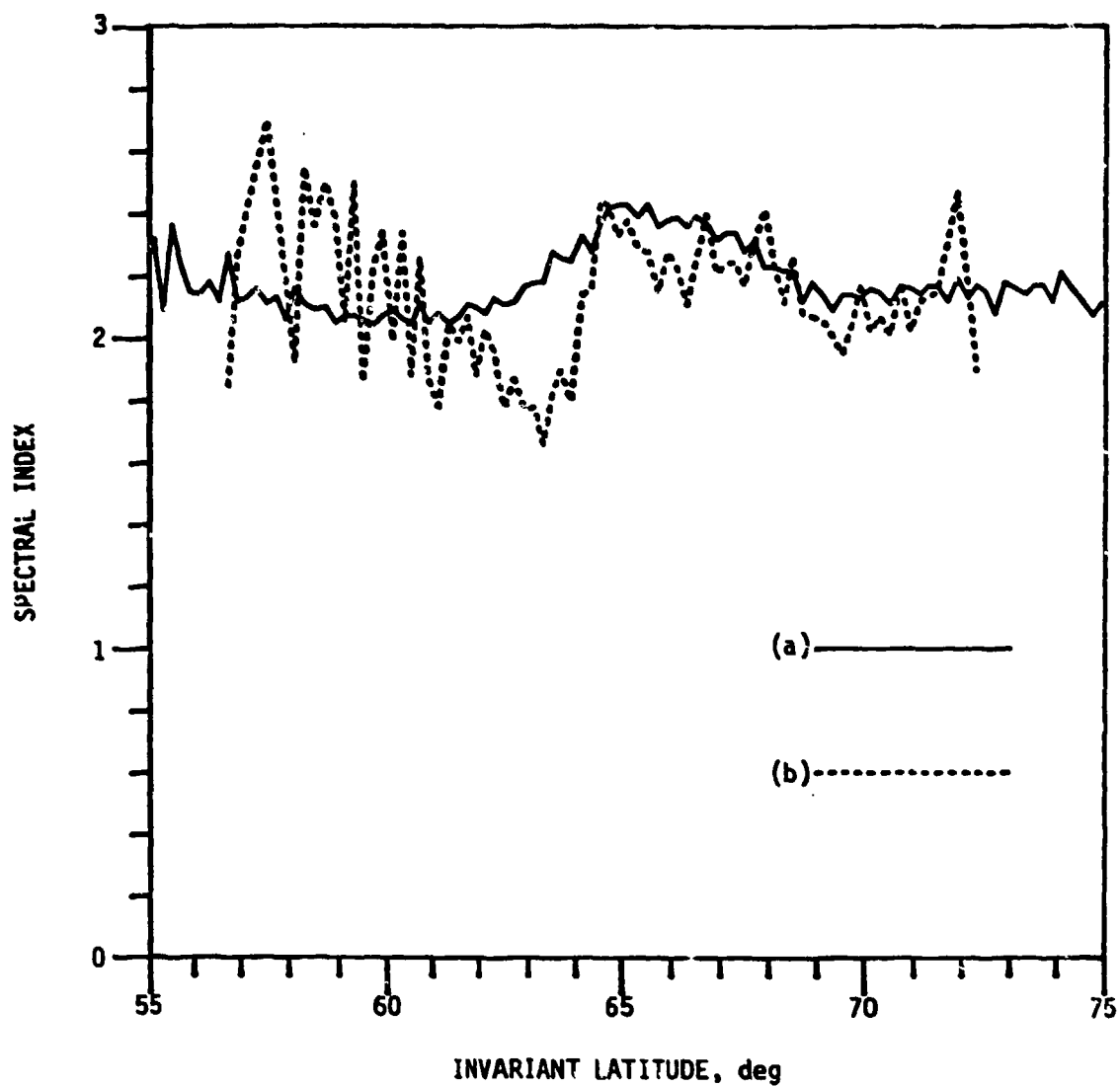
73

Figure 32. Average VHF phase spectral index, p, as a function of invariant latitude of the line-of-sight penetration point (at 350 km) for (a) all nighttime Wideband data from Poker Flat and (b) nearly overhead daytime passes.

74

We should like to argue either (1) that lack of a p enhancement in the dotted curve in Figure 32 attests to the geophysical significance of the enhancement clearly observed in the solid curve, or (2) that presence of an enhancement in the former indicates that the nighttime enhancement is a geometrical artifact. The results shown in Figure 32, however, do not seem definitive. There are more statistical fluctuations in the dotted curve, owing to the smaller number of data points, and a positive fluctuation does occur near the magnetic zenith.

In an attempt to resolve this geometrical/geophysical dilemma, we have resorted to a more directly geometrical ordering of the data. For each data point, we have calculated the angle between the line of sight and (1) the magnetic L shell and (2) the magnetic meridian, both calculated at a height of 350 km. To establish whether a geometrical "singularity" due to anisotropic irregularities produces an enhancement in p, we made a contour plot of average p values on a grid of off-shell and off-meridian angle. The question at hand should be answered by the presence or absence of a p enhancement at the origin of such a coordinate system for daytime data.

Figure 33 shows such a contour plot for all the 6,647 daytime spectra available within the look-angle window employed. There is no identifiable, statistically outstanding feature at the center of the plot.

The grid is oriented as if one were looking down on a map of Alaska. That is, positive off-meridian angles correspond to satellite locations to the (geomagnetic) east of Poker Flat, and positive off-shell angles correspond to northerly satellite positions. Daytime passes progressed in an approximately northwesterly direction. The daytime "overhead" pass corridor, from which data for the dotted curve in Figure 32 came, starts at coordinates of about +45°, -33°, on Figure 33, progresses slowly thereon through the lightly dappled region ($1.75 \leq p \leq 2.00$) centered near +20°,-20°, and then speeds up through the central region of the plot (but with the corridor center passing slightly to the upper right of 0°,0°). Tracing such a trajectory, one can pick out the features that rendered the dotted curve in Figure 32 nondefinitive. On Figure 33, they are seen to have no special geometrical significance.

Figure 34 contains a contour plot of average p values for the nighttime Wideband data. Unlike Figure 33, an ordered pattern clearly is present. Surprisingly, however, it is ordered in off-meridian angle as well as in off-shell angle. That is, the observed enhancement in p does not appear as a horizontal band, as one might have expected without a longitude-like separation of data from the solid curve in Figure 32. Rather, the p enhancement occurs preferentially away from the station's magnetic meridian.

The Wideband data base contains about twice as many nighttime data points as it does daytime points. In order to assess the statistical significance of differences observed between daytime and nighttime behaviors of p, the nighttime data population was decimated by using only every other chronologically ordered point in a given bin prior to the plotting of Figure 34. A total of 6,012 spectra contributed to Figure 34 (as compared with 6,647 for Figure

75
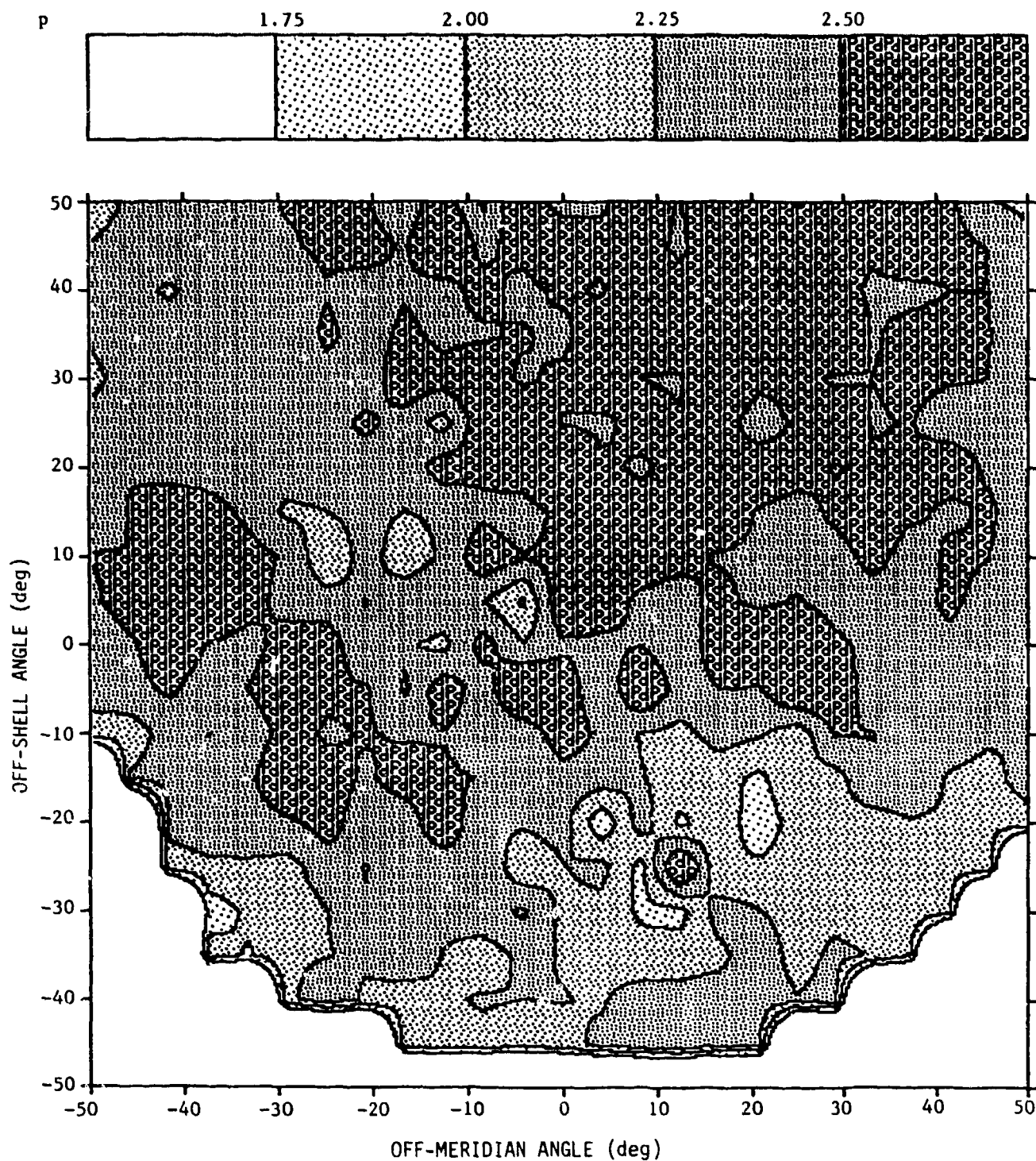
Figure 33. Contour plot of VHF phase-spectral index, p, for all daytime Wideband data from Poker Flat. Gray scale appears at top. Coordinate system refers to angle, calculated at 350-km altitude, between the line of sight and the local (x) magnetic meridian and (y) magnetic L shell.

76
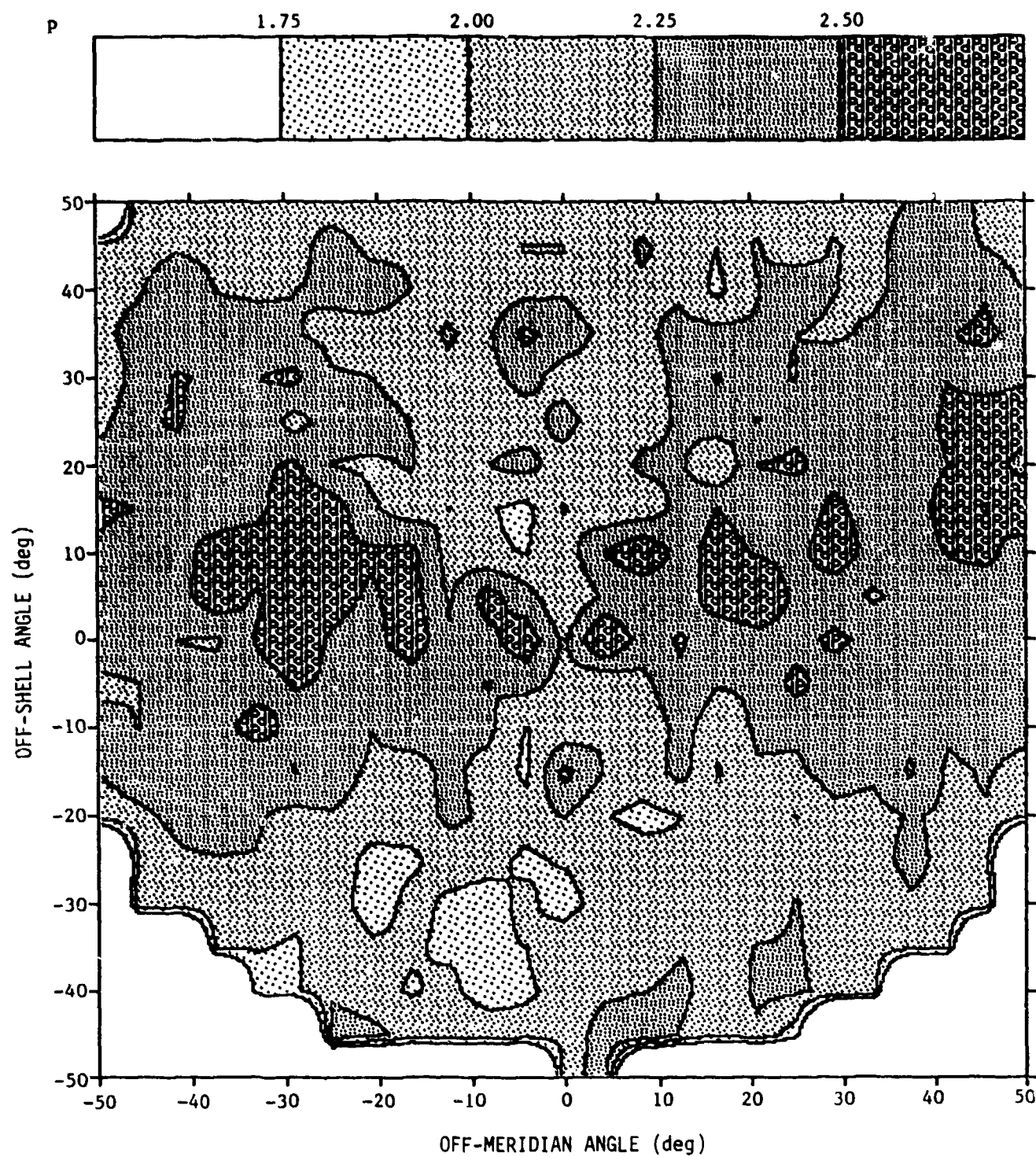
Figure 34. Contour plot of p, in same coordinate system as in Figure 2, for nighttime VHF data base decimated to provide statistical significance comparable to that of daytime data population.

2), and the numbers of points per bin were similar through the important central portions of the two plots. The full nighttime data population (p values from 11,811 spectra) was employed in Figure 35 in order to refine the presentation of p behavior.

Figure 35 reveals, even more clearly than Figure 34, the tendency for the nighttime enhancement in p to avoid the magnetic meridian. Indeed, this initially puzzling behavior was observed in nighttime corridor data sets before contour plots of p were produced. (Nighttime passes progress essentially vertically on the off-meridian/off-shell coordinate system.)

As a working hypothesis, the following interpretation of Figure 35 is offered. Suppose that the "sheetlike" irregularities (Rino et al, 1978) responsible for the scintillation enhancement (Fremouw et al, 1977) observed by means of Wideband at Poker Flat are confined primarily to the large-scale end of the scintillation-producing spectrum. That is, suppose that the smaller-scale irregularities are more nearly axially symmetric than are the large ones. An idealized picture would be small-scale "rods" imbedded in large-scale "sheets."

The scintillation enhancement has been defined mostly in terms of the integral, σ_{ϕ}^{2}, of the phase spectrum. This phase variance is thought to be enhanced by quasi-coherent addition of phase perturbations as a radio wave propagates along an elongated axis of (sheetlike or rodlike) irregularities. The same process would occur for the rod/sheet mix postulated in the foregoing paragraph. For such a mix, however, the phase spectrum would be uniformly enhanced only near the magnetic zenith, while there would be preferential enhancement of the large-scale end of the spectrum at large off-meridian angles (and small off-shell angles). For the latter geometry, quasi-coherent phase addition would arise in the (large-scale) sheetlike irregularities but not in the (small-scale) rodlike irregularities.

The foregoing qualitative reasoning does not allow us totally to distinguish geometrical from geophysical sources of the p enhancement. We assert only that the absence of a p enhancement at 0°,0° in Figure 2 permits us to accept the enhancement shown in the solid curve of Figure 32 as "real" -- i.e., as other than an artifact due to geometrically imposed signal-statistical nonstationarity. We cannot yet unequivocally interpret the observed p enhancement directly as a latitudinally ordered q enhancement. Still, there is now abundant evidence that the nightside F layer between L of about 5 and 7 is a special region as regards plasma-density structure.

A likely sequence of events in the aforementioned region would be one initiated by soft electron precipitation (Tanskanen et al, 1981) setting up latitudinally nonuniform F-layer ionization observed by Vickrey (1982) by means of incoherent scatter and by Rino and Owen (1980) and Leitinger et al (1982) as TEC enhancements. This L-shell-aligned large-scale structure would form a "reservoir" spectral regime from which smaller-scale structure would bifurcate into a cascade regime by means of convective instability.

As a new element in the picture, the p behavior reported and tentatively interpreted here may indicate a trend toward cross-field isotropy in the cascade regime. Thus, there would be no
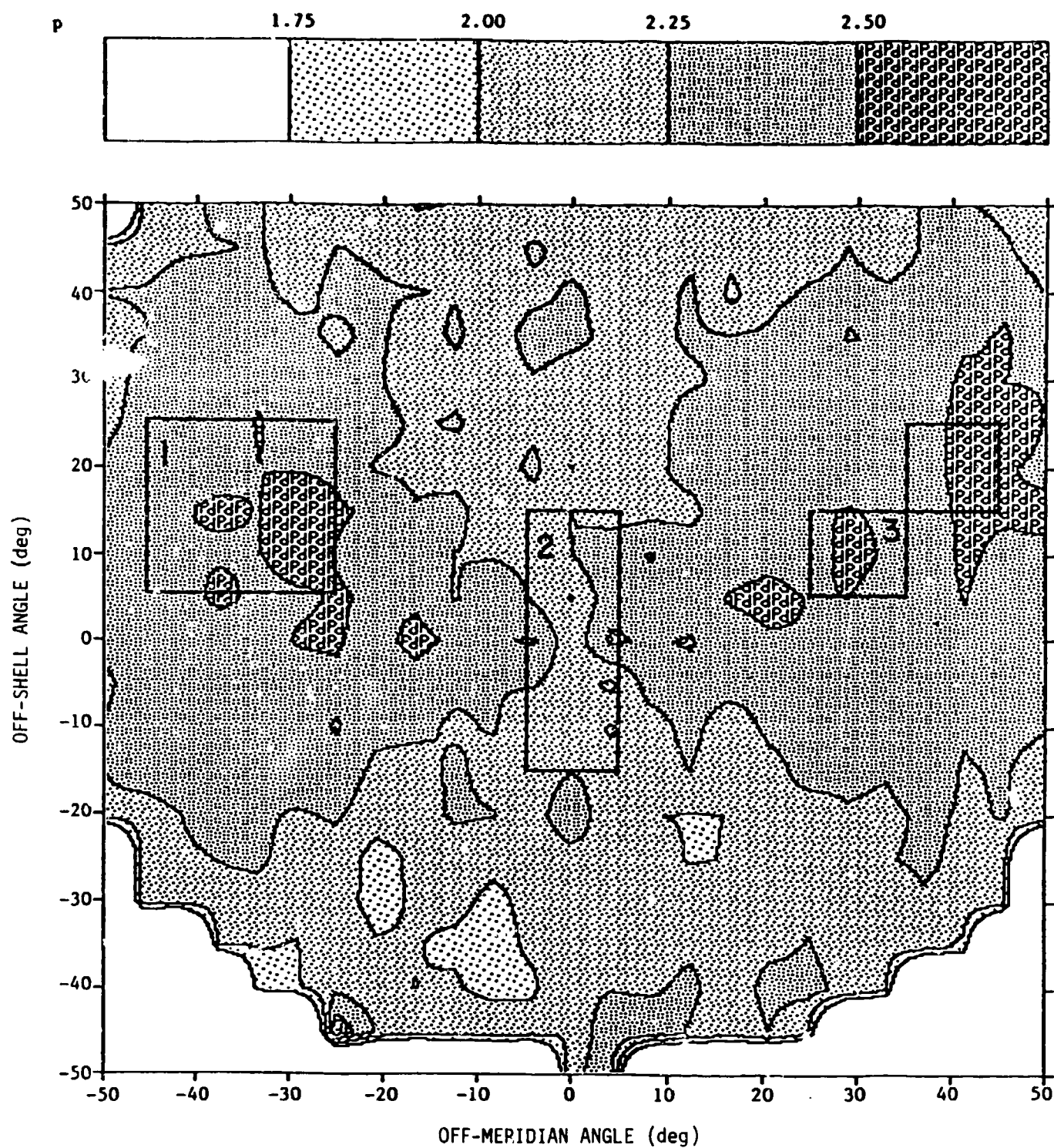
Figure 35. Contour plot of p using entire nighttime VHF Wideband data base from Poker Flat. Rectangles show regions of data selected for detailed spectral analysis.

need for nonlinear production of L-shell-aligned structures by convective processes, which do not seem to be a dominant result of NRL's simulations (Keskinen and Ossakow, 1982 and references therin). One may envision a multistage cascade process in which each generation produces structure not only smaller than itself but also oriented perpendicular to its own dominant alignment (parallel to its own dominant gradient). Many generations taken together would display cross-field isotropy, but the largest (reservoir-regime) structures would remain anisotropic.

For propagation calculations, the foregoing picture could be modeled by means of a two-component spectrum. Signal-statistically, the situation might be likened to the two-component model described by Fremouw *et al* (1980), in which the large-scale component is responsible for large phase perturbations and geometrical-optics focusing and defocusing, while the small-scale component produces diffractive scatter. Now, however, the two components would have a phenomenological basis also, distinguishable not only in scale-size but in degree of anisotropy.

4-4 SPECTRAL FEATURES

The spectral index, p, behaving as described in Subsection 4-2, is obtained (by SRII) from log-linear fits to phase spectra between 0.5 and 10.0 Hz. Designed for bulk processing, the fitting procedure presupposes a simple (one-component) power-law spectrum. Automated fits to more complicated spectra could produce unexpected, and even systematic, behaviors of fit parameters such as p. Thus, a necessary step in the investigation is a visual inspection of selected spectra.

Passes for initial inspection of selected spectra have been chosen in the following manner. The rectangular boxes on Figure 35 represent masks used for convenient selection of pass segments for comparison of the disparate behaviors noted near and away from the local meridian. In terms of routine 20-second processing periods for which we have detrend data, we found 17 points from six passes in Region 1, 22 points from five passes in Region 2, and 28 points from nine passes in Region 3. For initial inspection, we have selected periods of high p from Regions 1 and 3 and periods of low p from Region 2.

Table 9 below indicates, in terms of routine 20-second periods, that the points obtained in the detrend-data masking procedure are consistent with the behavior of p in the overall (summary-data) nighttime population from Poker Flat.

TABLE 9 SELECTED DATA

Region	No. of Points		
	Total	p > 2.5	p < 2.0
1	17	7	3
2	22	2	13
3	28	8	2

We selected 15 of the aforementioned 20 passes for detailed spectral analysis, including a preponderance showing the p-behavior illustrated in Figure 35, a few counter-examples, and one very weak-scintillation pass as a check on noise effects. For each of the 15 passes, we plotted the phase time series for five or six minutes including the scintillation enhancement. The time-series plots were used to hand-select 20-second periods showing reasonable statistical stationarity, for spectral analysis. Periods totally inside the enhancement region and totally outside the region were being sought, and transition periods are have been identified.

Figures 36 shows some of the spectra computed after the foregoing selection. The cases were chosen as exemplary of behavior well off (a, from Region 3) and near (b, from Region 2) the magnetic meridian. The former (a, Pass 61-33) shows an ordered increase in p through the off-meridian enhancement region. The latter (b, Pass 52-46) is an extreme example of near-meridian behavior. Not only does p remain at values well below the maximum achieved in the off-meridian case, but it actually decreases substantially in the strongest portion of the scintillation enhancement (as identified on the time-series plot).

The spectra illustrated in Figures 36 were obtained using a Blackman-Harris window. The first data point (0.1 Hz) was elevated by 3 dB to offset detrender suppression, and a five-bin centered smoother (modified to avoid end effects) has been applied. The straight lines superimposed on the spectra represent log-linear best fits in the spectral band routinely employed for that purpose in Wideband summary processing. The spectra shown are quite well approximated by single-component power laws in that band and above, although several show some enhancement in a lower-frequency (reservoir?) band. The noise floor is at about -70 dB on the scale indicated. The p values derived from the routine fit procedure are indicated on the plots.

The first and last spectra in both Figures 36 a and b are from outside the geometrical enhancement, and they exhibit p values approximating that currently employed in WBMOD (2.5).

81
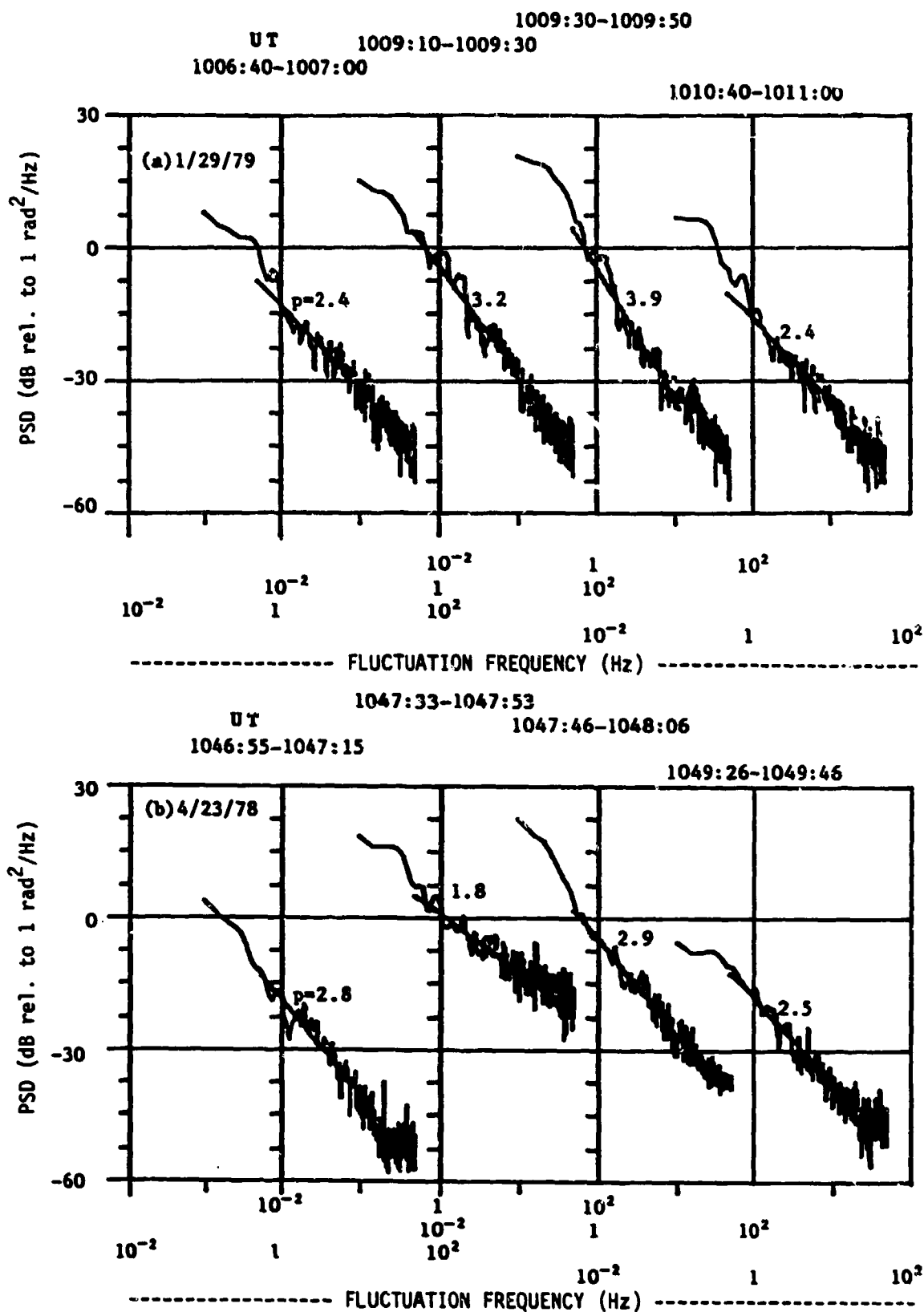
Figure 36. VHF phase spectra from an off-meridian (a) and a near-meridian (b) Wideband pass over Poker Flat, both nighttime. Note opposite spectral-behavior.

The central two spectra in each case are from the enhancements, and they show the opposite spectral-index behaviors described above. (Note that the central two spectra in Figure 36b are from overlapped time periods in Pass 52-46, which displayed a narrower enhancement than did Pass 61-33.) Qualitatively, it appears that the off-meridian enhancement preferentially affected large-scale structures, whereas all scales were enhanced -- and especially small ones in the present example -- near the magnetic zenith. (The peak enhancement in Pass 52-46 occurred as the line-of-sight passed within about two degrees of field-alignment.)

Reliable interpretation must await inspection and analysis of several additional cases, including consideration of less simple spectra than those shown in Figure 36. Of the approximately one hundred spectra so far inspected, about three-quarters display some general spectral enhancement above the routine linear fit at frequencies below 0.5 Hz (~ 6 km wavelength in the line-of-sight scan direction). The second most common departure from single-component power-law behavior is a downward break at the high-frequency end, as found by Rino et al (1981) in in-situ data from the equator. About a quarter of the spectra inspected for this study show such a break, typically at about ten Hz (~ 300 meters wavelength in the line-of-sight scan direction) or slightly lower. One of the most obvious examples is shown in Figure 37.

In the case shown, which is from Poker Flat Pass 12-19, the shallow-slope band happens to coincide with the band used for routine spectral fitting. In other cases, such coincidence does not occur, and the best-fit p value then has little relevance. A single power law is still a good first approximation to the majority of spectra inspected, but there are departures, as noted.

As discussed by Rino at the 1982 DNA Summer Study, it is tempting to interpret spectra such as that in Figure 37 in terms of "reservoir, cascade, and diffusion" regimes. There is still a good deal of uncertainty about such a characterization, however. For instance, a 3-dB difference between log-linear best fits to phase spectra in bands below and above the Fresnel frequency could be explained simply in terms of weak-scatter diffraction theory.
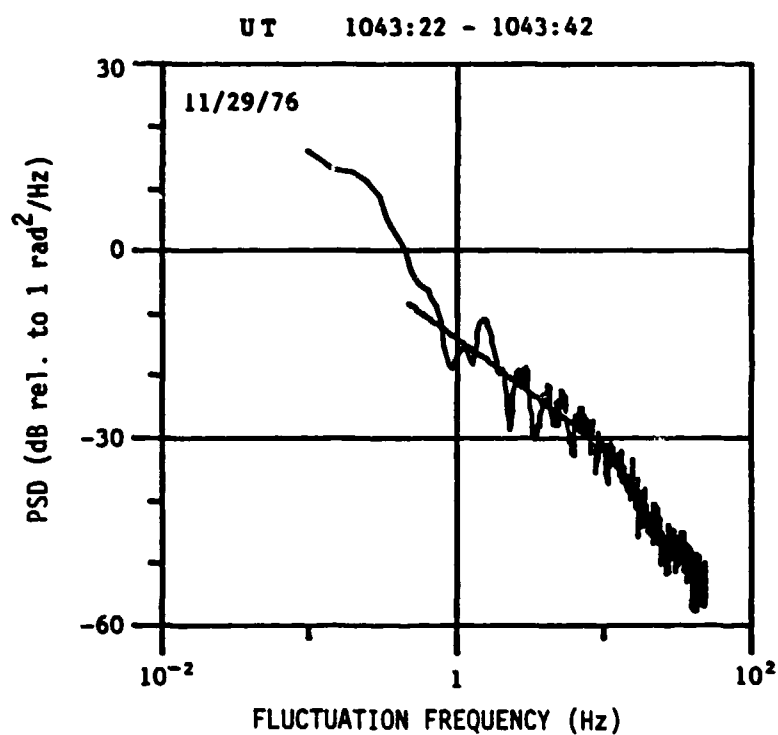
Figure 37. VHF phase spectrum displaying a high-frequency break as well as a low-frequency band that is enhanced with respect to the best log-linear fit between 0.5 and 10.0 Hz.

SECTION 5

CONCLUSION

WBMOD Rev 6B3 represents the state of the art of descriptive modeling of auroral-zone scintillation for systems-evaluation use. The version of it implemented at USAF Global Weather Central contains the same model, the code being configured for more nearly real-time link analysis on the basis of current geophysical input conditions. Neither version is likely to give a consistently satisfactory description of equatorial scintillation.

In the near future, WBMOD will be iteratively tested against equatorial scintillation data obtained by means of Wideband at Kwajalein, Marshall Islands; and Ancon, Peru. This work will be guided by the comparative morphology of Livingston (1978) and the physical insights of Dachev and Walker (1983) and/or Tsunoda (1983).

The drift-velocity model described in this report requires additional calibration, particularly of its behavior in the night exit region. The existing Wideband-Poker Flat data base will be used in this calibration, as well as data from the various auroral incoherent scatter radars (Foster, 1983), and from the HILAT experiment when its data become available.

Meanwhile, research will continue into the three-dimensional spectral characteristics of scintillation-producing irregularities in the auroral F layer. Current information on the latitudinal dependence of irregularity axial ratios (Livingston *et al*, 1982) will be incorporated into WBMOD. Beyond that, an attempt will be made to ascertain whether cross-field anisotropy may be restricted in scale size as well as in geomagnetic latitude and time.

The three-dimensional spatial spectrum of plasma structures is expected to hold important clues about their generation, evolution, and decay. Thus, it will continue to be explored with Wideband data. Moreover, the ability of scintillation measurements to yield such informaton is expected to constitute a major contribution to the beacon experiment in the forthcoming HILAT Satellite Program.

APPENDIX

Potential-Model Functions

The $G(\theta)$ latitudinal functions and their derivatives are as follows (these equations are implemented in Subroutine GFUNC):

__Region 1:__ $\theta \geqslant \theta_1$

$$G(\theta) = A_1 \left(\frac{\sin \theta}{\sin \theta_0}\right)^{r_1} \tag{A-1a}$$

$$\frac{\partial G(\theta)}{\partial \theta} = r_1 \, G(\theta) \cot \theta \tag{A-1b}$$

__Region 1T:__ $\theta_1 > \theta \geqslant \theta_0$

$$G(\theta) = \left[1 - \frac{(\theta - \theta_0)^2}{B_1}\right]^{\frac{1}{2}} \tag{A-2a}$$

$$\frac{\partial G(\theta)}{\partial \theta} = - \frac{(\varepsilon - \theta_0)}{G(\theta)B_1} \tag{A-2b}$$

__Region 2T:__ $\theta_0 > \theta > \theta_1$

$$G(\theta) = \left[1 - \frac{(\theta_0 - \theta)^2}{B_1}\right]^{\frac{1}{2}} \tag{A-3a}$$

$$\frac{\partial G(\theta)}{\partial \theta} = \frac{(\theta_0 - \theta)}{G(\theta)B_2} \tag{A-3b}$$

__Region 2:__ $\theta \leq \theta_1$

$$G(\theta) = A_2 \left\{\left[\frac{\sin (\theta + \theta_c)}{\sin \theta_0}\right]^{r_2} - \left(\frac{\sin \theta_r}{\sin \theta_0}\right)^{r_2}\right\} \tag{A-4a}$$

$$\frac{\partial G(\theta)}{\partial \theta} = r_2 A_2 \left[\frac{\sin(\theta + \theta_c)}{\sin \theta_0}\right]^{r_2} \cot (\theta + \theta_c) \tag{A-4b}$$

86

The $F(\phi,\theta)$ magnetic local time equations and their derivatives are as follows (these equations are implemented in Subroutine FFUNC):

Dayside Cleft: $\phi_d - \phi_i^- \leqslant \phi \leqslant \phi_d + \phi_i^+$

$$F(\phi,\theta) = \bar{\psi} + \frac{\Delta\psi}{2} \cos \phi_d(\phi) \tag{A-5a}$$

$$\frac{\partial F(\phi,\theta)}{\partial \phi} = -\frac{\pi}{2} \left[\frac{\Delta\psi}{\phi_i^+ + \phi_i^-} \right] \sin \phi_d(\phi) \tag{A-5b}$$

$$\frac{\partial F(\phi,\theta)}{\partial \theta} = -\frac{\pi}{2} \left[\frac{\Delta\psi}{\phi_i^+ + \phi_i^-} \right] \left[\frac{\phi_i^+ \frac{\partial \phi_i^-}{\partial \theta} - \phi_i^- \frac{\partial \phi_i^+}{\partial \theta}}{\phi_i^+ + \phi_i^-} \right] \sin \phi_d(\phi) \tag{A-5c}$$

where $\phi_d(\phi) = \pi \left[\dfrac{\phi - (\phi_d - \phi_i^-)}{\phi_i^+ + \phi_i^-} \right]$

$$\bar{\psi} = \tfrac{1}{2}(\psi_M + \psi_E)$$

$$\Delta\psi = \psi_M - \psi_E$$

$$\phi_i^\pm = \phi_d^\pm + \left(\frac{\theta - \theta_0}{\theta_0} \right) \left(\frac{\pi}{2} - \phi_d^\pm \right)$$

$$\frac{\partial \phi_i^\pm}{\partial \theta} = 2 \left(\frac{\theta - \theta_0}{\theta_0^2} \right) \left(\frac{\pi}{2} - \phi_d^\pm \right)$$

Evening Sector: $\phi_d + \phi_i^+ < \phi < \phi_n - \phi_a^-$

$$F(\phi,\theta) = \psi_E \tag{A-6a}$$

$$\frac{\partial F(\phi,\theta)}{\partial \phi} = 0 \tag{A-6b}$$

$$\frac{\partial F(\phi,\theta)}{\partial \theta} = 0 \tag{A-6c}$$

87

<u>Night Exit Region:</u> $\phi_n - \phi_a \leq \phi \leq \phi_n + \phi_a^i$

$$F(\phi,\theta) = \bar{\psi} - \frac{\Delta\psi}{2} \cos \phi_n(\phi) \tag{A-7a}$$

$$\frac{\partial F(\phi,\theta)}{\partial \phi} = \frac{\pi}{2} \left[\frac{\Delta\psi}{\phi_a^+ + \phi_a^-} \right] \sin \phi_n(\phi) \tag{-7b}$$

$$\frac{\partial F(\phi,\theta)}{\partial \phi} = \frac{\pi}{2} \left[\frac{\Delta\psi}{\phi_a^+ + \phi_a^-} \right] \left[\frac{\phi_a^+ \frac{\partial \phi_a^-}{\partial \theta} - \phi_a^- \frac{\partial \phi_a^+}{\partial \theta}}{\phi_a^+ + \phi_a^-} \right] \sin \phi_n(\phi) \tag{A-7c}$$

where $\phi_n(\phi) = \pi \left[\frac{\phi - (\phi_n - \phi_a^-)}{\phi_a^+ + \phi_a^-} \right]$

$$\phi_a^\pm = \phi_n^\pm + \left(\frac{\theta - \theta_0}{\theta_0} \right)^2 \left(\frac{\pi}{2} - \phi_n^\pm \right)$$

$$\frac{\partial \phi_a^\pm}{\partial \theta} = 2 \left(\frac{\theta - \theta_0}{\theta_0^2} \right) \left(\frac{\pi}{2} - \phi_n^\pm \right)$$

<u>Morning Sector:</u> $\phi_n + \phi_a^+ < \phi < \phi_d - \phi_i^-$

$$F(\phi,\theta) = \psi_m \tag{A-8a}$$

$$\frac{\partial F(\phi,\theta)}{\partial \phi} = 0 \tag{A-8b}$$

$$\frac{\partial F(\phi,\theta)}{\partial \theta} = 0 \tag{A-8c}$$

REFERENCES

____(1977), Automated Data Systems Documentation Standards, DoD Standard 7935.1-S, Department of Defense, Washington, DC.

Basu, S., S. Basu, R. Livingston, E. MacKinzie, and H. Whitney (1982), "Phase and Amplitude Scintillation Statistics at 244 MHz from Goose Bay Using a Geostationary Satellite, AFGL-TR-82-0222, Hanscom AFB, MA.

Cauffman, D.P. and D.A. Gurnett (1972), "Satellite Measurements of High-Latitude Convection Electric Fields," Space Sci. Rev., 13, 369.

Dachev, Ts.P. and J.C.G. Walker (1982), "Seasonal Dependence of the Distribution of Large-Scale Plasma Depletions in the Low-Latitude F Region," J. Geophys. Res., 87, 7625.

Dandekar, B.S. (1979), "Study of the Equatorward Edge of the Auroral Oval from Satellite Observations," AFGL-TR-79-0010, Hanscom AFB, MA.

Feldstein, Y.I. (1963), "On Morphology of Auroral and Magnetic Disturbances at High Latitudes," Geomagn. Aeron., 3, 183.

Foster, J.C. (1983), "An Empirical Electric Field Model Derived from Chatanika Radar Data," J. Geophys. Res., 88, 981.

Fremouw, E.J. (1982), "SESP Space Flight Request: DNA POlar Satellite," DD Form 1721, March 1982.

Fremouw, E.J. and J.M. Lansinger (1979), "Continued Geophysical Analysis of Coherent Satellite Scintillation Data," Physical Dynamics Report PD-NW-79-213R, Annual Report on Contract F49620-78-C-0014, Physical Dynamics, Inc., Bellevue, WA, 98009.

Fremouw, E.J. and J.M. Lansinger (1981b), "Dominant Configuration of Scintillation-Producing Irregularities in the Auroral Zone," J. Geophys. Res., 86(11).

Fremouw, E.J. and J.M. Lansinger (1981a), "A Computer Model for High-Latitude Phase Scintillation Based on Wideband Satellite Data from Poker Flat," DNA 5686F, Defense Nuclear Agency, Washington, DC.

Fremouw, E.J., R.L. Leadabrand, R.C. Livingston, M.D. Cousins, C.L. Rino, B.C. Faur, and R.A. Long (1978), "Early Results from the DNA Wideband Satellite Experiment--Complex-Signal Scintillation," Rad. Sci., 13(1), 167-187.

Fremouw, E.J., R.C. Livingston, and D.A. Miller (1980), "On the Statistics of Scintillating Signals," J. Atmos. Terr. Phys., 42, 717-731.

Fremouw, E.J., C.L. Rino, R.C. Livingston, and M.C. Cousins (1977), "A Persistent Subauroral Scintillation Enhancement Observed in Alaska," _Geophys. Res. Ltrs._, _4_(11), 539.

Heelis, R.A. (1982), "The Polar Ionosphere," _Rev. Geophys. Space Phys._, _20_, 567.

Heelis, R.A., W.B. Hanson, and J.L. Burch (1976), "Ion Convection Velocity Reversals in the Dayside Cusp," _J. Geophys. Res._, _81_, 3803.

Heelis, R.A., J.K. Lowell, and R.W. Spiro (1982), A Model of the High-Latitude Ionospheric Convection Potential," _J. Geophys. Res._, _87_, 6339.

Heelis, R.A., J.D. Winningham, W.B. Hanson, J.L. Burch (1980), "The Relationships Between High-Latitude Convection Reversals and the Energetic Particle Morphology Observed by Atmospheric Explorer," _J. Geophys. Res._, _85_, 3315.

Heppner, J.P. (1972), "Polar-cap Electric Field Distributions Related to the Interplanetary Magnetic Field Direction," _J. Geophys. Res._, _77_, 4877.

Heppner, J.P. (1973), "High Latitude Electric Fields and the Modulations Related to Interplanetary Magnetic Field Parameters," _Radio Sci._, _8_, 933.

Heppner, J.P. (1977), "Empirical Models of High-Latitude Electric Fields," _J. Geophys. Res._, _82_, 1115.

Holzworth, R.H. and C.-I. Meng (1975), "Mathematical Representation of the Auroral Oval," _Geophys. Res. Lett._, _2_, 377.

Kawasaki, K. (1975), "A Model of the Electric Field Over the Polar Cap," _Rep. Ionos. Space Res. Jap._, _29_, 157.

Keskinen, M.J. and S.L. Ossakow (1982), "Theories of High Latitude Ionospheric Irregularities: A Review, _NRL Memorandum Report 4949_, Naval Research Laboratory, Washington, DC.

Kluge, G. (1970), "Computer Program _SHELL_ for the Calculation of B and L from Models of the Geomagnetic Field," _ESOC Internal Note No. 67_, Darmstadt, Germany.

Leitinger, R., G.K. Hartmann, W. Degenhardt, A. Hedberg, and P. Tanskanen (1982), "The Electron Content of the Ionosphere and the Southern Boundary of Diffuse Aurora," _J. Atmos. & Terr. Phys._, _44_(4).

Livingston, R.C. (1978), Comparative Equatorial Scintillation Morphology - American and Pacific Sectors, _DNA 4644T_, Defense Nuclear Agency, Washington, DC.

Livingston, R.C., C.L. Rino, J. Owen, and R.T. Tsunoda (1982), "The Anisotropy of High-Latitude Nighttime F-Region Irregularities," SRI International Topical Report, Contract DNA001-81-C-0076.

McNish, A.G. (1936), "Geomagnetic Coordinates for the Entire Earth," Terr. Mag., 41(1), 37-43.

Meng, C.-I. (1981), "Electron Precipitation in the Midday Auroral Oval," J. Geophys. Res., 86 2149.

Meng, C.-I., R.H. Holzworth, and S.-I. Akasofu (1977), "Auroral Circle Delineating the Poleward Boundary of the Quiet Auroral Belt," J. Geophys. Res., 82, 164.

Perrault, P. and S.-I. Akasofu (1978), "A Study of Geomagnetic Storms," Geophys. J. R. Astron. Soc., 54, 547.

Reiff, P.H., R.W. Spiro, and T.W. Hill (1981), "Dependence of Polar Cap Potential Drop on Interplanetary Parameters," J. Geophys. Res., 86,7639.

Rino, C.L. (1979), "A Power Law Phase Screen Model for Ionospheric Scintillation. 1. Weak Scatter," Rad. Sci., 14(6), 1135.

Rino, C.L. and E.J. Fremouw (1977), "The Angle Dependence of Singly Scattered Wavefields," J. Atmos. and Terr. Phys., 39, 859.

Rino, C.L., E.J. Fremouw, R.C. Livingston, M.D. Cousins, and B.C. Fair (1977), "Wideband Satellite Observations," DNA 4399F, Defense Nuclear Agency, Washington, D.C.

Rino, C.L., E.J. Fremouw, A.R. Hessing, and V.E. Harfield (1978), "Two Fortran Programs for Calculating Global Ionospheric Amplitude and Phase Scintillation," RADC-TR-78-87, Rome Air Development Center, Griffiss AFB, NY.

Rino, C.L. and R.C. Livingston (1982), "On the Analysis and Interpretation of Space-Receiver Measurements of Transionospheric Radio Waves," Radio Sci., 17, 845.

Rino, C.L., R.C. Livingston, and S.J. Matthews (1978), "Evidence for Sheetlike Auroral Ionospheric Irregularities," Geophys. Res. Ltrs., 5 (12), 1039.

Rino, C.L. and J. Owen (1980), "The Structure of Localized Nighttime Auroral Zone Scintillation Enhancements," J. Geophys. Res., 85 (A6), 2941-2948.

Rino, C.L., R.T. Tsunoda, J. Petriceks, and R.C. Livingston (1981), "Simultaneous Rocket-Borne Beacon and In-Situ Measurements of Equatorial Spread F --Intermediate Wavelength Results," J. Geophys. Res., 86(A4), 2411.

Secan, J.A. (1982), "WBMOD Scintillation Model System Documentation,
   Vol. I.   Functional Description
   Vol. II.   Users Manual
   Vol. III.   Program Maintenance Manual (with D.A. Miller)
   Vol. IV.   Test Plan

91

Vol. V. Test Analysis Report

PD-NW-82-273R, Physical Dynamics, Inc., Bellevue, WA.

Tanskanen, P.J., D.A. Hardy, and W.J. Burke (1981), "Spectral Characteristics of Precipitating Electron Associated with Visible Aurora in the Premidnight Oval During Periods of Substorm Activity," J. Geophys. Res., 86(A3).

Tatarski, V.I. (1971), "The Effects of the Turbulent Atmosphere on Wave Propagation," US Department of Commerce, National Technical Information Service, Springfield, VA.

Tsunoda, R.T. (1983)

Vickrey, J.F. (1982), "On the Morphology of Plasma Density Irregularities in the Auroral F-Region," Topical Report for Period 15 Jan 1981 - 15 Mar 1982, Contract DNA001-81-C-0076, SRI International, Stanford, CA.

Volland, H. (1978), "A Model of Magnetospheric Electric Convection Field," J. Geophys. Res., 83, 2695.

Wittwer, L.A. (1979), "Radio Wave Propagation in Structured Ionization for Satellite Applications," DNA 5304D, Defense Nuclear Agency, Washington, DC.

Wolf, R.A. (1974), "Calculation of Magnetospheric Electric Fields," Magnetospheric Physics, B. McCormac, ed., D. Reidel, Dodrecht, Netherlands, p. 167.

Zi, M.-Y. and E. Nelson (1982), "Spacial Variations of Electric Fields in the High-Latitude Ionosphere," J. Geophys. Res., 87, 5202.

Zi, M.-Y., W. Lei, R. Gendrin, and B. Higel (1982), "The Harang Discontinuity and the Evening Plasmapause Boundary: A STARE-GOES Intercomparison," J. Atmos. Terr. Phys., 44 671.

DISTRIBUTION LIST

DEPARTMENT OF DEFENSE

Command & Control Technical Center
    ATTN: C-312, R. Mason
    ATTN: C-650, G. Jones
    ATTN: C-650
3 cy ATTN: C-650, W. Heidig

Defense Communications Agency
    ATTN: Code 230
    ATTN: Code 205
    ATTN: J300 for Yen-Sun Fu

Defense Nuclear Agency
    ATTN: STNA
    ATTN: NAFD
    ATTN: RAEE
    ATTN: NATD
    ATTN: RAAE, P. Lunn
3 cy ATTN: RAAE
4 cy ATTN: TITL

Defense Technical Information Center
12 cy ATTN: DD

Field Command
Defense Nuclear Agency, Det 1
Lawrence Livermore Lab
    ATTN: FC-1

Field Command
Defense Nuclear Agency
    ATTN: FCTT, G. Ganong
    ATTN: FCTXE
    ATTN: FCTT, W. Summa
    ATTN: FCPR

DEPARTMENT OF THE ARMY

Atmospheric Sciences Laboratory
    ATTN: DELAS-EO, F. Niles

BMD Advanced Technology Center
    ATTN: ATC-R, J. Russ
    ATTN: ATC-O, W. Davies
    ATTN: ATC-R, W. Dickinson
    ATTN: ATC-T, M. Capps

Harry Diamond Laboratories
    ATTN: DELHD-NW-P
    ATTN: DELHD-NW-R, R. Williams

US Army Comm-Elec Engrg Instal Agency
    ATTN: CCC-EMEO-PED, G. Lane
    ATTN: CCC-CED-CCO, W. Neuendorf

US Army Communications Command
    ATTN: CC-OPS-W
    ATTN: CC-OPS-WR, H. Wilson

US Army Communications R&D Command
    ATTN: DRDCO-COM-RY, W. Kesselman

US Army Nuclear & Chemical Agency
    ATTN: Library

DEPARTMENT OF THE ARMY (Continued)

US Army Satellite Comm Agency
    ATTN: Document Control

US Army White Sands Missile Range
    ATTN: STEWS-TN-N, K. Cummings

DEPARTMENT OF THE NAVY

Naval Ocean Systems Center
    ATTN: Code 532
    ATTN: Code 5322, M. Paulson
    ATTN: Code 5323, J. Ferguson

Naval Research Laboratory
    ATTN: Code 7500, B. Wald
    ATTN: Code 4780, S. Ossakow
    ATTN: Code 4187
    ATTN: Code 4700
    ATTN: Code 4780
    ATTN: Code 7950, J. Goodman
    ATTN: Code 6700
    ATTN: Code 4720, J. Davis

Office of Naval Research
    ATTN: Code 414, G. Joiner
    ATTN: Code 412, W. Condell

Strategic Systems Project Office
    ATTN: NSP-2722, F. Wimberly
    ATTN: NSP-2141
    ATTN: NSP-43

DEPARTMENT OF THE AIR FORCE

Air Force Geophysics Laboratory
    ATTN: OPR, H. Gardiner
    ATTN: OPR-1
    ATTN: LKB, K. Champion
    ATTN: CA, A. Stair
    ATTN: Phy, J. Buchau
    ATTN: R. Babcock
    ATTN: R. O'Neil

Air Force Technical Applications Ctr
    ATTN: TN

Air Force Weapons Laboratory
    ATTN: SUL
    ATTN: NTYC
    ATTN: NTN

Air Force Wright Aeronautical Lab
    ATTN: W. Hunt
    ATTN: A. Johnson

Air University Library
    ATTN: AUL-LSE

Rome Air Development Center
    ATTN: OCS, V. Coyne
    ATTN: TSLD

93

DEPARTMENT OF THE AIR FORCE (Continued)

Rome Air Development Center
    ATTN: EEP, J. Rasmussen

Space Command
    ATTN: DC, T. Long

Space Division
    ATTN: YGJB, W. Mercer

DEPARTMENT OF ENERGY

Department of Energy
GTN
    ATTN: DP-233

OTHER GOVERNMENT AGENCIES

Department of Commerce
National Oceanic & Atmospheric Admin
    ATTN: R. Grubb

Institute for Telecommunications Sciences
National Telecommunications & Info Admin
    ATTN: L. Berry
    ATTN: A. Jean
    ATTN: W. Utlaut

DEPARTMENT OF ENERGY CONTRACTORS

Los Alamos National Laboratory
    ATTN: T. Kunkle, ESS-5
    ATTN: MS 664, J. Zinn
    ATTN: MS 670, J. Hopkins
    ATTN: D. Simons
    ATTN: P. Keaton
    ATTN: J. Wolcott
    ATTN: R. Jeffries

Sandia National Lab
    ATTN: D. Thornbrough
    ATTN: D. Dahlgren
    ATTN: Tech Lib 3141
    ATTN: Space Project Div
    ATTN: Org 4231, T. Wright
    ATTN: Org 1250, W. Brown

DEPARTMENT OF DEFENSE CONTRACTORS

Aerospace Corp
    ATTN: J. Straus
    ATTN: I. Garfunkel
    ATTN: D. Olsen
    ATTN: R. Slaughter
    ATTN: T. Salmi
    ATTN: V. Josephson
    ATTN: K. S Cho

Berkeley Research Associates, Inc
    ATTN: S. Brecht
    ATTN: C. Prettie
    ATTN: J. Workman

Charles Stark Draper Lab, Inc
    ATTN: J. Gilmore
    ATTN: D. Cox
    ATTN: A. Tetewski

DEPARTMENT OF DEFENSE CONTRACTORS (Continued)

Cornell University
    ATTN: M. Kelly
    ATTN: D. Farley, Jr

EOS Technologies, Inc
    ATTN: B. Gabbard

Institute for Defense Analyses
    ATTN: E. Bauer
    ATTN: H. Wolfhard
    ATTN: J. Aein
    ATTN: H. Gates

JAYCOR
    ATTN: J. Sperling

Johns Hopkins University
    ATTN: J. Newland
    ATTN: T. Evans
    ATTN: P. Komiske
    ATTN: J. Phillips

Kaman Tempo
    ATTN: DASIAC
    ATTN: B. Gambill
    ATTN: J. Devore
    ATTN: W. McNamara
    ATTN: W. Knapp
    ATTN: K. Schwartz

M.I.T. Lincoln Lab
    ATTN: D. Towle

Mission Research Corp
    ATTN: F. Fajen
    ATTN: S. Gutsche
    ATTN: D. Knepp
    ATTN: R. Hendrick
    ATTN: R. Bogusch
    ATTN: F. Guigliano
    ATTN: R. Kilb
    ATTN: C. Lauer
    ATTN: Tech Library
    ATTN: G. McCartor
    ATTN: R. Bigoni

Pacific-Sierra Research Corp
    ATTN: F. Thomas
    ATTN: E. Field, Jr
    ATTN: H. Brode, Chairman SAGE

Physical Dynamics, Inc
4 cy ATTN: E. Fremouw
4 cy ATTN: J. Secan

R&D Associates
    ATTN: R. Lelevier
    ATTN: W. Wright
    ATTN: W. Karzas
    ATTN: R. Turco
    ATTN: M. Gantsweg
    ATTN: F. Gilmore
    ATTN: C. Greifinger
    ATTN: H. Ory
    ATTN: P. Haas

94

R&D Associates
      ATTN: G. Yoon

Rand Corp
      ATTN: C. Crain
      ATTN: E. Bedrozian

Stewart Radiance Laboratory
      ATTN: J. Ulwich

Technology International Corp
      ATTN: W. Boquist

Visidyne, Inc
      ATTN: W. Reidy
      ATTN: J. Carpenter
      ATTN: C. Humphrey
      ATTN: O. Shepard

SRI International
      ATTN: R. Tsunoda
      ATTN: J. Vickrey
      ATTN: V. Gonzales
      ATTN: W. Chesnut
      ATTN: D. McDaniels
      ATTN: K. Baron
      ATTN: R. Livingston
      ATTN: R. Leadabrand
      ATTN: G. Price
      ATTN: D. Neilson
      ATTN: A. Burns
      ATTN: J. Petrickes
      ATTN: G. Smith
      ATTN: W. Jaye
      ATTN: C. Rino

95